

ALMA MATER STUDIORUM · UNIVERSITÀ DI BOLOGNA

---

Scuola di Scienze  
Corso di Laurea Magistrale in Fisica

**LUMINOSITY DETERMINATION  
FOR THE MEASUREMENT OF THE PROTON-PROTON  
TOTAL CROSS-SECTION AT 8 TeV IN THE ATLAS  
EXPERIMENT.**

**Relatore:**  
Chiar.mo Prof.  
NICOLA SEMPRINI CESARI

**Presentata da:**  
GRAZIA CABRAS

**Correlatore:**  
Dott. BENEDETTO GIACOBBE

**Sessione III**  
**Anno Accademico 2013/2014**









## Abstract

La sezione d'urto totale adronica gioca un ruolo fondamentale nel programma di fisica di LHC. Un calcolo di questo parametro, fondamentale nell'ambito della teoria delle interazioni forti, non é possibile a causa dell'inapplicabilità dell'approccio perturbativo. Nonostante ciò, la sezione d'urto può essere stimata, o quanto meno le può essere dato un limite, grazie ad un certo numero di relazioni, come ad esempio il Teorema Ottico. In questo contesto, il detector ALFA (An Absolute Luminosity For ATLAS) sfrutta il Teorema Ottico per determinare la sezione d'urto totale misurando il rate di eventi elastici nella direzione forward. Un tale approccio richiede un metodo accurato di misura della luminosità in condizioni sperimentali difficoltose, caratterizzate da valori di luminosità istantanea inferiore fino a 7 ordini di grandezza rispetto alle normali condizioni di LHC. Lo scopo di questa tesi è la determinazione della luminosità integrata di due run ad alto  $\beta^*$ , utilizzando diversi algoritmi di tipo Event-Counting dei detector BCM e LUCID. Particolare attenzione è stata riservata alla sottrazione del fondo e allo studio delle incertezze sistematiche. I valori di luminosità integrata ottenuti sono  $L = 498.55 \pm 0.31$  (stat)  $\pm 16.23$  (sys)  $\mu\text{b}^{-1}$  and  $L = 21.93 \pm 0.07$  (stat)  $\pm 0.79$  (sys)  $\mu\text{b}^{-1}$ , rispettivamente per i due run. Tali saranno forniti alla comunità di fisica che si occupa della misura delle sezioni d'urto protone-protone, elastica e totale. Nel Run II di LHC, la sezione d'urto totale protone-protone sarà stimata con un'energia nel centro di massa di 13 TeV per capire meglio la sua dipendenza dall'energia in un simile regime. Gli strumenti utilizzati e l'esperienza acquisita in questa tesi saranno fondamentali per questo scopo.



## Abstract

The total hadronic cross section plays a fundamental role in the physics program of the Large Hadron Collider. A calculation of this fundamental parameter of strong interactions is not possible because a perturbative approach is not applicable. Even though, it can be estimated or bounded by a certain number of relations, such as the Optical Theorem. The ALFA (An Absolute Luminosity For ATLAS) detector exploits an experimental approach based on the Optical Theorem, to determine total cross section by measuring the elastic event rate in the forward direction. This approach requires an accurate method of measurement of the luminosity in very challenging experimental conditions characterized by an instantaneous luminosity up to 7 orders of magnitude below the standard LHC conditions. The aim of this thesis is the determination of integrated luminosity of two high- $\beta^*$  runs, using different Event-Counting algorithms of BCM and LUCID detectors. Particular attention has been paid to the background subtraction and to the study of the systematic uncertainties. Luminosity values of  $L = 498.55 \pm 0.31$  (stat)  $\pm 16.23$  (sys)  $\mu\text{b}^{-1}$  and  $L = 21.93 \pm 0.07$  (stat)  $\pm 0.79$  (sys)  $\mu\text{b}^{-1}$  were obtained for the two runs, respectively. The luminosity values determined in this thesis will be provided to the physics community performing the measurement of the  $pp$  elastic and total cross section. In LHC Run II, it is planned to perform a  $pp$  total cross section measurement at a center of mass energy of 13 TeV in order to increase the understanding of its energy dependence. The tools and the experience developed in this thesis will be fundamental for this purpose.



# Contents

<b>Introduction</b>	<b>1</b>
<b>1 Beam Dynamics and Luminosity Determination at the Hadron Colliders</b>	<b>3</b>
1.1 Beam Dynamics . . . . .	3
1.1.1 Magnetic and Electric Fields . . . . .	3
1.1.2 Betatron Motion and Transverse Emittance . . . . .	5
1.1.3 Beam Emittance . . . . .	8
1.2 Beam-Beam Interactions . . . . .	10
1.2.1 Head - on Collisions . . . . .	11
1.2.2 Crossing Angle . . . . .	13
1.2.3 Offset Collisions . . . . .	13
1.2.4 Hourglass Effect . . . . .	14
1.3 The Concept of Luminosity . . . . .	15
1.4 Status of LHC in 2012 . . . . .	16
1.5 The Luminosity Measurement . . . . .	19
1.5.1 Event - Counting Methods . . . . .	21
1.5.2 Hit - Counting Methods . . . . .	23
1.5.3 Pile-up Effects and Non-Linearity . . . . .	24
1.5.4 Particle-Flux Methods . . . . .	25
1.6 Luminosity Calibration Methods . . . . .	25
1.6.1 Single-Beam Parameters from Accelerator Instrumentation . . . . .	25
1.6.2 Calibration through Reference Physics Processes: Semilep- tonic $W$ and/or $Z$ decays . . . . .	26
1.7 Calibration through van der Meer Scans . . . . .	27
1.7.1 Absolute Luminosity from Beam Parameters . . . . .	28
1.7.2 Luminosity Calibration by Beam Separation Scans . . . . .	29

<b>2</b>	<b>Luminosity Determination at the ATLAS Experiment</b>	<b>31</b>
2.1	The ATLAS Experiment . . . . .	31
2.2	ATLAS Luminosity Sub-detectors . . . . .	32
2.2.1	The Inner Detector . . . . .	33
2.2.2	BCM . . . . .	34
2.2.3	LUCID . . . . .	36
2.2.4	ALFA . . . . .	36
2.2.5	The Calorimeters: FCAL and TileCal . . . . .	36
2.3	ATLAS Luminosity Algorithms . . . . .	37
2.3.1	Online Algorithms . . . . .	37
2.3.2	Offline Algorithms . . . . .	39
2.4	ATLAS Luminosity Calibration . . . . .	39
2.5	Systematic Uncertainties in the Luminosity Measurement in 2012 . . . . .	41
2.5.1	Systematic Uncertainties in the Absolute Luminosity Calibration . . . . .	41
2.5.2	Systematic Uncertainties on Luminosity Extrapolation . . . . .	44
<b>3</b>	<b>Measurement of the Total Cross Section from Elastic Scat- tering in <math>pp</math> Collisions at <math>\sqrt{s} = 7</math> TeV in 2011</b>	<b>49</b>
3.1	The Total Hadronic Cross Section . . . . .	49
3.2	Measurement of $\sigma_{tot}$ with Elastic Scattering through Optical Theorem . . . . .	52
3.3	Measurement of $\sigma_{tot}$ with Elastic Scattering in the Coulomb- Nuclear Interference Region . . . . .	54
3.4	Beam Optics for $\sigma_{tot}$ Measurement . . . . .	55
3.5	$t$ -reconstruction . . . . .	56
3.6	Measurement of $\sigma_{tot}$ at $\sqrt{s} = 7$ TeV in ATLAS in 2011 . . . . .	57
3.6.1	Data Taking . . . . .	57
3.6.2	The Roman Pots . . . . .	57
3.6.3	The ALFA Detector . . . . .	58
3.6.4	Principles of Measurement . . . . .	60
3.6.5	Data Acquisition and Analysis . . . . .	62
3.6.6	Luminosity Determination with ALFA . . . . .	63
3.6.7	ALFA Total Cross Section Results . . . . .	66
3.7	Measurement of $\sigma_{tot}$ at $\sqrt{s} = 7$ TeV with TOTEM . . . . .	66
3.7.1	TOTEM Results . . . . .	66
3.8	Comparison of ATLAS and TOTEM Measurements . . . . .	68

---

3.8.1	Systematic Uncertainties . . . . .	68
<b>4</b>	<b>Luminosity Determination for the Total Cross Section Measurement at <math>\sqrt{s} = 8</math> TeV</b>	<b>71</b>
4.1	The Data Sample . . . . .	71
4.1.1	Run 206881 at $\beta^* = 90$ m . . . . .	72
4.1.2	Run 213268 at $\beta^* = 1000$ m . . . . .	72
4.2	Analysis Procedure . . . . .	72
4.2.1	Luminosity Algorithms . . . . .	72
4.2.2	Statistical Errors . . . . .	73
4.2.3	Calibration . . . . .	74
4.3	Background Definition and Evaluation . . . . .	74
4.3.1	Afterglow Background . . . . .	75
4.3.2	Afterglow Modelling . . . . .	76
4.3.3	Afterglow Subtraction Results . . . . .	78
4.3.4	Beam Gas (Single-Beam) Background . . . . .	79
4.4	Luminosity Results . . . . .	81
4.4.1	Results for run 206881 at $\beta^* = 90$ m . . . . .	82
4.4.2	Results for run 213268 at $\beta^* = 1000$ m . . . . .	83
4.5	Systematic Uncertainties Evaluation . . . . .	89
4.6	General Comments . . . . .	94
	<b>Conclusions</b>	<b>95</b>
	<b>Appendices</b>	<b>96</b>
	<b>A Derivation of Hill's Equations</b>	<b>97</b>





# List of Figures

1.1	Scheme of a typical coordinate system for a circulating particle.	4
1.2	Layout of a FODO Cell. . . . .	7
1.3	Scheme of the motion of a single particle in the phase space ( $y, y'$ ): typically it defines an ellipse, characterized by the Courants-Snyder parameters $\alpha, \beta$ and $\gamma$ . . . . .	9
1.4	Scheme of collision between two beams with a crossing-angle $\theta_c$ . The beam-beam forces occur when particles of one beam encounter the fields produced by the opposite one. . . . .	10
1.5	Kick produced by a beam-beam force as a function of the amplitude (distance between the two beams) in red and linear force of a defocusing quadrupole is shown in green. . . . .	11
1.6	Scheme of head-on collision between bunch 1 and bunch 2. . .	12
1.7	Pictorial view of Hourglass Effect. The bunch shape at the IP is drawn in red and the blue line indicates the parabolic shape of the $\beta$ function. The bunch has a minimum in transverse size at the IP and grows moving away from it. . . . .	14
1.8	Evolution of the <i>beta</i> -function $\beta(s)$ and the beam size as a function of the distance from the IP. Two different values for the $\beta^*$ are plotted: 11 m in solid line and 0.55 m in dotted line.	15
1.9	The LHC injector complex. . . . .	18
1.10	Scheme of RF voltage (top) and, consequently, formation of RF buckets and bunches (bottom). The particle A is synchronous, while B is non-synchronous and performs oscillations in phase space. . . . .	18
1.11	Sketch of head-on collisions. . . . .	27
2.1	The ATLAS Experiment . . . . .	32
2.2	The ATLAS Luminosity detectors. . . . .	33
2.3	Inner Detector . . . . .	34

2.4	Schematic illustration of 4 BCM stations. Two identical modules are mounted in the two sides of ATLAS. The horizontal and vertical modules deliver separate luminosity measurements.	35
2.5	A schematic view of a Roman Pot. . . . .	37
2.6	Specific interaction rate as a function of the nominal beam separation for the BCMV_EventOR algorithm in the horizontal scanning direction ( $x$ ). The residual deviation of the data from a double Gaussian plus constant background fit, normalized to the statistical uncertainty at each scan point, is shown in the bottom panel. . . . .	40
2.7	Percentage deviations between the integrated luminosity measured by different detectors with respect to BCMHOR and as a function of time in 2012. . . . .	46
2.8	Percentage deviations of the measurement of $\mu$ from different detectors and algorithms with respect to BCM_HOR as a function of $\mu_{BCM\_HOR}$ . . . . .	47
3.1	Dependence of the total cross section from the centre-of-mass energy. . . . .	50
3.2	Pictorial view of the incident particle beam and the related target particle. Within a circle of radius $b_0$ in the plane of the target particle, the scattering probability cannot be larger than 1. Outside, it's not negligible essentially in a ring of width $1/k$ . The total cross section is bounded by $\pi(b_0 + 1/k)^2$ .	51
3.3	Differential elastic cross section estimation at LHC as a function of transferred momentum. The differential cross section is plotted for $\rho=0$ (dashed line) and $\rho=0.15$ (solid line) in order to highlight the interference region, as well as for $\alpha=0$ (dotted line) to isolate the nuclear contribution. . . . .	55
3.4	Picture of two Roman Pot vessels. . . . .	58
3.5	Schematic view of the ALFA tracking system where the two kinds of detector, main (MD) and overlap (OD) are visible. . .	59
3.6	Schematic sketch of the experimental set-up showing the ALFA Roman Pot station positions. . . . .	60
3.7	Comparison of <i>golden</i> (top) and <i>anti-golden</i> (bottom) topology for reconstruction of elastic scattered candidates. . . . .	63
3.8	Values of luminosity determined using various algorithms as a function of time during the run (top) and as percentual deviations with respect to the reference algorithm (bottom). . . .	65

3.9	Comparison of the three TOTEM results and ALFA (ATLAS detector performing this measurement) result in the determination of $\sigma_{tot}$ at $\sqrt{s}=7$ TeV (2011 data). . . . .	68
4.1	Typical shape of afterglow background induced by a single colliding bunch, an exponential tail with decay time of few $\mu s$ . . . . .	75
4.2	(A): Signal modelling for zero-counting, exclusive single-side ( $P_A, P_C$ ) and coincidence ( $P_{AND}$ ) algorithms. . . . .	76
4.3	(B): Background-only modelling based on the exclusive single-side background probabilities $P_{bA}$ and $P_{bC}$ . . . . .	77
4.4	(C): Table reporting the modelling of signal+background contributions to the different algorithms. . . . .	78
4.5	A typical BCID-distribution of the measured activity in LUCID, for a high-luminosity run, where the colliding bunches are visible together with the "previous-to-colliding" ones. . . . .	79
4.6	Measured (blue triangles) and afterglow-subtracted (green squares) $\mu$ for BCMHOR in the forbidden gap. . . . .	80
4.7	Measured (blue triangles) and afterglow-subtracted (green squares) $\mu$ for LCDOR in the forbidden gap for run 206881. . . . .	81
4.8	Ratio between afterglow background subtracted and measured $\mu$ for run 206881 for BCMHOR as a function of $\mu$ measured. . . . .	82
4.9	Ratio between afterglow background subtracted and measured $\mu$ for run 206881 for LCDOR as a function of $\mu$ measured. The ratio is about 2% with no dependency on $\mu$ . . . . .	83
4.10	(Left) BCMHOR measured (blue triangles), afterglow subtracted (green squares), afterglow and beam gas subtracted (red circles) $\mu$ for the unpaired bunch 3196 of run 206881. (Right) LCDOR measured (triangles), afterglow subtracted (squares), afterglow and beam gas subtracted (circles) $\mu$ for the unpaired bunch 3196 of run 206881. . . . .	84
4.11	Percentages of afterglow only (red triangles) and afterglow plus beam-gas (blue circles) for BCMHOR (left) and for LCDOR (right) for run 206881. . . . .	85
4.12	Percentages of afterglow only (red triangles) and afterglow plus beam-gas (blue circles) for BCMHOR (left) and for LCDOR (right) for the run 213268. . . . .	85
4.13	Average number of interactions per bunch crossing $\mu$ as a function of the LB number for the different luminosity algorithms for run 206881. . . . .	86
4.14	Percentage deviation of the various algorithms with respect to the reference one, BCMHOR. . . . .	86

4.15	Average number of interactions per bunch crossing $\mu$ as a function of the LB number for the various luminosity algorithms for run 213268. . . . .	87
4.16	Percentage deviation of the various algorithms with respect to the reference one, BCMHOR. . . . .	88
4.17	Long-term stability of the different luminosity algorithms along 2012. The dates of two ALFA runs (light green) and the corresponding $\nu dM$ sessions (orange) are marked with vertical lines. . . . .	90
4.18	$\mu$ as measured by LUCID (LCDOR algorithm) as a function of BCIDs. The activity 5 BCIDs before colliding and unpaired bunches is marked with coloured squares. . . . .	90
4.19	Run 206881: Beam-gas induced activity in LCDORA normalized to the bunch proton current for all colliding (blue), unpaired (red) and for the 3 ALFA-triggered colliding-bunches. .	91
4.20	Run 206881: Beam-gas induced activity in LCDORC normalized to the bunch proton current for all colliding (blue), unpaired (red) and for the 3 ALFA-triggered colliding-bunches. .	91
4.21	Run 213268: Beam-gas induced activity in LCDORA normalized to the bunch proton current for all colliding (pink), unpaired (red) and for the 3 ALFA-triggered colliding-bunches. .	93
4.22	Run 213268: Beam-gas induced activity in LCDORC normalized to the bunch proton current for all colliding (pink), unpaired (red) and for the 3 ALFA-triggered colliding-bunches. .	93

# List of Tables

1.1	Performance parameters achieved in 2012 data taking compared with the design values for physics runs. . . . .	17
1.2	Performance parameters achieved in ALFA runs, performed at $\beta^* = 90$ m and at $\beta^* = 1000$ m, these runs are analyzed in this thesis. . . . .	19
1.3	Hit-configurations in F and B sides for the various Event-counting algorithms. . . . .	22
2.1	Summary of the main characteristics of the 2012 $vdM$ scans performed at the ATLAS interaction point. . . . .	41
2.2	Relative systematic uncertainties on the determination of the visible cross section $\sigma_{vis}$ from the $vdM$ scans of April 2012 at $\sqrt{s} = 8$ TeV. . . . .	45
2.3	Main sources of systematic uncertainties on the calibrated luminosity. . . . .	47
3.1	Luminosity results for the different algorithms in the 2011 measurement. The uncertainties listed are statistical only. . .	64
3.2	List of the main sources of systematic uncertainties affecting the luminosity determination in the 2011 high $\beta^*$ runs. The total uncertainty is 2.45%. . . . .	65
4.1	Values of $\sigma_{vis}$ measured in July and November 2012 calibration for LUCID and BCM algorithms. . . . .	74
4.2	Integrated luminosity values (first column) and statistical errors (second column) determined with different algorithms for run 206881. In the third column, the deviations among the various algorithms to the reference BCMHOR are reported in units of the statistical errors. . . . .	84

---

4.3	Integrated luminosity values (first column) and statistical errors (second column) determined with different algorithms for run 213268. In the third column, the deviations among the various algorithms to the reference BCMHOR are reported in units of the statistical errors. . . . .	87
4.4	Systematic uncertainties on the luminosity measurement for runs 206881 and 213268. . . . .	92

# Introduction

The total hadronic cross section  $\sigma_{tot}$  is a fundamental parameter of the strong interaction theory. Unfortunately, direct calculation of this parameter from quantum chromodynamics is not possible because the perturbation theory is not applicable. Even though  $\sigma_{tot}$  can be estimated or bounded by a certain number of fundamental relations in high-energy scattering theory, such as the Optical Theorem (which relates the imaginary part of the forward elastic amplitude to the total cross section), a direct measurement at high energy is of the highest importance.

Traditionally, the Optical Theorem has been used at colliders in order to measure, via elastic scattering, the total hadronic cross section but there are other methods to perform this measurement.

The ALFA (*Absolute Luminosity For ATLAS*) detector, located at 240 meters from the IP1 of the Large Hadron Collider (the ATLAS Interaction Point), employs a method that requires an independent luminosity measurement. The total cross section measurement is performed during special runs using a dedicated high- $\beta^*$  optics and a parallel-to-point focusing. Such experimental conditions are required for the measurement of the elastic event rate. During these runs, the instantaneous luminosity is up to seven orders of magnitude lower with respect to the normal runs, ( $\mathcal{L} \sim 0.5 \times 10^{27} \text{ cm}^{-2}\text{s}^{-1}$ ). The detectors used for luminosity determination are BCM (*Beam Conditions Monitor*) and LUCID (*Luminosity measurements Using Cherenkov Integrating Detector*), exploiting different event-counting algorithms.

The purpose of this thesis is the determination of the integrated luminosity for two different low-luminosity runs, acquired in the 2012 data-taking at  $\sqrt{s}=8$  TeV.

Chapter 1 focuses on the beam dynamics and on the concept of luminosity, one of the main figures of merit for any particle collider. A description of the main methods for luminosity determination and calibration follows, with particular attention to the LHC conditions in 2012.

Chapter 2 provides a description of the ATLAS Luminosity sub-detectors, of the algorithms used for the luminosity measurement and of the calibration

procedure.

Chapter 3 describes the various experimental approaches to the measurement of the total  $pp$  cross section focusing on the measurements performed by the ALFA and TOTEM experiments in 2011 with a center of mass energy of  $\sqrt{s} = 7$  TeV.

Finally, Chapter 4 provides a detailed description of the analysis procedure used for the determination of the integrated luminosity needed for the total  $pp$  cross section measurement at ATLAS at  $\sqrt{s} = 8$  TeV with 2012 data. Particular attention was devoted to the background subtraction, one of the most delicate issues given the experimental conditions of the data-taking. A detailed treatment of the systematic uncertainties related to the luminosity measurement is also provided, as these directly enter in the overall systematics of the total cross section result.



# Chapter 1

## Beam Dynamics and Luminosity Determination at the Hadron Colliders

### 1.1 Beam Dynamics

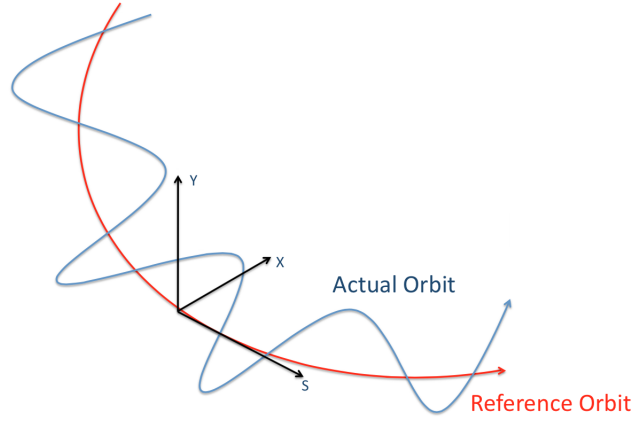
In order to provide a description of the techniques used in the determination of luminosity in a collider, a brief overview of the beam dynamics is necessary.

#### 1.1.1 Magnetic and Electric Fields

A charged particle, in the electromagnetic field of an accelerator, gains energy by the interaction with the electric field  $\vec{E}$  and its trajectory is curved when it passes through a dipole magnet. At relativistic velocities, an electric field  $\vec{E}$  and a magnetic field  $\vec{B}$  have the same effect: a magnetic field of 1 T would be, at this condition, equal to an electric one of  $3 \cdot 10^8 V \cdot m^{-1}$ . Producing such an electric field is far beyond our actual technical limits, magnetic fields are used to steer the beams.

The physical fundamentals of beam steering and focusing are called *beam optics*.

A typical coordinate system  $(x, y, s)$  used to describe the particle's motion is shown in Fig. 1.1. In order to describe the path of the particles,  $s$  is the *longitudinal* direction along the *reference orbit*, while  $x$  and  $y$  are the *transversal* coordinates which define the *transverse plane*. We call  $\vec{r}_0$  the reference trajectory with null  $x$  and  $y$  coordinates for all  $s$ . The particle



**Figure 1.1:** Scheme of a typical coordinate system for a circulating particle.

trajectory around the reference orbit can be expressed as:

$$\vec{r} = \vec{r}_0 + x\hat{x}(s) + y\hat{y}(s) \quad (1.1)$$

The  $\vec{B}$  field components can be expressed as a function of a *dipolar* and *quadrupolar* term. Dipole and quadrupoles are important in the comprehension of the *beam optics*.

Dipole magnets guide the charged particles along the closed orbit and the Lorentz force bends the trajectory with a bending angle  $\theta$

$$\theta = \frac{q}{p} \int_{s_1}^{s_2} B dl = \frac{1}{B\rho} \int_{s_1}^{s_2} B dl \quad (1.2)$$

where  $p$  and  $q$  are the momentum and the charge of the particle, respectively, while  $\rho$  is the bending radius.

Knowing that the total bending angle of a circular accelerator is  $2\pi$ , the total dipole field is

$$\oint B dl = \frac{2\pi p}{q} = 2\pi B\rho \quad (1.3)$$

from which we derive an expression for the bending radius  $\rho$

$$\rho = \frac{mv}{qB} = \frac{p}{qB} \quad (1.4)$$

While dipole magnets are used to bend the particle's trajectory, quadrupole magnets are used to focus or defocus the beam and to control the beam size. A focusing quadrupole in the horizontal plane corresponds to a defocusing

one on the vertical plane and viceversa. In an accelerator, quadrupoles with opposite polarities are used to provide focusing in the two transverse directions.

The task of the electric fields is to accelerate the charged particles. There are several technologies that can be used and the choice depends on the scale of energy. At high energies, radiofrequencies (RF) are used to generate a longitudinal electric field. The passage through a RF cavity induce a gain/loss of energy expressed as  $\Delta E = q\Delta V$ , where  $\Delta V = V_0 \sin(\omega_{RF}t + \phi)$  is the effective gap voltage,  $\omega_{RF}$  is the RF frequency,  $V_0$  is the effective peak accelerating voltage and  $\phi$  is the phase angle. The reason of using RF cavities is that particles accelerated to high energy require *synchronization*. It's necessary that the particle always sees the accelerating voltage, so the RF frequency must be an integer ( $h$ ) multiple of the revolution frequency. In that way, the particle crosses the electric field every turn at a constant phase and so experiences a constant force.

$$f_{RF} = h \cdot f_{rev} \quad (1.5)$$

A particle with a speed  $\beta$  (in units of  $c$ ) circulates in the accelerator with a period  $T_{rev} = \frac{2\pi R}{\beta c}$  and a frequency  $f_{rev} = \frac{\beta c}{2\pi R}$ .

### 1.1.2 Betatron Motion and Transverse Emittance

The *betatron motion* describes the motion of the particle in the transverse plane, around the reference orbit.

The equation describing this motion is derived from the Lorentz force. Knowing that  $\vec{B}$  is non-null only on the transverse plane  $xy$ , the *Hill's equations* (See Appendix A) can be written as:

$$x'' + K_x(s)x = 0 \quad (1.6)$$

$$y'' + K_y(s)y = 0$$

$$K_x = \frac{1}{\rho^2} \mp K_1(s) \quad (1.7)$$

$$K_y = \mp K_1(s)$$

where  $K_1(s) = \frac{B_1(s)}{B\rho}$  is the effective focusing function which sign depends on the charge of the particle and  $B_1(s)$  is the magnetic field evaluated at the center of the quadrupole.  $K_x(s)$  and  $K_y(s)$  are periodic and can be assumed constant because in the accelerator magnetic field components are nearly uniform.

Considering  $K$  as both the vertical and horizontal component (assuming the

periodic condition  $K(s + L) = K(s)$ , being  $L$  the distance between two successive quadrupole stations (see Fig.1.2), the solution to Hill's equation will be:

$$y(s) = \begin{cases} A \cos(\sqrt{K}s + b) & K > 0 \\ As + b & K = 0 \\ A \cosh(\sqrt{-K}s + b) & K < 0 \end{cases}$$

An alternative expression can be expanded in terms of the *betatron state vector*  $\mathbf{y}(s)$  and the *betatron transfer matrix*  $M(s|s_0)$  [1]:

$$\mathbf{y}(s) = \begin{pmatrix} y(s) \\ y'(s) \end{pmatrix} \quad (1.8)$$

$$\mathbf{y}(s) = M(s|s_0)\mathbf{y}(s_0) \quad (1.9)$$

Eq. (1.9) is the solution of Hill's equation in terms of betatron state vector and the betatron transfer matrix, where  $M(s|s_0)$  has the following expression, depending on  $K$  ( $\ell = s - s_0$ ):

- $K > 0$  (focusing quadrupole)

$$\begin{pmatrix} \cos\sqrt{K}\ell & \frac{1}{\sqrt{K}}\sin\sqrt{K}\ell \\ -\sqrt{K}\sin\sqrt{K}\ell & \cos\sqrt{K}\ell \end{pmatrix}$$

- $K = 0$  (drift space)

$$\begin{pmatrix} 1 & \ell \\ 0 & 1 \end{pmatrix}$$

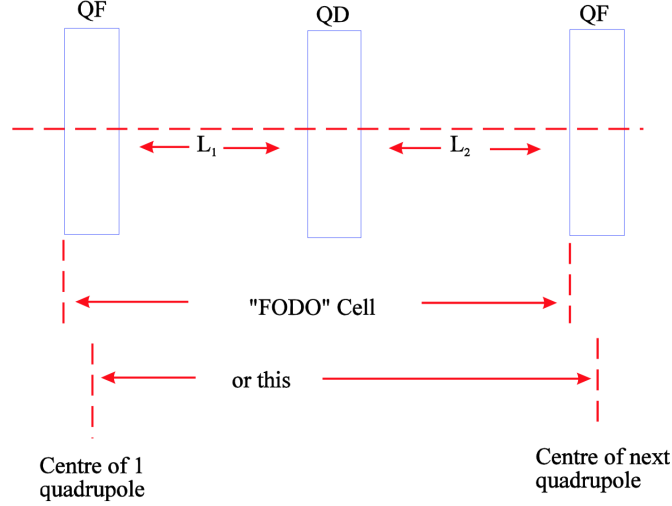
- $K < 0$  (defocusing quadrupole)

$$\begin{pmatrix} \cosh\sqrt{|K|}\ell & \frac{1}{\sqrt{|K|}}\sinh\sqrt{|K|}\ell \\ \sqrt{|K|}\sinh\sqrt{|K|}\ell & \cosh\sqrt{|K|}\ell \end{pmatrix}$$

The solution of Hill's equations for  $K > 0$  can be interpreted as an harmonic oscillator for which the solution is:

$$y(s) = Aw(s)\cos(\Phi(s) - \Phi_0) \quad (1.10)$$

where  $w(s)$  is a periodic function with periodicity  $L$ ,  $\Phi(s) = \sqrt{K}s$ ,  $A$  and  $\Phi_0$  are the integration constants and  $w(s)$  is a periodic function with periodicity  $L$ . Since  $K(s)$  is a periodic function,  $K(s + L) = K(s)$  where the period  $L$  can coincide with the accelerator circumference but usually corresponds to



**Figure 1.2:** Layout of a FODO Cell.

the distance between two *FODO* cells (typically, the structure of the focusing/defocusing system is the so-called FODO cell, F stands for focusing, O for drift space and D for defocussing, see Fig.1.2) for a schematic picture. The substitution of Eq.(1.10) in the Hill's equation allow us, at last, to define a new set of variables:

$$\beta(s) = \frac{w^2(s)}{k} \quad (1.11)$$

$$\alpha(s) = -\frac{1}{2} \frac{\partial \beta(s)}{\partial s} \quad (1.12)$$

$$\gamma(s) = \frac{1 + \alpha^2(s)}{\beta(s)} \quad (1.13)$$

Eqs. (1.11), (1.12) and (1.13) represent the *Courant - Snyder* functions or *Twiss* parameters and they can be used to parametrize the transfer matrix  $\mathbf{M}$  that describes a complete turn around the ring

$$\mathbf{M} = \begin{pmatrix} \cos\Phi + \alpha\sin\Phi & \beta\sin\Phi \\ -\gamma\sin\Phi & \cos\Phi - \alpha\sin\Phi \end{pmatrix} \quad (1.14)$$

where  $\Phi$  is the *betatron phase advance*, defined as:

$$\Phi = \int_{s_0}^{s_0+L} \frac{ds}{\beta(s)} \quad (1.15)$$

where  $L$  is the length of the periodic beam line for which the  $K$  function is periodic and  $\beta(s)$  is the *betatron amplitude function*. For an accelerator of circumference  $C = NL$  with  $N$  identical superperiods,  $N\Phi$  is the phase change per revolution. We can also derive characteristic quantities  $Q_x$  and  $Q_y$  for an accelerator called the *betatron tunes*, the number of betatron oscillation per turn.

$$Q_i = \frac{N\Phi_i}{2\pi} = \frac{1}{2\pi} \int_s^{s+C} \frac{ds}{\beta_y(s)} \quad (1.16)$$

where  $i = x, y$ . The betatron oscillation frequency is  $Q_i f_0$ , where  $f_0$  is the revolution frequency.

The general solution of Hill's equations in the vertical plane becomes:

$$y(s) = a\sqrt{\beta_y(s)}\cos[\Phi_y(s) + \Phi_0] \quad (1.17)$$

with

$$\Phi_y(s) = \int_0^s \frac{ds}{\beta_y(s)} \quad (1.18)$$

This means that we have a pseudo-harmonic oscillation with varying amplitude  $\beta_y^{1/2}(s)$ .

In an accelerator structure, the motion can be reconstructed knowing the evolution of the Courant- Snyder parameters and of the phase advance along the coordinate  $s$ .

### 1.1.3 Beam Emittance

The particle distribution is generally described by a six dimensional density function  $\rho$  in which  $x, y, s$  represent the variables that define the coordinate system. In linear dynamics the transverse and longitudinal distributions are often considered as uncorrelated, so the six dimension can therefore be factorized into three independent phase-space  $(x, x')$ ,  $(y, y')$  and  $(s, E)$ .

Replacing  $\Phi_y + \Phi_0$  by  $\theta(s)$  in Eq. (1.17),

$$y(s) = a\sqrt{\beta(s)}\cos\theta(s) \quad (1.19)$$

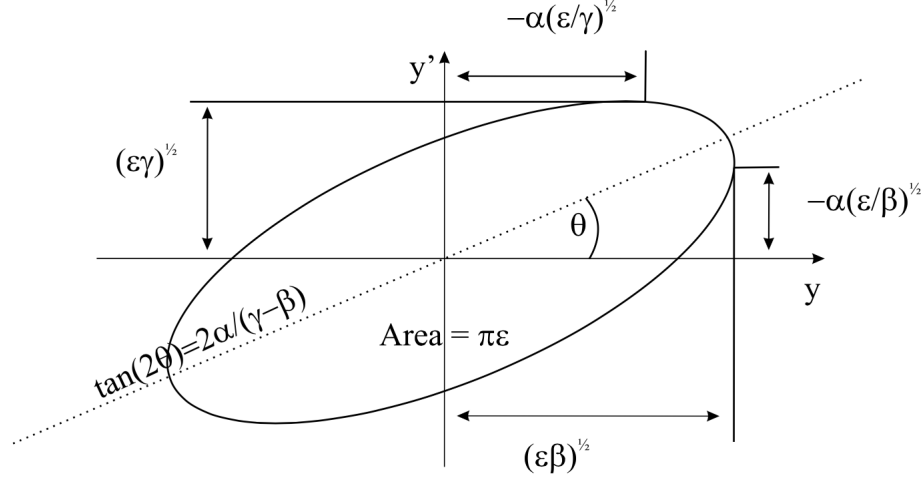
and

$$y'(s) = -\frac{a}{\beta(s)}[\sin\theta(s) + \alpha(s)\cos\theta(s)] \quad (1.20)$$

and combining them, the following equation can be written as:

$$\gamma y^2 + 2\alpha y y' + \beta y'^2 = a^2 \quad (1.21)$$

which is the *Courant - Snyder invariant* which remains constant along a



**Figure 1.3:** Scheme of the motion of a single particle in the phase space  $(y, y')$ : typically it defines an ellipse, characterized by the Courants-Snyder parameters  $\alpha$ ,  $\beta$  and  $\gamma$

particle trajectory and describes an ellipse (Fig 1.3), in the phase-space  $(y, y')$ . The parameters are determined by the *lattice functions*  $\alpha$ ,  $\beta$  and  $\gamma$  at the location  $s$ .  $a^2$  is called *emittance* of a single particle following its individual trajectory:

$$\epsilon = a^2 = \frac{\text{Ellipse area}}{\pi} \quad (1.22)$$

The emittance is the area of the ellipse which contains a certain percentage of particles. For example, a 95% emittance is defined as the area of the ellipse which contains 95% of the total particles. The ellipse can have different orientations depending on the location  $s$  around the ring but its area remains constant.

A beam is composed by particles centered around the reference orbit, so for any distribution of particles, it's possible to define a region in phase space occupied by all of them. Taking a normalized distribution function  $\rho(y, y')$ , the moments of the beam distribution are

$$\begin{aligned} \langle y \rangle &= \int \int y \rho(y, y') dy dy' \\ \langle y' \rangle &= \int \int y' \rho(y, y') dy dy' \end{aligned} \quad (1.23)$$

$$\begin{aligned} \sigma_y^2 &= \int \int (y - \langle y \rangle)^2 \rho(y, y') dy dy' \\ \sigma_{y'}^2 &= \int \int (y' - \langle y' \rangle)^2 \rho(y, y') dy dy' \\ \sigma_{yy'}^2 &= \int \int (y - \langle y \rangle)(y' - \langle y' \rangle) \rho(y, y') dy dy' = r \sigma_y \sigma_{y'} \end{aligned} \quad (1.24)$$

where  $\sigma_y$  and  $\sigma_{y'}$  are the RMS beam widths,  $\sigma_{yy'}$  is the correlation and  $r$  is the correlation coefficient.

The *RMS beam emittance* is defined as:

$$\epsilon_{rms} = \sqrt{\sigma_y^2 \sigma_{y'}^2 - \sigma_{yy'}^2} = \sigma_y \sigma_{y'} \sqrt{1 - r^2} \quad (1.25)$$

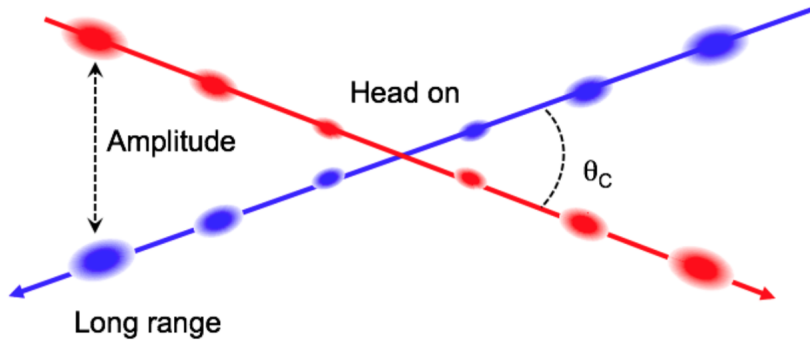
and it is equal to the phase space area enclosed by the Courant-Snyder ellipse of the RMS particle. It can be shown that for a beam with RMS emittance  $\pi\epsilon$ , the RMS beam width is

$$\sigma_y = \sqrt{\beta\epsilon} \quad (1.26)$$

## 1.2 Beam-Beam Interactions

A beam is a charged particle collection and it behaves as an electromagnetic potential for other particles. This force acts both on the other beam and within the beam itself. In the case of a collider where the two beams travel in different rings, as in the LHC case, the beam-beam forces act only close to the Interaction Points (IPs), where the two beams intersect each other [2].

The distribution of the particles within a beam can have different shapes.

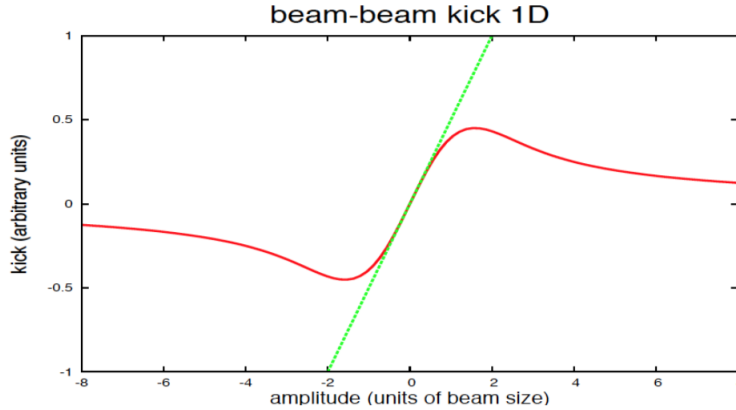


**Figure 1.4:** Scheme of collision between two beams with a crossing-angle  $\theta_c$ . The beam-beam forces occur when particles of one beam encounter the fields produced by the opposite one.

The easiest case is the one of the *Gaussian beam*.

At LHC, the beams collide in the IPs with an angle which allow them not to intersect each other out of this region, see (Fig.1.4). When the beams are close to the IP, they feel the effects of a *long-range force*, due to the electromagnetic force each beam exert on the other one. Fig.(1.5) shows the





**Figure 1.5:** Kick produced by a beam-beam force as a function of the amplitude (distance between the two beams) in red and linear force of a defocusing quadrupole is shown in green.

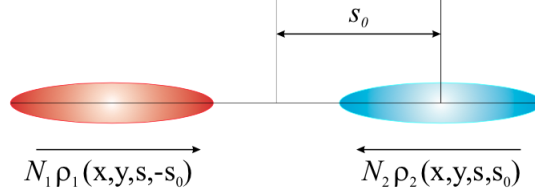
*kick* produced by the beam-beam force as a function of the distance between the two beams. For small distances (*head-on* collisions) the force is linear, while for larger distances it becomes non-linear. The linear part resembles that of a quadrupole field. A defocusing effect and, consequently, a change of the  $\beta$  functions of the beams are therefore expected and lead to orbit distortion. The beam-beam forces change thus the effective beam-optics. This change of the beam-optics can result in an increase of the emittance and in non-Gaussian tails of the particles distributions. The linear forces have higher impact on high-density beams (high intensity and small beam-sizes), exactly the ideal condition to achieve high luminosity. So, the beam-beam interactions are a limiting factor for the luminosity at a collider.

### 1.2.1 Head - on Collisions

The two beams have different distribution functions and their overlap integral is proportional to luminosity [3]:

$$\mathcal{L}_b = f_r N_1 N_2 N_b K \int \int \int \int \rho_1(x, y, s, -s_0) \rho_2(x, y, s, s_0) dx dy ds ds_0 \quad (1.27)$$

being  $\rho_1$  and  $\rho_2$  the particle distribution functions,  $N_1$  and  $N_2$  the bunch intensities (the number of particles per bunch),  $f_r$  is the revolution frequency and  $N_b$  the number of colliding bunches (see Fig 1.6).  $K$  is a kinematic factor defined as follows (assuming that  $s_0 = 0$  because the beams are moving



**Figure 1.6:** Scheme of head-on collision between bunch 1 and bunch 2.

against each other):

$$K = \sqrt{(\vec{v}_1 - \vec{v}_2)^2 - \frac{(\vec{v}_1 \times \vec{v}_2)^2}{c^2}} \quad (1.28)$$

In case of head-on collisions and relativistic particles,  $\vec{v}_1 = \vec{v}_2 = c$ ,  $K = 2$ . In the assumption of uncorrelated densities, Eq. 1.27 can be rewritten as:

$$\mathcal{L}_b = 2f_r N_1 N_2 N_b \int \int \int \int \rho_{1x}(x) \rho_{1y}(y) \rho_{1s}(s-s_0) \rho_{2x}(x) \rho_{2y}(y) \rho_{2s}(s+s_0) dx dy ds ds_0 \quad (1.29)$$

Assuming the beam profiles being Gaussian, the integrals can be calculated analytically. The distribution functions are expressed as:

$$\rho_{ix}(x) = \frac{1}{\sqrt{2\pi}\sigma_{ix}} e^{-\frac{x^2}{2\sigma_{ix}^2}} \quad (1.30)$$

$$\rho_{iy}(y) = \frac{1}{\sqrt{2\pi}\sigma_{iy}} e^{-\frac{y^2}{2\sigma_{iy}^2}} \quad (1.31)$$

$$\rho_{is}(s \pm s_0) = \frac{1}{\sqrt{2\pi}\sigma_{is}} e^{-\frac{(s \pm s_0)^2}{2\sigma_{is}^2}} \quad (1.32)$$

where  $i = 1, 2$  refers to the two beams and Eq. (1.29) becomes:

$$\mathcal{L} = \frac{2N_1 N_2 f N_b}{(\sqrt{2\pi})^2 \sigma_{1x}^2 \sigma_{2x}^2 \sigma_{1y}^2 \sigma_{2y}^2 \sigma_{1s}^2 \sigma_{2s}^2} \cdot \int \int \int \int_{-\infty}^{+\infty} e^{-x^2 \left( \frac{1}{2\sigma_{1x}^2} + \frac{1}{2\sigma_{2x}^2} \right) - y^2 \left( \frac{1}{\sigma_{1y}^2} + \frac{1}{\sigma_{2y}^2} \right) - \frac{(s-s_0)^2}{2\sigma_{1s}^2} - \frac{(s-s_0)^2}{2\sigma_{2s}^2}} dx dy ds ds_0 \quad (1.33)$$

Solving Eq. (1.33) like a Gaussian integral, the general expression of the luminosity for unequal Gaussian bunched beams colliding head-on is:

$$\mathcal{L} = \frac{N_1 N_2 f N_b}{2\pi} / \sqrt{\sigma_{1x}^2 + \sigma_{2x}^2} \sqrt{\sigma_{1y}^2 + \sigma_{2y}^2} = \mathcal{L}_{max} \quad (1.34)$$

Eq. (1.34) expresses the *maximum luminosity* which is available for head-on collisions in a collider with Gaussian bunched beams.

In practice, we have to include additional effects which reduce the maximum achievable luminosity, namely:

- crossing angle
- offset collisions
- hourglass effect

### 1.2.2 Crossing Angle

The crossing angle is introduced in order to restrict collisions only to the IP and to avoid unwanted *parasitic*-collisions at the other positions in the ring where the two beams are not separated, see Fig.(1.4). Due to the crossing angle  $\theta_c$ , the luminosity is reduced by a factor:

$$F_c = \sqrt{1 + \left(\frac{\theta_c \sigma_s}{2\sigma^*}\right)^2} \quad (1.35)$$

where  $\sigma_s$  is the longitudinal ( $s$ ) bunch length and  $\sigma^*$  the transverse R.M.S. beam size at the interaction point.

### 1.2.3 Offset Collisions

The two beams do not always collide head-on, actually they can be shifted in the horizontal and vertical directions by arbitrary displacements  $x_i$  and  $y_i$  ( $i = 1, 2$ ). In real conditions, the density distribution in the transverse plane is thus expressed as:

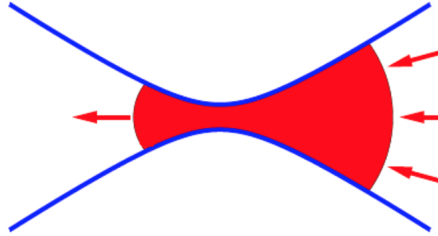
$$\rho_{ix} = \frac{1}{\sigma_{ix}\sqrt{2\pi}} e^{-\left(\frac{(x-x_i)^2}{2\sigma_{ix}^2}\right)} \quad (1.36)$$

$$\rho_{iy} = \frac{1}{\sigma_{iy}\sqrt{2\pi}} e^{-\left(\frac{(y-y_i)^2}{2\sigma_{iy}^2}\right)} \quad (1.37)$$

Despite the displacements, the velocities are still collinear and  $K$  is unchanged ( $K = 2$ ). The luminosity will be

$$\mathcal{L} = \mathcal{L}_{MAX} e^{-\left[\frac{\delta_x^2}{2(\sigma_{1x}^2 + \sigma_{2x}^2)} - \frac{\delta_y^2}{2(\sigma_{1y}^2 + \sigma_{2y}^2)}\right]} \quad (1.38)$$

where  $\mathcal{L}_{MAX}$  is the luminosity in head-on collision case and  $\delta_x$  and  $\delta_y$  represent the two displacements of the centroids in the transverse plane. The dependence on the transverse offset is a Gaussian function.



**Figure 1.7:** Pictorial view of Hourglass Effect. The bunch shape at the IP is drawn in red and the blue line indicates the parabolic shape of the  $\beta$  function. The bunch has a minimum in transverse size at the IP and grows moving away from it.

#### 1.2.4 Hourglass Effect

The beam size  $\sigma(s)$  is related to the betatron function and emittance:

$$\sigma(s) = \sqrt{\epsilon\beta(s)} \quad (1.39)$$

At the interaction point,  $\beta(s)$  is typically adjusted to have a local minimum in order to minimize the beam size and consequently maximize the interaction rate. The value of  $\beta(s)$  at the IP is known as  $\beta^*$ .

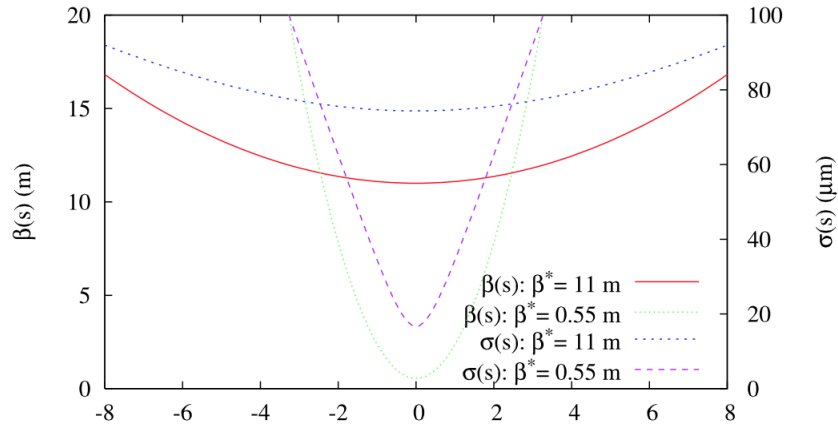
The assumption of the previous discussion is that the beam density functions are uncorrelated in the transverse and longitudinal planes and that the beam sizes are constant in the collision region. Actually, for low  $\beta^*$ , this is not a good approximation. The  $\beta$ -function varies around the minimum value as:

$$\beta(s) = \beta^* \left( 1 + \frac{s^2}{\beta^{*2}} \right) \quad (1.40)$$

and the transverse beam size  $\sigma(s)$  depends on  $s$ :

$$\sigma(s) = \sigma^* \sqrt{1 + \frac{s^2}{\beta^{*2}}} \quad (1.41)$$

The effect is known as *hourglass effect* because of the shape of the function (Fig. 1.7). The  $\beta$  functions and beam sizes have a minimum at the IP and grow away from it, Fig.(1.8). The maximum luminosity is obtained for collisions occurring exactly at the IP, while away from the IP the beam size increases and the luminosity decreases. This effect becomes relevant if  $\beta^*$  is small compared to the bunch length, in particular if the ratio  $r = \beta^*/\sigma_s$  is



**Figure 1.8:** Evolution of the *beta*-function  $\beta(s)$  and the beam size as a function of the distance from the IP. Two different values for the  $\beta^*$  are plotted: 11 m in solid line and 0.55 m in dotted line.

of the order of one or less.

Typical values of  $\beta^*$  and  $\sigma_s$  for the LHC case are reported in Tabs. (1.1) and (1.2) both for the normal running conditions and for the runs analysed in this thesis. In this latter case where  $\beta^* = 90$  m or  $\beta^* = 1$  km, the hourglass effect is negligible.

### 1.3 The Concept of Luminosity

The term "Luminosity" was introduced in particle physics between 50s and 60s at **AdA**, an  $e^-e^+$  collider at the Frascati Laboratory: it was called the *source factor* and it connected the  $e^+e^-$  cross section  $\sigma_{e^-e^+}$  to the rate of annihilation events. The *source factor* was determined from the intensities, geometry and time structure of the circulating beams. Probably the appellation of "luminosity" in the context of Particle Physics was introduced by the founding father of AdA, B. Touschek, in analogy with the astronomical definition [4].

Together with the energy available in the centre of mass, the luminosity is the second main figure of merit of a collider because it quantifies its potentiality in providing a statistically significant sample of a class of events.

The luminosity has different definitions:

- the *instantaneous luminosity*  $\mathcal{L}$  ( $[cm^{-2}s^{-1}]$ ) reflects the instantaneous performance of the collider. The time interval where it is measured may fluctuate from tens of nanoseconds to minutes, depending on the type

of collider (bunched or continuous beams).  $\mathcal{L}$  decays exponentially with a time constant of hours or days. It is defined as follows:

$$\mathcal{L} = \frac{R}{\sigma} \quad (1.42)$$

where  $R$  is the rate and  $\sigma$  is the cross section of a general physical process.

- the *integrated luminosity*  $L = \int \mathcal{L} dt$  ( $[cm^{-2}]$ ) is the instantaneous luminosity integrated over a certain time interval. It is defined as:

$$L = \frac{\int R dt}{\sigma} = \frac{N}{\sigma} \quad (1.43)$$

where  $N$  is the number of produced events of a certain type and  $\sigma$  is the cross section of this class of events. The definition is independent of the class of events considered provided that the corresponding  $\sigma$  is used.

There are two ways of measuring the luminosity depending on the goal to achieve. In order to obtain the cross section of any physics channel, the *absolute luminosity* is necessary as visible by inverting Eq. (1.43). Such a measurement, of course, needs a calibration of the detectors used to measure the *relative* luminosity.

In order to monitor the relative luminosity variations, a *relative luminosity* monitoring is sufficient and it is useful, for example, to control the beam quality of the collider. Each detector able to provide a quantity which is proportional to the luminosity can be used to evaluate the relative luminosity.

## 1.4 Status of LHC in 2012

LHC is a proton-proton and heavy ion collider operating at the CERN laboratories in Geneva. LHC is the last stage of a set of accelerators, the injector chain, composed by the LINAC2, PS Booster, PS, SPS [5], which permits the final acceleration of LHC protons through these stages: Fig.(1.9) shows the LHC injector complex (in the regime of 7 TeV and including the heavy ion route). The acceleration of the LHC protons is performed in different successive stages:

- LINAC2. It is a linear accelerator for protons and ions. It injects beams of 50 MeV in the following accelerator with a rate of 1 Hz. The duration of each pulse ranges from 20  $\mu s$  to 150  $\mu s$  depending on the number of required protons.

Parameters	Value in 2012	Design value
Beam energy [TeV]	4	7
$\beta^*$ in IP1[m]	0.6	0.55
Bunch spacing[ns]	50	25
Max Number of bunches	1380	2808
$\sigma_{x,y}$ [ $\mu\text{m}$ ]	$\sim 12-18$	16.6
$\sigma_s$ [mm]	$\sim 42-52$	75
Average bunch intensity[protons/bunch]	$1.6 - 1.7 \times 10^{11}$	$1.5 \times 10^{11}$
Normalized emittance at the start of the fill [mm mrad]	2.5	3.75
Peak luminosity[ $\text{cm}^{-2} \text{s}^{-1}$ ]	$7.7 \times 10^{33}$	$1 \times 10^{34}$
Max mean number of events per BCID	$\approx 40$	19
Stored beam energy[MJ]	$\approx 140$	362

**Table 1.1:** Performance parameters achieved in 2012 data taking compared with the design values for physics runs.

- *Proton Synchrotron Booster* (PSB). It accelerates the beams coming from LINAC2 to an energy of 1.4 GeV. The accelerator is composed of 4 superimposed rings. Five bunches circulate in each ring that are then focused and sent through a magnet deflector into a single line for injection into the next accelerating element.
- *Proton Synchrotron* (PS). It accelerates protons up to an energy of 28 GeV. It has been set to separate the bunches by 25 ns.
- *Super Proton Synchrotron* (SPS). It is used as final injector for protons and heavy ions bringing the energy from 28 GeV to 450 GeV.

After injection in the LHC ring at 450 GeV, protons are accelerated up to the final energy (for each circulating beam). In 2012 the final energy was 8 TeV per beam.

As said in Sec.(1.1.1), particles are accelerated using a RF system deployed in specially designed cavities. At LHC, knowing that the RF frequency is 400.79 MHz, the  $f_{rev}$  is 11.245 kHz, the proton's speed is  $\sim c$  and  $2\pi R \sim 26659$  m (LHC circumference), from Eq.(1.5)  $h = 35640$  [6].

A particle exactly synchronized with the RF frequency is called *synchronous particle* and the other ones will oscillate longitudinally around her orbit, thanks to the RF system, see Fig.(1.10). This means that the particles are not spread uniformly around the accelerator circumference but they get "clumped" around the synchronous particle in the so-called *bunch*. There's a chain of 35640 RF-*buckets* around the machine which, thus, could be filled with bunches. In the nominal filling scheme, the bunches are spaced by 25 ns (i.e. 40 MHz). Therefore, 3564 potential slots are available, each of them having a unique *bunch crossing identifier* (BCID). The number of occupied

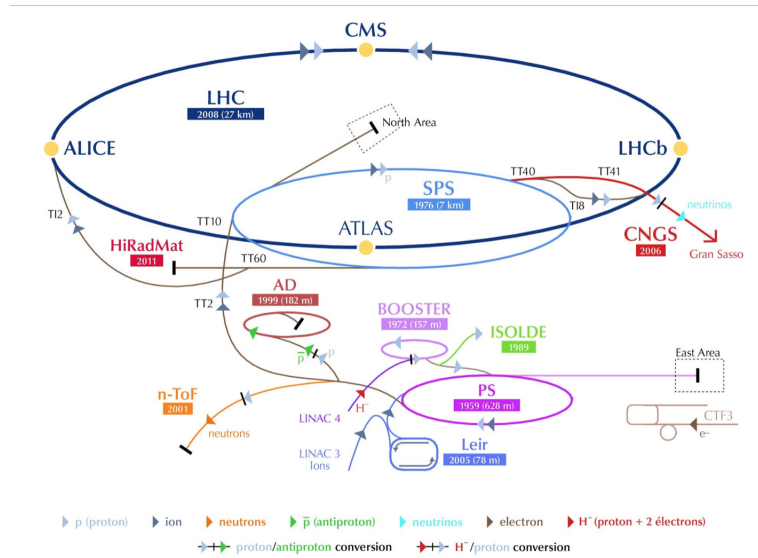


Figure 1.9: The LHC injector complex.

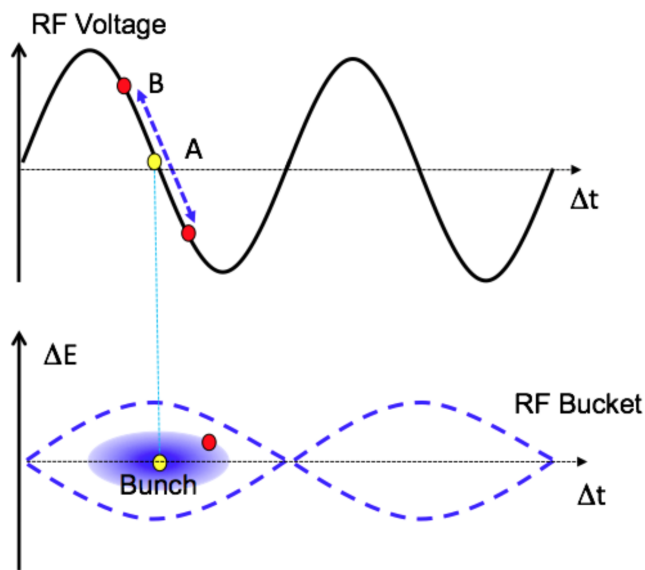


Figure 1.10: Scheme of RF voltage (top) and, consequently, formation of RF buckets and bunches (bottom). The particle A is synchronous, while B is non-synchronous and performs oscillations in phase space.

buckets is, by design, 2808, although a maximum of 1380 was filled in 2012 for technical reasons. Not all the bunches are *paired* or colliding and we can define different groups of BCIDs can be defined:



- *paired*: a filled bunch in both beams in the same BCID. This will collide at the IP.
- *unpaired isolated*: a filled bunch in one beam only, with no bunch in the other beam within 3 BCIDs.
- *unpaired non-isolated*: a bunch in one beam only, with a bunch in the other beam within 3 BCIDs.
- *empty*: a BCID without proton bunch in either beam.

Tabs. (1.1) and (1.2) report the relevant parameters of LHC as achieved in 2012 data taking for physics runs (2012) and for the high- $\beta^*$  runs analysed in this thesis.

	$\beta^*=90$ m	$\beta^* = 1000$ m
Beam energy [TeV]	4	4
$\beta^*$ in IP1[m]	90	1000
Bunch spacing[ns]	irrelevant	irrelevant
Number of bunches	108	3
Average bunch intensity[protons/bunch]	$6 - 7 \times 10^{10}$	$1 \times 10^{11}$
Normalized emittance at the start of the fill [mm mrad]	2-3	2-3
Peak luminosity[ $\text{cm}^{-2} \text{s}^{-1}$ ]	$5 \times 10^{27}$	$3 \times 10^{27}$
Mean number of interaction/BCID	$0.05 \div 0.1$	$0.001 \div 0.005$

**Table 1.2:** Performance parameters achieved in ALFA runs, performed at  $\beta^* = 90$  m and at  $\beta^* = 1000$  m, these runs are analyzed in this thesis.

## 1.5 The Luminosity Measurement

The bunch luminosity may be written as:

$$\mathcal{L}_b = \frac{\mu f_r}{\sigma_{inel}} \quad (1.44)$$

where  $\sigma_{inel}$  is the  $pp$  inelastic cross section.

In Eq.1.44, a new fundamental parameter has been introduced:  $\mu$ , the average number of inelastic  $p - p$  interactions per bunch crossing (BC) or *pile-up* parameter. This quantity is varying with time following the beam degradation formula  $\mathcal{L} = \mathcal{L}_0 e^{-\frac{t}{\tau}}$  with time-constant of 14 h at LHC. Due to this degradation, the luminosity is evaluated in short time period, called *Luminosity Blocks* (LB), in which the luminosity can be considered constant. In this perspective  $\mu$  and  $\mathcal{L}$  have to be considered as the average number of

interactions per bunch crossing and the average luminosity within each LB. There are several methods for the luminosity determination [4], the main being:

- *Event-Counting* algorithms: they are based on the determination of the fraction of bunch crossings in which a specified detector registers an "event" satisfying a given selection requirement. For example, a bunch crossing contains an "event" if at least one  $pp$  interaction induced at least one observed hit in the luminosity detector.
- *Hit-Counting* algorithms: they are based on the counting of the number of hits per bunch-crossing in luminosity detector. A hit can be, for example, an electronic channel providing a signal above a specified threshold.
- *Particle Counting* algorithms: they are based on the measurement of the particle distribution per bunch crossing inferred from reconstructed quantities as number of tracks or vertices in the tracking detector, energy distribution in the calorimeters, total ionization current, ...)

Eq. (1.44) can be rewritten, along with our approach, as:

$$\mathcal{L}_b = \frac{\mu f_r}{\sigma_{inel}} = \frac{\mu_{vis} f_r}{\epsilon \sigma_{inel}} = \frac{\mu_{vis} f_r}{\sigma_{vis}} \quad (1.45)$$

where

- $\epsilon$  is the efficiency for detecting one inelastic  $pp$  interaction with the defined selection criteria;
- $\mu_{vis} \equiv \epsilon \mu$  represents the average number of visible inelastic interactions per bunch crossing;
- $\sigma_{vis} \equiv \epsilon \sigma_{inel}$  is the fraction of the inelastic cross section visible by a detector with the defined selection criteria and it represents the calibration constant that relates the measured quantity  $\mu_{vis}$  to the absolute luminosity.

The calibration parameters  $\epsilon$  (and therefore  $\sigma_{vis}$ ) depends on the colliding particles, the available center of mass energy, the pseudorapidity and transverse momentum distribution and the defined selection criteria for any luminometer and reconstruction algorithm.

In the next section, the formulas needed to measure  $\mu_{vis}$  from the observables accessible to the different luminosity algorithms are discussed.

### 1.5.1 Event - Counting Methods

The value of  $\mu_{vis}$  is necessary to determine the luminosity  $\mathcal{L}_b$  of a bunch crossing within each LB. Two assumptions are made in the following:

- the number of  $pp$  interactions follows the Poisson statistics;
- the efficiency  $\epsilon_1$  to detect a single inelastic  $pp$  interaction doesn't change if, in the same bunch crossing, several interactions occur.

The efficiency  $\epsilon_n$  for detecting  $n$  interactions occurring in the same bunch crossing is thus:

$$\epsilon_n = 1 - (1 - \epsilon_1)^n \quad (1.46)$$

In the following the formulas used to determine the luminosity with various algorithms are reported, based on the described assumptions.

#### Inclusive-OR Algorithms

In an **Event-OR** algorithm, a bunch crossing is considered as containing an event if at least one hit is observed in the luminosity detector. Under the assumption that the probability of  $n$   $pp$  interactions in a bunch-crossing is described by a Poisson distribution with average value  $\mu$ :

$$P_n(\mu) = \mu^n \frac{e^{-\mu}}{n!} \quad (1.47)$$

and calling  $\epsilon_{OR}$  the single interaction detection efficiency of the detector, the probability of counting zero interactions is

$$P_0(\mu, \epsilon_{OR}) = e^{-\mu\epsilon_{OR}} = e^{-\mu_{vis}} = P_0(\mu_{vis}) \quad (1.48)$$

The probability of observing at least one event is therefore:

$$P_{Event-OR}(\mu_{vis}) = \frac{N_{OR}}{N_{BC}} = 1 - P_0(\mu_{vis}) = 1 - e^{-\mu_{vis}} \quad (1.49)$$

where  $N_{OR}$  is the number of bunch crossings, in a given LB, in which at least one  $pp$  collision satisfies the event-selection criteria of the OR algorithm, while  $N_{BC}$  is the total number of bunch crossings occurred in the same interval. Solving for  $\mu_{vis}$  Eq.(1.49), we get:

$$\mu_{vis} = -\ln \left( 1 - \frac{N_{OR}}{N_{BC}} \right) \quad (1.50)$$

$$\mu = \frac{\mu_{vis}}{\epsilon} = -\frac{1}{\epsilon} \ln \left( 1 - \frac{N_{OR}}{N_{BC}} \right) \quad (1.51)$$

### Coincidence Algorithms

In most of the experiments operating in a collider, the luminosity detectors consist in two independent parts located symmetrically on the two sides (Backwards and Forwards, B and F) of the IP. Coincidence (AND) algorithms requests both sides to record an event in the same bunch crossing (i.e. within 25 ns at LHC). In case of **Event-AND** selection, the relation between  $\mu_{vis}$  and  $N$  is more complicated then in Event-OR case. This coincidence condition can be satisfied both by a single  $pp$  interaction or from single hits from different  $pp$  collisions in the same bunch crossing. The efficiency is no longer one single parameter, three different efficiencies have to be taken into account:  $\epsilon_F$ ,  $\epsilon_B$  and  $\epsilon_{AND}$  that correspond of having, respectively, at least one hit in the F-side, at least one hit in the B-side and at least one hit on both sides. The three efficiencies are related to  $\epsilon_{OR}$  by

$$\epsilon_{OR} = \epsilon_F + \epsilon_B - \epsilon_{AND} \quad (1.52)$$

see Tab. (1.3).

Algorithm	Forwards	Backwards
OR	1	0
	0	1
	1	1
OR-F	1	0
	1	1
OR-B	0	1
	1	1
AND	1	1

**Table 1.3:** Hit-configurations in F and B sides for the various Event-counting algorithms.

Defining  $P_{Event-AND}$  the probability of the *Event-AND* algorithm:

$$P_{Event-AND}(\mu) = \frac{N_{AND}}{N_{BC}} = 1 - P_0(\mu) \quad (1.53)$$

$$= 1 - (e^{-\mu\epsilon^F} - e^{-\mu\epsilon^B} - e^{-\mu\epsilon^{OR}}) \quad (1.54)$$

$$= 1 - (e^{-\mu\epsilon^F} + e^{-\mu\epsilon^B} - e^{-\mu(\epsilon^F + \epsilon^B - \epsilon^{AND})}) \quad (1.55)$$

This expression can't be inverted analitically to obtain  $\mu$  from  $\frac{N_{AND}}{N_{BC}}$ . The best approach depends on the values of  $\epsilon^F$ ,  $\epsilon^B$  and  $\epsilon^{AND}$ . The equation can be simplified under the assumption that  $\epsilon^F \approx \epsilon^B$ , if the layouts, geometries

and efficiencies of the two sides of the luminometers are sufficiently similar. In this case, Eq.1.55 can be rewritten in the following way:

$$\frac{N_{AND}}{N_{BC}} = 1 - 2e^{-\mu(\epsilon^{AND} + \epsilon^{OR})/2} + e^{-\mu\epsilon^{OR}} \quad (1.56)$$

If the efficiencies are high enough,  $\epsilon_{AND} \simeq \epsilon_F \simeq \epsilon_B$ , the Eq.(1.55) can be approximated by:

$$\mu_{vis} = -\ln \left( 1 - \frac{N_{AND}}{N_{BC}} \right) \quad (1.57)$$

In the limit of  $\mu \ll 1$ , the equation can be approximated, with a Taylor expansion, as

$$P_{Event-AND} \sim 1 - (1 + \epsilon_A\mu + 1 - \epsilon_C\mu - 1 - \epsilon_A\mu - 1 - \epsilon_C\mu + \epsilon_{AND}\mu) \quad (1.58)$$

And consequently

$$\mu_{vis} \propto P_{Event-AND} \quad (1.59)$$

The analysis carried out in this thesis is performed on a sample which fulfil this condition and this simplification is therefore applied.

### 1.5.2 Hit - Counting Methods

Event-counting algorithms loose sensitivity when  $\mu_{vis} \gg 1$  because fewer bunch-crossings report zero observed interactions in a given time interval, implying that  $\frac{N_{OR}}{N_{BC}} \rightarrow 1$ , which makes Eq.(1.49) not usable anymore. This effect is known as *saturation* or *zero starvation*. The event-counting method is no longer exploitable and new techniques, such as the *hit-counting* method, where the number of hits in a given detector is counted rather than just the total number of events, have to be implemented.

Under the assumption that the number of hits due to  $pp$  interaction has a *binomial distribution* and the number of interactions per BC follows a Poisson distribution, the average probability of having a hit per bunch crossing in one of the detector channels can be computed as:

$$P_{HIT}(\mu_{vis}^{HIT}) = \frac{N_{HIT}}{N_{BC}N_{CH}} = 1 - e^{-\mu_{vis}^{HIT}} \quad (1.60)$$

In Eq.(1.60),  $N_{HIT}$  and  $N_{BC}$  are, respectively, the total numbers of hits and bunch crossings during a certain time interval, while  $N_{CH}$  is the number of detector channels, each having the possibility to independently record a hit. It's important to underline that the binomial assumption is true only if the probability to observe one hit in a channel is independent of the number of

hits observed in the other channels. Using this method, the mean number of interactions is:

$$\mu_{vis}^{HIT} = -\ln \left( 1 - \frac{N_{HIT}}{N_{BC}N_{CH}} \right) \quad (1.61)$$

and the bunch luminosity is:

$$\mathcal{L}_b = \frac{\mu_{vis}^{HIT} f_r}{\sigma_{vis}^{HIT}} \quad (1.62)$$

Despite being preferable to event-counting in the high- $\mu$  regime, the hit-counting algorithms are more sensitive with respect to the event-counting ones to instrumental effects such as threshold variations, instrumental noise, channel-to-channel efficiency variations, etc. Such algorithms are very useful at LHC, where very high values of the pile-up parameter makes it hard to use the event-counting algorithms. In the present analysis, as said before,  $\mu \ll 1$ , the hit-counting algorithms are no longer used.

### 1.5.3 Pile-up Effects and Non-Linearity

The applicability of the Poisson formalism depends on the validity of the assumption expressed by Eq. 1.46: the efficiency for detecting an elastic  $pp$  interaction is independent of the number of interactions that occur in each bunch crossing or equivalently, from the detector's point of view, the interactions are independent of each other. This latter assumption is intrinsically not true when a threshold is set to define a hit (and consequently one event), which is exactly the way event and hit counting work. If, for example, two  $pp$  interactions happen in the same bunch crossing, both producing signals in the detector which are individually below the threshold (i.e. they would not be individually detected), but whose sum is above the threshold, then the assumption of Eq.(1.46) is clearly violated. The same holds if background not related to the  $pp$  interaction add up to produce a hit in addition or even without signals from collisions. The result is that the Poisson assumption is violated and non-linearities appear in the luminosity measurement with increasing pile-up ( $\mu$ ). This effect is called *migration* and can be reduced, but not eliminated, by lowering as much as possible the thresholds. Only in the impossible limit of zero-threshold, the effect disappears. Migration becomes important in case of high pile-up parameter and it affects more hit-counting methods than event counting ones.

### 1.5.4 Particle-Flux Methods

The *particle-counting algorithms* are based on the use of observable directly proportional to the rate of particles interacting in the detector. These methods are intrinsically free from migration effects described in the previous section as no threshold is used in order to define an event or hit. A possible approach exploiting this principle and used by both ATLAS and CMS at LHC is to measure the current drawn by the readout PMTs in the calorimeters (both electromagnetic and hadronic) which is proportional to the particle flux inside the calorimeter, which is, in turn, proportional to the luminosity. Other quantities as the energy deposited in the calorimeter or the number of track counted by tracking devices are also frequently used.

## 1.6 Luminosity Calibration Methods

Each luminometer and algorithm must be calibrated by determining its visible cross section  $\sigma_{vis}$ , in order to determine the absolute luminosity (see Eq.1.45). There are several approaches to obtain the calibration constant [8].

The first method is to compare the visible interaction rate to the absolute luminosity computed, in the same time interval, from measured beam-parameters using Eq.(1.34). For example, far from the IP, the parameters of the two beams can be separately estimated and then extrapolated to the collision point. Unfortunately this technique has a limited precision (see Sec.1.6.1). A more accurate technique is the determination of the *beam-overlap area* directly at the IP using the beam-separation scans. This technique is described in Sec.(1.7).

A different approach is to measure, in dedicated runs, the elastic  $pp$  cross section at small angle and, using the optical theorem, to extract both the total cross section and the luminosity and relate it with the rate measured by the luminosity detectors, see Sec.(2.2.4).

Finally well known physics processes for which not only the cross section, but also the total acceptance and efficiency are known with sufficient precision can be used, see Sec.(1.6.2).

### 1.6.1 Single-Beam Parameters from Accelerator Instrumentation

The *bunch luminosity* can be inferred from the bunch population  $n_B$  and the transverse beam size  $\sigma_{iB}$  ( $i = x, y; B = 1, 2$ ) at the IP, see Eq.(1.34). The

single-beam profiles are difficult to measure accurately at the IP because of instrumental resolution and space limitation, while beam-current monitoring is more accurate.

The beam-profile monitoring is based on *wire scanners* or *synchrotron light telescope* methods. The monitors are installed in diagnostic regions away from the IP and they usually reports the projected horizontal and vertical RMS beam sizes, which can be extrapolated to the interaction point using an optical model of the collider lattice. Nevertheless, this technique has some limitation to be taken into account.

- Instrumental systematics (such as wire scanning speed, beam-induced heating, distortion of optical mirrors, resolution effects, etc.) make the precise *determination* of the *absolute* transverse beam size at the monitor rather challenging.
- The determination of the single-beam sizes to the IP requires the knowledge of a certain set of parameters, such as the betatron functions and betatron phases, both at the monitor points and at the IP. These parameters must be determined in separated sessions and their combination typically contribute with significant amount to the uncertainty to each of the four IP single-beam sizes  $\sigma_{iB}$ .
- Extrapolation becomes challenging when transverse coupling, dispersion and dynamic- $\beta$  effects play a significant role.
- The assumption of Gaussian beams, factorizable in  $x$  and  $y$ , may demonstrate itself as an incorrect hypothesis, because of instrumental limitations.

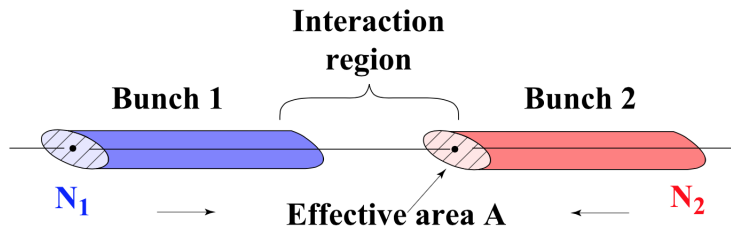
Typical precisions obtained with such methods are not better than 10-15%.

### 1.6.2 Calibration through Reference Physics Processes: Semileptonic $W$ and/or $Z$ decays

Another way of determining the calibration constant is to use reference physics processes with well-known cross section and sufficiently high rates. The  $W$  and  $Z$  production are very good candidates thanks to the small uncertainties in the theoretical prediction of the cross section. Indeed at  $\mathcal{L} = 10^{33} \text{ cm}^{-2}\text{s}^{-1}$  and  $\sqrt{s} = 14 \text{ TeV}$ , the vector bosons production rate is about  $1 \div 10 \text{ Hz}$ , the leptonic decay modes are clean and the background controllable. The integrated luminosity, in this case, is

$$\int \mathcal{L} dt = \frac{N - B}{\sigma_{th} AC} \quad (1.63)$$





**Figure 1.11:** Sketch of head-on collisions.

where  $N$  is the number of observed events,  $B$  the number of background events and  $\sigma_{th}$  the product of the production cross section by the leptonic branching ratio,  $A$  the geometric acceptance that relates the cross section in the fiducial volume to the full phase space and  $C$  the event reconstruction efficiency. By relating this luminosity to the measured rates in the luminometers an absolute calibration can be obtained.

In ATLAS,  $A$  and  $C$  have been evaluated with a systematic uncertainty of 1-2% while a precision of order of less than 5% is, at present, available for the theoretical calculations of  $\sigma_{th}$ , limited by the knowledge of the parton distribution functions. These uncertainties imply that the typical precision on the calibration constant using physics channels is of the order of 5%.

## 1.7 Calibration through van der Meer Scans

The luminosity calibration through beam-separation scans was originally proposed by Simon van der Meer at the ISR (*Intersecting Storage Ring* at CERN, the first hadron collider in 1968 [7]).

The underlying idea is to measure the parameters of the colliding bunches, namely the transverse dimensions of the beams, by varying the distance between the colliding beams in dedicated "scan sessions". Once measured such transverse sizes  $\sigma_{ix}$  and  $\sigma_{iy}$  and knowing the number of protons in the two beams, using the Eq. 1.34 the absolute luminosity at zero beam-separation from the beam parameters can be obtained (see Fig.1.11). By comparing such luminosity with the visible interaction rate  $\mu_{vis}$ , measured by the luminosity detectors, and using the Eq.(1.45), the visible  $pp$  cross section  $\sigma_{vis}$ , i.e. the calibration constant, can be determined. In order to achieve high accuracy, the scans are performed not during normal runs, but in controlled and optimized conditions.

### 1.7.1 Absolute Luminosity from Beam Parameters

The bunch luminosity in the transverse plane can be expressed in terms of colliding beam parameters and, for zero crossing angle, is given by

$$\mathcal{L}_b = f_r n_1 n_2 \int \rho_1(x, y) \rho_2(x, y) dx dy \quad (1.64)$$

where  $\rho_1(x, y)$  and  $\rho_2(x, y)$  are the particle densities in the transverse plane of the beam 1 and 2, respectively. Under the assumption that the particle densities may be factorized into independent horizontal and vertical components  $\rho(x, y) = \hat{\rho}_x(x) \hat{\rho}_y(y)$ , Eq.(1.64) becomes

$$\mathcal{L}_b = f_r n_1 n_2 \Omega_x(\hat{\rho}_{x_1}, \hat{\rho}_{x_2}) \Omega_y(\hat{\rho}_{y_1}, \hat{\rho}_{y_2}) \quad (1.65)$$

where

$$\begin{aligned} \Omega_x(\hat{\rho}_{x_1}, \hat{\rho}_{x_2}) &= \int \hat{\rho}_{x_1}(x) \hat{\rho}_{x_2}(x) dx \\ \Omega_y(\hat{\rho}_{y_1}, \hat{\rho}_{y_2}) &= \int \hat{\rho}_{y_1}(x) \hat{\rho}_{y_2}(y) dy \end{aligned} \quad (1.66)$$

Eqs.(1.66) are the so called *beam-overlap* integrals in the two transverse directions.

The method proposed by van der Meer was first introduced for continuous ribbon beams and it was generalized by Rubbia for elliptical bunched beams. The overlap integral, considering the  $y$  direction, is:

$$\Omega(\hat{\rho}_{y_1}, \hat{\rho}_{y_2}) = \frac{R_y(0)}{\int R_y(\delta_y) d\delta_y} \quad (1.67)$$

where  $R_y(\delta_y)$  is the visible rate measured by a certain luminosity detector during a  $y$ -scan when the two beams are separated by the distance  $\delta_y$  and  $\delta_y = 0$  is the case of *zero beam separation* (head-on collisions).

Defining the parameter  $\Sigma_y$  as

$$\Sigma_y = \frac{1}{\sqrt{2\pi}} \frac{\int R_y(\delta_y) d\delta_y}{R_y(0)} \quad (1.68)$$

and (similarly for  $\Sigma_x$ ), the bunch luminosity can be written as:

$$\mathcal{L}_b = \frac{f_r n_1 n_2}{2\pi \Sigma_x \Sigma_y} \quad (1.69)$$

Eq.(1.69) allows to determine the luminosity from the machine parameters by performing a pair of beam-separation scans in the  $x$  and  $y$  transverse

direction separately. It is a general expression because the  $\Sigma$  depends only upon the area of the luminosity curve and not upon its shape. In case of a Gaussian luminosity curve,  $\Sigma_y$  coincides with the standard deviation of the distribution.

The measurement of  $\Sigma_x$  and  $\Sigma_y$  are provided by the luminosity detectors only, while  $n_1$  and  $n_2$  are the only parameters evaluated from machine measurements.

### 1.7.2 Luminosity Calibration by Beam Separation Scans

Every luminosity algorithm needs a calibration that can be obtained equating the absolute luminosity obtained through the measurement of  $\Sigma_x$ ,  $\Sigma_y$ ,  $n_1$  and  $n_2$  during the scan and the luminosity measured by a particular algorithm at the peak of the scan curve:

$$\sigma_{vis} = \mu_{vis}^{MAX} \frac{2\pi\Sigma_x\Sigma_y}{n_1n_2} \quad (1.70)$$

Eq.(1.70) provides a direct calibration of the visible cross section  $\sigma_{vis}$  for each algorithm in terms of the peak visible interaction rate  $\mu_{vis}^{MAX}$ , the product of the convolved beam widths  $\Sigma_x\Sigma_y$  and the bunch population product  $n_1n_2$ .

In case of non-zero crossing angle, the luminosity distribution is wider by a factor that depends on the bunch length, the transverse beam size and the crossing angle. The peak luminosity is also reduced by the *same* factor. The increase of the measured value of  $\Sigma_x$  is thus cancelled by the decrease in the maximum of the distribution. Consequently, no correction is needed in the determination of  $\sigma_{vis}$  and the van der Meer scan is a completely general method for calibrating a luminometer.

In this context, the *specific luminosity* is also used, defined as

$$\mathcal{L}_{spec} = \frac{\mathcal{L}_b}{n_1n_2} = \frac{f_r}{2\pi\Sigma_x\Sigma_y} \quad (1.71)$$

The specific luminosity depends on the product of the convolved beam sizes and can be measured in the same scan by different luminometers and algorithms. It constitutes a direct check on the mutual consistency of the absolute luminosity scale provided by these methods.

In Sec.(2.4), the description of the van der Meer scans performed by LHC in the ATLAS interaction point in 2012 is given together with the systematic uncertainties affecting the detector calibration. These uncertainties will enter in the total systematic uncertainty affecting the measurement performed in this thesis.



## Chapter 2

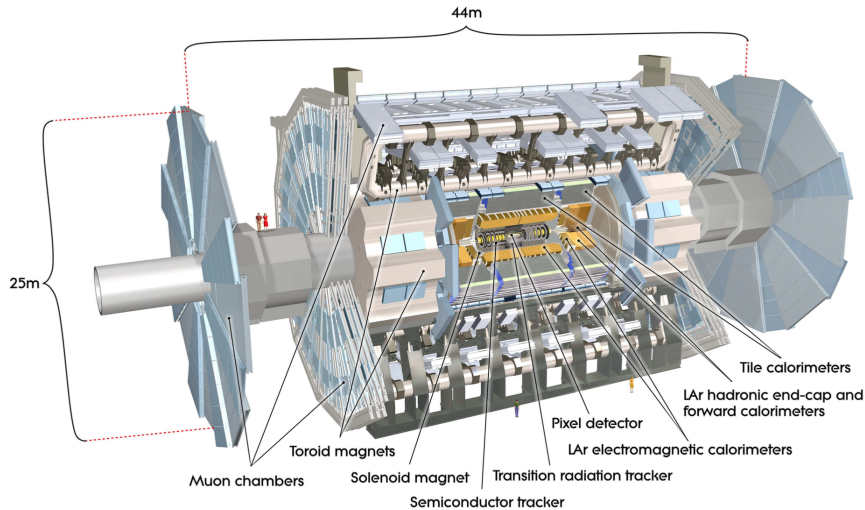
# Luminosity Determination at the ATLAS Experiment

At the ATLAS experiment, the luminosity is determined using several detectors and multiple algorithms in order to have a redundant measurement. Each of the used detectors has different acceptance, systematic uncertainties and sensitivity to background. The ratios of the luminosities obtained with different detectors are monitored as a function of time and  $\mu$  (the average number of interactions per bunch crossing) in order to quantify the systematic uncertainties on the measurement. The absolute luminosity calibration is performed with beam separation scans independently for the various algorithms and detectors.

### 2.1 The ATLAS Experiment

The ATLAS (*A Toroidal LHC ApparatuS*) detector [9] is one of the general purpose experiment of LHC and it is nominally forward-backward symmetric with respect to the interaction point. Its dimension are 25 m in height and 44 m in length, while the weight is approximately 7000 tones. The magnet configuration comprises a thin superconducting solenoid surrounding the Inner Detector cavity, and three large superconducting toroids (one barrel and two end-caps) arranged with an eight-fold azimuthal symmetry around the calorimeters. This choice has driven the design and the development of the rest of the detector, Fig. 2.1.

The coordinate system used to describe the ATLAS detector has its origin in the nominal interaction point. The beam direction defines the  $z$ -axis and the  $x - y$  plane is transverse to the beam direction. The positive  $x$ -axis is defined



**Figure 2.1:** The ATLAS Experiment

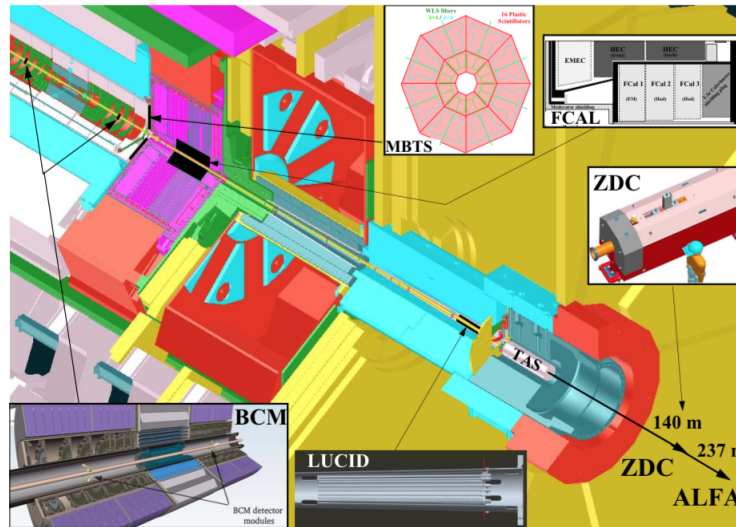
pointing from the interaction point to the center of the LHC ring, while the positive  $y$ -axis is defined pointing upwards. ATLAS is ideally divided in a side- $A$  and a side- $C$ , the former corresponding to the positive  $z$ , the latter to the negative  $z$ . The azimuthal angle  $\phi$  is measured around the beam axis and the polar angle  $\theta$  is the one from the beam axis. The pseudorapidity is defined as  $\eta = -\ln(\theta/2)$ , but, when the objects are massive, the rapidity  $y = 1/2 \ln[(E + p_z)/(E - p_z)]$  is used. In the pseudorapidity-azimuthal space, the distance  $\Delta R$  is defined as  $\Delta R = \sqrt{\Delta\eta^2 + \Delta\phi^2}$ . A brief description of the ATLAS subsystem for the luminosity measurement follows.

## 2.2 ATLAS Luminosity Sub-detectors

The ATLAS strategy to understand and control systematic uncertainties affecting the luminosity determination is to compare measurements from different approaches. The measurements of the inelastic  $pp$  rate are performed with multiple event and hit counting algorithms that are different in their statistics and background sensitivity as well as particle counting algorithms which exploit totally different observables. The ATLAS luminosity community chooses one *preferred* detector and algorithm and the measurement provided is called the "*ATLAS preferred*".

Offline and Online preferred algorithms have to be distinguished: the former is used for physics analysis, the latter is used to provide fast-feedback to LHC on the luminosity conditions at IP1. Long-term stability, independence

from changing the running conditions and reliability in a large range of luminosity scales, independence of dead-time and the ability to determine the luminosity at the *per-bunch* level (i.e. separately for each colliding bunch) are the main requirements for the ATLAS preferred method. In Fig.(2.2) the

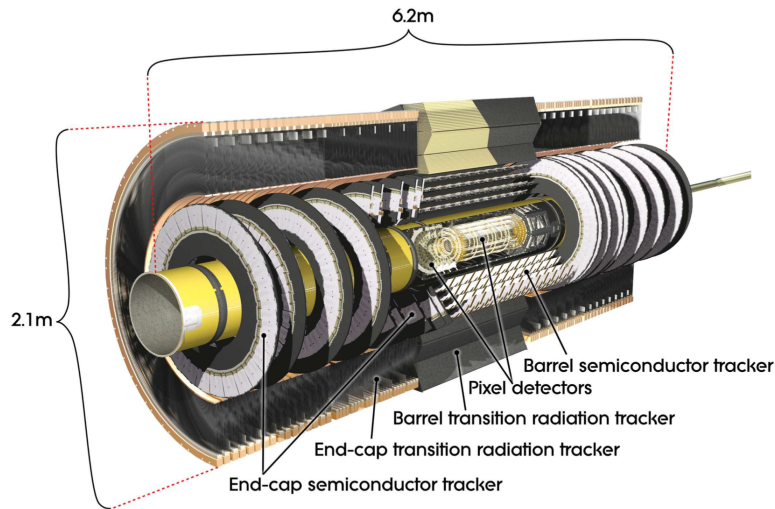


**Figure 2.2:** The ATLAS Luminosity detectors.

main luminosity detectors within ATLAS are shown. Most of them have two stations on either side of the IP (side A and side C), which allows to perform coincidence requirements.

### 2.2.1 The Inner Detector

In order to achieve a precise momentum and vertex resolution, the Inner Detector (ID) is composed of high granularity detectors exploiting different technologies: pixel and silicon microstrip in the Semiconductor Trackers (SCT) and straw tubes in the Transition Radiation Tracker (TRT). In Fig(2.3), a view of the ATLAS Inner Detector. The ID is immersed in a 2 T solenoidal magnetic field. The precision tracking detectors are composed by pixel and silicon microstrips and they cover the pseudorapidity region  $|\eta| < 2.5$ . In the barrel region, they are disposed in cylindric symmetry around the beam axis while in the end-cap ones they are located perpendicularly to the beam axis. The pixel layers are segmented in  $R - \phi$  and  $z$  with typically three pixel layers crossed by each track. All pixel sensors have a minimum pixel



**Figure 2.3:** Inner Detector

size  $(R - \phi) \times z$  of  $50 \times 400 \mu\text{m}^2$ . The pixel detector has 80.4 million readout channels [10].

For SCT, eight strip layers are crossed by each track. In the barrel region, it uses small-angle stereo strips to measure both coordinates, with one set of strips in each layer parallel to the beam axis, measuring  $R - \phi$ . They consist of two 6.4 cm long daisy-chained sensors with a strip pitch of  $80 \mu\text{m}$ . The total number of read-out channels in the SCT is 6.3 million [11].

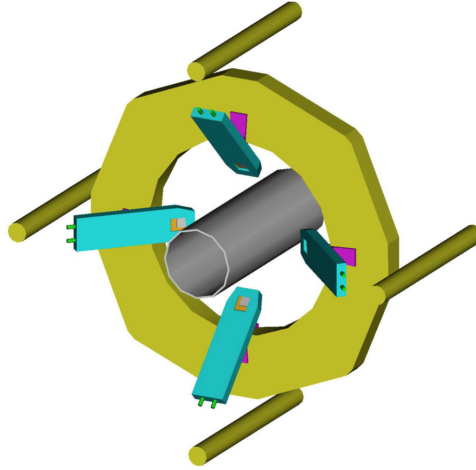
The track-following is possible thanks to the TRT, which provides a large number of hits (typically 36 per track) thanks to the straw tubes. TRT gives only  $R - \phi$  information. In the barrel region, the straws are parallel to the beam axis and are 144 cm long, with their wires divided into two halves, approximately at  $\eta = 0$ . In the end-cap region, the straw is 37 cm long and arranged radially in wheels. The total number of TRT readout channels is 351000 [12].

The ID system provides tracking measurements and allows the electron identification by the detection of the transition-radiation photons in the xenon-based gas mixture of the straw tubes. The semiconductor trackers also allow parameter measurements and vertexing.

### 2.2.2 BCM

The task of the *Beam Condition Monitor* (BCM) [13] is to monitor beam losses and provide fast signals that will abort the beam safely if the loss rates become dangerous. It also provides bunch-by-bunch luminosity mea-





**Figure 2.4:** Schematic illustration of 4 BCM stations. Two identical modules are mounted in the two sides of ATLAS. The horizontal and vertical modules deliver separate luminosity measurements.

measurements. The BCM consists of two sets of four modules mounted symmetrically at a positions of  $z_{BCM} = \pm 1.84$  m and at a radius of 55 mm with respect to the beam axis, on each side of the IP, Fig (2.4).

The sensors are made of 500  $\mu\text{m}$  thick radiation hard polycrystalline chemical vapor deposition diamonds and they are mounted with a tilt of  $45^\circ$  with respect to the beam axis. The low acceptance of the BCM requires each sensor to be sensitive to single minimum ionization particles (MIPs). A fast readout ( $\approx 2$  ns) enables the measurement on a per-bunch level and allows to measure time of flight and pulse amplitudes. In order to expand the dynamic range each signal is split into a high and low amplitude channel. The low-threshold channels have MIP sensitivity and are suited for luminosity determination. All signals are then transmitted over 70 m optical fibers and one readout path uses the low-threshold channels of the four horizontal modules, which is called BCM-H, another one uses the low-threshold channels of the vertical modules, which is called BCM-V. In this way, the BCM delivers two independent measurements that can be used for cross-checks. Both the BCM-V and BCM-H exploit event counting methods to determine the luminosity. These methods include inclusive algorithms (BCMFOR, BCMHOR), single side inclusive algorithms (BCMFORC, BCMHORC) and coincidence algorithms (BCMFORAND, BCMHORAND). In 2012 BCM was used as a preferred detector for the ATLAS luminosity measurement.

### 2.2.3 LUCID

LUCID (*L*uminosity measurements using *C*herenkov *I*ntegrating *D*etectors) [14] is the only ATLAS detector uniquely dedicated to luminosity measurements. It is composed by two modules on each side of the IP, at a distance of approximately  $\pm 17$  m from the IP and at a radial distance of 10 cm from the beam line ( $|\eta| \pm 5.8$ ). Each module consists of 20 aluminium tubes that are arranged along the beam line.

The tubes have a diameter of 15 mm. In the original project, they were filled with  $C_4F_{10}$  used as Cherenkov radiator for charge particles at a pressure of  $1.2 \div 1.4$  bar, providing a Cherenkov threshold of 2.8 GeV for pions and 10 MeV for electrons. The Cherenkov light produced by charged particles was collected by the PMTs installed at the end of each tube. Due to the large migration effects produced by secondary particles crossing the tubes at large angles, the detector was emptied in the 2012 data taking leaving the quartz PMT windows to act as active areas. Therefore the Cherenkov light is now produced by charged particles crossing the PMT windows.

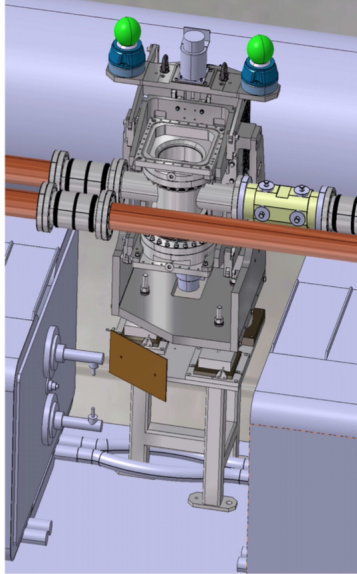
The signals of all PMTs are sent to the readout system where a dedicated electronic board applies luminosity algorithms at the per-bunch level. Additional to the algorithms used by BCM, hit-counting algorithms are also available with LUCID.

### 2.2.4 ALFA

ALFA (*A*bsolute *L*uminosity *F*or *A*TLAS) [14] is a system of detectors for the measurements of elastic scattering in the Coulomb-Nuclear interference region. The detector is aimed to the measurement of the luminosity with 2-3% error and the measurement of the elastic and total  $pp$  cross section, see Sec.(3.6.4). The detector must approach the beam to about 1.5 mm in order to measure the particles scattered at very small angles. The subdetectors used to achieve this goal are the so-called *Roman Pots* (Fig.2.5), a system integrated with the beam pipe and able to move the detector close to the beam. ALFA is made of two arms situated at 240 m from the interaction point at either sides of ATLAS. Each module is composed by 2 groups of scintillating plastic fibers, mounted at  $90^\circ$  with respect to each other. A detailed description of ALFA is given in Sec. (2.2.4).

### 2.2.5 The Calorimeters: FCAL and TileCal

An independent measurement of the luminosity is performed using the ATLAS calorimeters to provide a cross-check of the stability and non-linearities



**Figure 2.5:** A schematic view of a Roman Pot.

of the main luminosity subdetectors. The PMT current drawn in TileCal modules and the current drawn across the liquid argon gaps in the FCAL modules are used. As described in Sec. (1.5.4), such currents are proportional to the particle fluxes across the calorimeters, which is in turn proportional to the luminosity. The measurement is performed once per LB meaning that, differently with respect to the BCM and LUCID case, it is not a per-bunch measurement. Due to the small sensitivity of the PMT-current measurement at low particle fluxes (low  $\mu$ ), the calibration in the vdM scans is not possible. A detailed description of the luminosity measurement of TileCal and FCAL is reported [15].

## 2.3 ATLAS Luminosity Algorithms

### 2.3.1 Online Algorithms

The online luminosity monitoring [16] can be used to provide luminosity information for machine tuning independently of the "busy" state of the acquisition system and the status of the other detectors. The calculation and publication of instantaneous luminosity data is performed by the *Online Luminosity Calculator* (OLC) and the results are displayed in the ATLAS control room and sent to the LHC operators with a frequency of about 1 sec for fast feedback on the accelerator tuning. The task of the OLC is to

collect the raw information such as event and hit counts, number of colliding bunches, number of LHC orbits in time observed interval and then determine  $\mu$  and the measured luminosity. Due to the small time allowed for online luminosity measurement, no background subtraction is performed. The OLC outputs are the instantaneous luminosities averaged on the number of colliding BCIDs, computed for all luminosity algorithms. Thanks to the OLC values, a collision optimization at IP1 is possible.

Most methods provide an LB-averaged luminosity measured from colliding bunches only, but for different detectors the requirement is imposed at different stages of the analysis. The BCM and the LUCID readout boards provide bunch-by-bunch luminosity information for each LB, as well as the luminosity per LB summed over all colliding BCIDs. For these two detectors the OLC calculated the *bunch-integrated* luminosity using the following sum over all colliding BCIDs:

$$\mathcal{L} = \sum_{i \in BCID} \frac{\mu_i^{vis} f_r}{\sigma_{vis}} \quad (2.1)$$

BCM uses only two of its four sides for online luminosity determination and three algorithms are implemented in the firmware of the BCM readout driver:

- BCM\_Event\_OR counts the number of events per BC in which at least one hit above the threshold occurs on either the A-side, the C-side or both within a 12.5 ns window centered on the arrival time of particles, coming from the IP1.
- BCM\_Event\_AND counts the number of events per BC where at least one hit above the threshold is observed, within a coincidence window of 12.5 ns, both on the A and C side.
- BCM\_Event\_XORC counts the number of events per BC where at least one hit above threshold is observed in the C-side and with none on the A-side within the same 12.5 ns window.

LUCID has four algorithms implemented in the readout board:

- LUCID\_Hit\_OR reports the mean number of hits per BC. In this algorithm, hits are counted for any event where there is at least one hit in any one of the 16 tubes in either detector side in one BCID.
- LUCID\_Hit\_AND reports the mean number of hits per BC and the event must contain one hit in each of the two sides of the detector within a BCID.

- LUCID\_Event\_AND reports the number of events with at least one hit on each detector side.
- LUCID\_Event\_OR reports the number of events with one hit on any of the sides of the detectors.

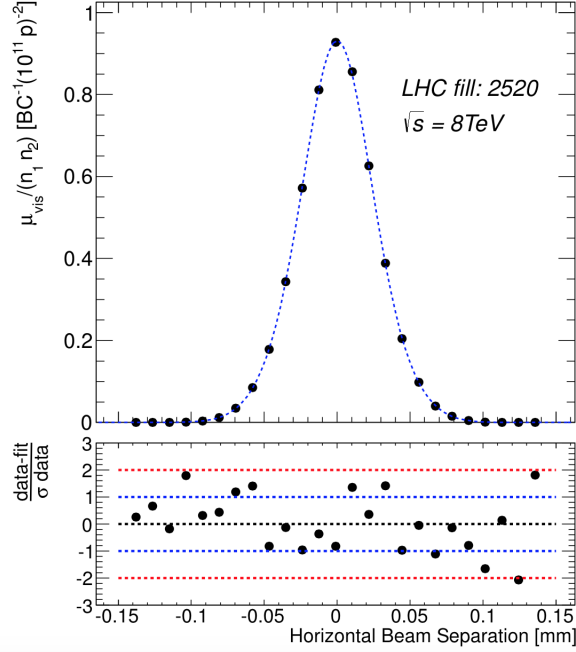
### 2.3.2 Offline Algorithms

For LUCID and BCM, the same algorithms used online are also implemented offline [16]. Additional single-side OR algorithms (ORA and ORC) are implemented. The Tile, the Forward calorimeter and the tracking system also contribute to the measurement. Offline analysis has no stringent time limitations and therefore a background subtraction can be performed. The offline luminosity can be moreover updated once more precise calibration are available which is not the case for the online algorithms.

## 2.4 ATLAS Luminosity Calibration

In 2012, to calibrate the luminosity detector ATLAS exploits the van der Meer calibration procedure (see Sec.1.7). Three sessions were performed in April, July and November 2012 in order to calibrate the luminosity detector along the whole data taking period. The main features of such scans are reported in Tab. 2.1, [17]. The procedure followed to perform the vdM scans is very time-consuming and technically challenging. It consists normally on the following steps:

- The horizontal scan is performed starting at zero nominal separation and moving to the maximum separation in negative direction, stepping back to zero and then again to the maximum positive direction. The maximum separation is  $6 \sigma_b$  where  $\sigma_b$  is the nominal transverse size of the beam. The maximum beam separation is scanned in 25 steps. Finally, it returned to the nominal zero separation.
- An identical procedure is then reported for the vertical plane.
- In each scan of 25 steps in relative displacement, the beams is left in a quiescent state for about 30s. In this time interval, relative luminosities are measured by active luminosity monitors and recorded, as a function of time, in a dedicated online-data stream, together with the nominal separation, the beam currents and other relevant accelerator parameters transmitted to ATLAS by the accelerator control system.



**Figure 2.6:** Specific interaction rate as a function of the nominal beam separation for the BCMV\_EventOR algorithm in the horizontal scanning direction ( $x$ ). The residual deviation of the data from a double Gaussian plus constant background fit, normalized to the statistical uncertainty at each scan point, is shown in the bottom panel.

The specific  $\mu_{vis}$  distribution measured by BCMV\_EventOR algorithm is shown in Fig.2.6 as a function of the beam separation. Various fitting functions are used to determine, from the distribution of Fig.2.6 the  $\Sigma_x$  ( $\Sigma_y$ ) transverse beam widths which are two of the parameters needed for the luminosity calibration as from Eq.1.71. For all detectors and algorithms the use of a double Gaussian with a flat background results in a  $\chi^2$  per degree of freedom close to one. The other quantity to be determined to measure the calibration constant  $\sigma_{vis}$  is the rate corresponding to zero-beam separation ( $R_{MAX}$ ) while the bunch intensities  $n_1$  and  $n_2$  are provided by the accelerator.

Knowing these quantities, the calibration constant can be determined as:

$$\sigma_{vis} = \frac{R^{MAX}}{\mathcal{L}^{MAX}} = R^{MAX} \frac{2\pi\Sigma_x\Sigma_y}{n_b f_r (n_1 n_2)_{MAX}} \quad (2.2)$$

Since the measurements in the horizontal and vertical plane are independent,  $R^{MAX}$  is the average of  $R_x^{MAX}$  and  $R_y^{MAX}$ .

Date	16 April 2012	19 July 2012	22, 24 November 2012
LHC Fill Number	2520	2855, 2856	3311, 3316
Center-of-mass energy (TeV)	8	8	8
Scan Labels	I-III	IV-IX	X-XV
Scan Sequence	3 sets of centered H+V scans	4 sets of centered H+V scans plus 2 sets of H+V off-axis scans	4 sets of centered H+V scans plus 2 sets of H+V off-axis scans
Total Scan Steps per Plane	25	25	25
Maximum beam separation	$\pm 6\sigma_b$	$\pm 6\sigma_b$	$\pm 6\sigma_b$
Scan Duration per Step	20 s	30 s	30 s
Total number of bunches per beam	48	48	39
Number of bunches colliding in ATLAS	35	35	29
Typical number of protons per bunch [ $n_{1,2}$ ]	$0.6 \cdot 10^{11}$	$0.9 \cdot 10^{11}$	$0.9 \cdot 10^{11}$
Nominal $\beta$ -function at the IP [ $\beta^*$ ] (m)	0.6	11	11
Approximate transverse emittance [ $\epsilon_N$ ] ( $\mu\text{m-radians}$ )	2.3	3.2	3.1
Approximate transverse single-beam size [ $\sigma_b$ ] ( $\mu\text{m}$ )	18	91	89
Nominal half crossing angle ( $\mu\text{rad}$ )	$\pm 145$	0	0
Typical luminosity/bunch ( $\mu\text{b}^{-1}/\text{s}$ )	0.8	0.09	0.09
$\mu$ (interactions/crossing)	5.2	0.6	0.6

**Table 2.1:** Summary of the main characteristics of the 2012  $vdM$  scans performed at the ATLAS interaction point.

While  $R^{MAX}$ ,  $\Sigma_x$  and  $\Sigma_y$  are provided by the luminosity detectors, beam currents are measured by two different LHC system: *Fast bunch-current transformers* and *Direct-Current Current Transformers*.

The FBCTs are AC-coupled, high-bandwidth devices which use gated electronics to perform continuous measurements of individual bunch charges for each beam. The DCCTs measure the total circulating intensity in each of the two beams. The latter have better accuracy but needs to average over hundreds of seconds to achieve the precision. The bunch-by-bunch currents are therefore measured by FBCT. The absolute scale of the bunch intensities  $n_1$  and  $n_2$  is determined by rescaling the total circulating current measured by the FBCT to the more accurate DCCT measurements.

In Tab. (2.1) the main characteristics of the van der Meer scans performed in 2012 are reported.

## 2.5 Systematic Uncertainties in the Luminosity Measurement in 2012

### 2.5.1 Systematic Uncertainties in the Absolute Luminosity Calibration

The main sources of systematic uncertainties [16] on the measurement of  $\sigma_{vis}$  from van der Meer calibration scans are summarized in the following list and their evaluation is presented in Tab.(2.2) [17].

- **Beam centering.** The two beams are not perfectly centered in the non-scanning plane at the start of a  $vdM$  scan, the assumption that

the luminosity observed at the peak is equal to the maximum head-on luminosity is not completely true.

- **Beam-position jitter.** At each step of the scan, the actual beam separation may be affected by random deviations of the beam positions from their nominal setting, causing fluctuations in the luminosity measurements at each scan point.
- **Bunch-by-bunch consistency of visible cross section measurements.**  $\sigma_{vis}$  value for a given detector or algorithm should be an universal scale factor independent of machine conditions and equal for all colliding bunches. The bunch-by-bunch spread in  $\sigma_{vis}$  is taken into account in the systematic uncertainty evaluation.
- **Emittance growth and other sources of non-reproducibility.** This calibration method assumes that the luminosity and the convolved beam sizes  $\Sigma_{x/y}$  are constant within a single  $x$  or  $y$  scan. A variation in the transverse emittance during the scan results in a distortion of the scan curve shape. An emittance growth between scans would manifest itself by a slight increase, from one scan to the next, of the measured value of  $\Sigma$  and, consequently, by a decrease of the peak specific luminosity.
- **Fit model.** The  $vdM$  scan data are analysed using a fit to a double Gaussian, plus a constant term interpreted as a single-beam background. Refitting the data with two different model assumptions (a single Gaussian multiplied by a fourth-order polynomial plus a constant and a single Gaussian multiplied by a sixth-order polynomial plus a constant) lead to different values of  $\sigma_{vis}$ . The maximum fractional variation between the scan averaged results of these different fit assumptions is used as uncertainty associated to the fit model.
- **Background subtraction.** The uncertainty associated with potential backgrounds to the luminosity signal is estimated using double Gaussian plus constant term as baseline fit model and comparing the bunch and scan averaged cross section, assuming :
  - either that the constant term results from luminosity-independent background sources;
  - or that the background is negligible and that the constant term integrated out to the scan limits of  $\pm 6\sigma_b$  is a pure luminosity contribution to the scan integral.



Taking the maximum deviation between these two assumptions as a measure of the systematic error, an uncertainty of  $\pm 0.06\%$  arises.

- **Reference specific luminosity.** The transverse convolved beam sizes  $\Sigma_{x/y}$  measured by the *vdM* scan are related to the reference specific luminosity, see Eq.(1.71). Each detector and algorithm should measure identical values from the scan curve fits. The visible cross section value extracted from a set of *vdM* scans for a given detector and algorithm uses the specific luminosity measured by the same detector and algorithm. The difference in  $\Sigma$  as measured by different detectors is also considered in the systematic uncertainties.
- **Lenght-scale calibration.** In the *vdM* scan technique, it is important to know the beam separation at every scan point, the ability to measure  $\Sigma_{x,y}$  depends, in fact, upon knowing the absolute distance by which the beams are separated during the scan procedure. This absolute distance is monitored by a set of closed orbit bumps applied locally near the ATLAS IP using steering correctors. Dedicated length scale separation measurements are performed close to each *vdM* scan set using the same collision-optics configuration. Lenght scale scans are performed by displacing the beams in collision by five steps over a range of up to  $\pm 2.5 \sigma_b$ . Since the beams remain in collision during the scans, the actual position of the luminous region can be determined with high accuracy using the primary vertex position reconstructed by the ATLAS tracking detectors.
- **Absolute lenght scale of the ATLAS Inner Detector.** The determination of the lenght scale relies on comparing the scan step requested by the LHC with the actual trasverse displacement of the luminous centroid measured by ATLAS. This depends on the length-scale of the ATLAS Inner Detector (ID) and its capability of measuring displacements of vertex positions away from the center of the detector. The uncertainty on this absolute scale is evaluated by analysing simulated Monte Carlo events using several different misaligned ID geometries.
- **Beam-beam effects.** The beam-beam interactions have already been discussed in Sec. 1.2. These effects can cause a mutual de-focusing of the two colliding bunches.
- **Transverse correlations.** In presence of linear  $x - y$  coupling in either beam and assuming the horizontal and vertical emittances to be sufficiently different, the luminosity distribution as a function of the

beam-separation in the  $x - y$  plane may transform from an upright ellipse into a tilted ellipse, with a potential underestimation of  $\Sigma_x$  and  $\Sigma_y$ .

- **$\mu$ -dependence.** Potential non-linearities with the average number of interactions for bunch crossing in the different detectors can affect the shape of the distribution in Fig.(2.6) leading to an error in the measurement of  $\Sigma_x$  and  $\Sigma_y$ .
- **Bunch-population product.** The bunch-by-bunch fraction determination has to be considered for the systematic uncertainty determination and additional corrections have to be applied for *satellite bunches* and *ghost charge*. The *satellite bunches* refers to protons captured in an LHC RF bucket with a nominally filled BCID, but separated from the nominal bucket by a multiple of the LHC RF period. Their current is integrated by both the DCCT and the FBCT, even though these protons do not contribute to the luminosity produced by collisions between the nominal bunches. The *ghost charge* refers to protons, both captured and unbunched, that populate any RF bucket outside the nominally colliding BCIDs and whose charge is integrated by the DCCTs but remains below the threshold for the FBCTs.

The overall systematic uncertainty in the calibration due to the listed sources is evaluated to be 3.27% in 2012, see Tab.(2.2). This value directly enters in the overall systematic uncertainty of the luminosity measurement, together with the contributions due to instrumental effects along the whole data taking which are discussed in the next section.

### 2.5.2 Systematic Uncertainties on Luminosity Extrapolation

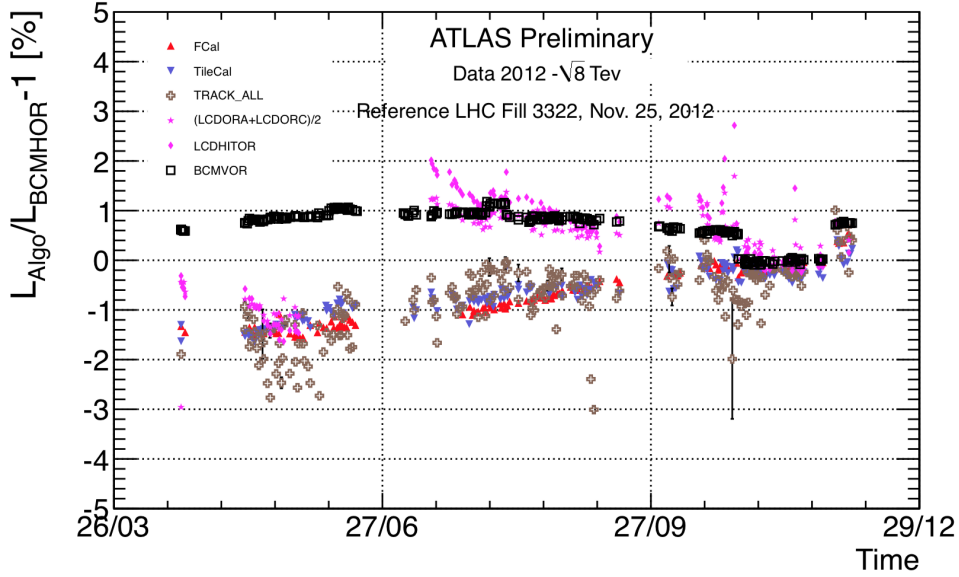
Additional to the systematic uncertainties related to the detectors calibration, other sources of uncertainties are to be considered related to the detector operation at high luminosity during the physics data taking [17]. In order to produce the integrated luminosity values used in ATLAS physics analysis, a single algorithm was chosen to provide a central value for a certain data-taking period, while the remaining calibrating algorithms are used as cross-checks to test the reliability of the result. In 2012, the BCMH\_EventOR algorithm has been used because of its availability over the whole data taking. The other detectors (LUCID, FCAL, TileCAL) were used to evaluate the systematic uncertainties on the main luminosity measurement.

Year	2012
Fill Number	2520
Beam Centering	0.80%
Beam-position jitter	0.60%
Bunch-to-bunch $\sigma_{vis}$ consistency	0.29%
Emittance growth	2.06%
Fit Model	0.21%
Background subtraction	0.06%
Specific luminosity	0.70%
Lenght scale calibration	0.10%
Absolute ID lenght scale	0.30%
Beam-beam effects	0.50%
Transverse correlations	2.00%
$\mu$ dependence	0.50%
Scan subtotal	3.25%
Bunch-population product	0.38%
Total	3.27%

**Table 2.2:** Relative systematic uncertainties on the determination of the visible cross section  $\sigma_{vis}$  from the  $vdM$  scans of April 2012 at  $\sqrt{s} = 8$  TeV.

The following systematic uncertainties were considered and evaluated for the physics runs in 2012.

- **Subtraction of Background.** Both LUCID and BCM observe some activity in the empty BCIDs immediately following a collision. This is attributed to a background component, often called *afterglow*. Different approaches for the afterglow subtraction were used leading to a systematic effect of 0.2% (See Sec. 4.5).
- **Long-term stability.** A possible source of uncertainty is the assumption that the  $\sigma_{vis}$  determined in set of  $vdM$  scans is stable across the entire 2012 data set. Several effects can in fact degrade the long-term stability of a given detector, including slow drifts in the detector response and sensibility with a corresponding variation in the LHC beam conditions, in particular the total number of colliding bunches. In Fig.(2.7), the percentage deviations, with respect to BCM\_HOR, between the integrated luminosity measured by different detectors for all the runs acquired in 2012 are shown as a function of time. A normalization of all measurement in a run at the end of the data taking is done, so that relative variations with respect to this run are shown. From

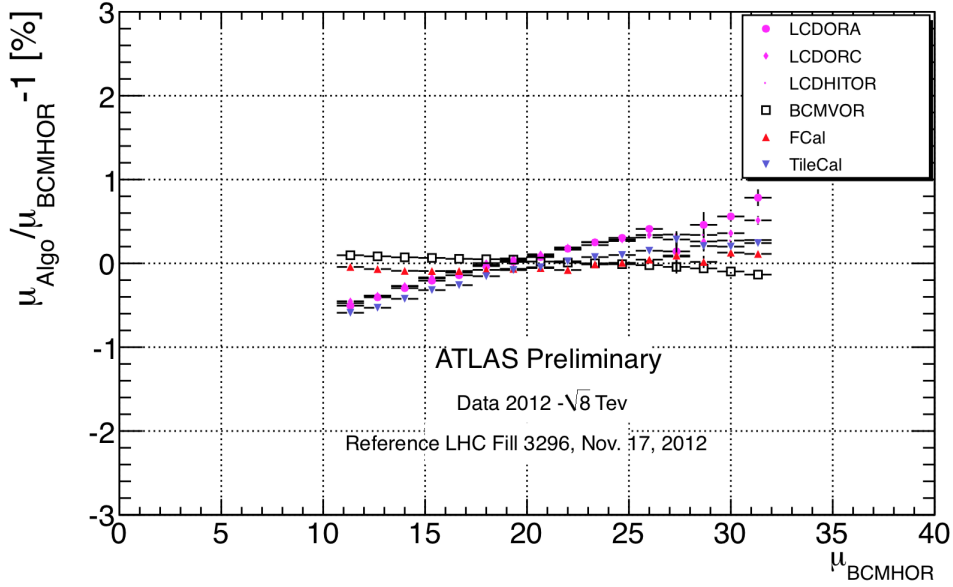


**Figure 2.7:** Percentage deviations between the integrated luminosity measured by different detectors with respect to BCMHOR and as a function of time in 2012.

the figure a maximum systematic uncertainty of 2% can be quoted all over 2012.

- **$\mu$ -dependence.** Another source of uncertainties is the linearity of the luminosity algorithms as a function of the number of interactions per crossings. The comparison among the response of various detectors as a function of  $\mu$  is used to evaluate such an effect. From Fig.(2.8) a maximum systematic uncertainty of 0.5% can be estimated as  $\mu$  dependence during normal physics runs ( $10 \lesssim \mu \lesssim 35$ ).

In Tab.(2.3), the various contributions to the total systematic uncertainty affecting the 2012 luminosity measurement are reported. A total systematic uncertainty of about 3.9% is evaluated for the high-luminosity operation. This table will be used in Sec.(4.5) to derive some of the systematic uncertainties affecting the measurement discussed in this thesis.



**Figure 2.8:** Percentage deviations of the measurement of  $\mu$  from different detectors and algorithms with respect to BCM\_HOR as a function of  $\mu_{BCM\_HOR}$ .

Uncertainty Sources	$\partial\mathcal{L}/\mathcal{L}$
Bunch-population product	0.38%
Other calibration uncertainties ( $vdM$ )	3.25%
Afterglow correction	0.20%
Long-term consistency	2.00%
$\mu$ -dependence	0.5%
Total	3.87%

**Table 2.3:** Main sources of systematic uncertainties on the calibrated luminosity.



## Chapter 3

# Measurement of the Total Cross Section from Elastic Scattering in $pp$ Collisions at $\sqrt{s} = 7$ TeV in 2011

In order to obtain the total  $pp$  cross section at LHC at  $\sqrt{s} = 7$  TeV, an integrated luminosity of about  $80 \mu b^{-1}$  was accumulated for the measurement of the differential elastic cross section as a function of the Mandelstam momentum transfer variable  $t$ . The measurement was independently performed both by ATLAS (using ALFA) and by TOTEM.

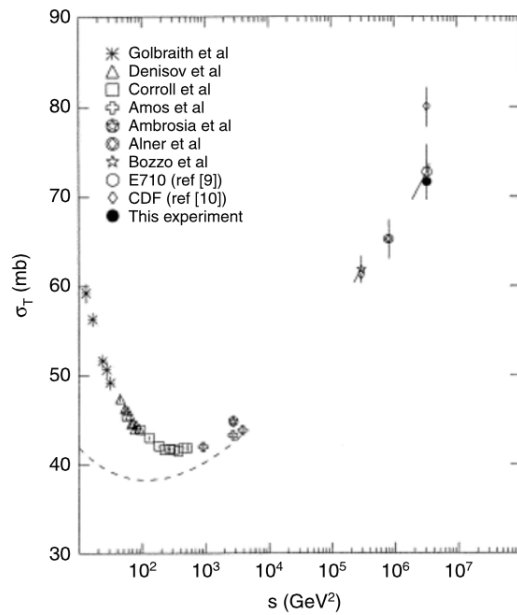
### 3.1 The Total Hadronic Cross Section

The total hadronic cross section is a fundamental parameter of strong interactions theory. Fundamentally, it sets the size of the interaction region at a given energy [20].

The hadronic processes are described by the *Quantum Chromodynamics* (QCD), the non-Abelian gauge theory of strong interactions. Due to the non-Abelian nature of theory, the gluons themselves carry a color charge and can therefore interact with other gluons. The strong force is characterized by a running coupling constant  $\alpha_s$  and the color charge is small at short distances and large at large distances. This characteristics creates two different regimes named, respectively, *asymptotic freedom* and *confinement*. In hadron-hadron collisions, these correspond to *hard scattering* and to *soft scat-*

*tering*. The former is characterized by small distances and large momentum transfer, while the latter by large distances and small momentum transfer. To describe hard interactions, QCD has successfully used a *perturbative* approach, but this is not possible for the soft ones because of the rise of the coupling constant with the decrease of the momentum transfer.

Soft scattering embodies elastic collisions and diffractive dissociation and



**Figure 3.1:** Dependence of the total cross section from the centre-of-mass energy.

they constitute a crucial problem for the theory of strong interaction. The lack of a pure QCD result for the elastic scattering constitutes a serious issue for the theoretical investigation of the *total* hadronic cross section. Experimental observations may help the comprehension of a possible development of the theory in the soft sector, at least as it concerns the *forward* elastic scattering amplitude.

The total cross section is defined by

$$\sigma_{tot} = \sigma_{el} + \sigma_{inel} = \frac{N_{el} + N_{inel}}{\mathcal{L}} \quad (3.1)$$

where  $\mathcal{L}$  is the luminosity and  $N_{el}$  and  $N_{inel}$  are the rate of elastic and inelastic interactions. The definition in Eq. (3.1) opens to two interpretations. The first one is statistical, that connects  $\sigma_{tot}$  to a probability of interaction,

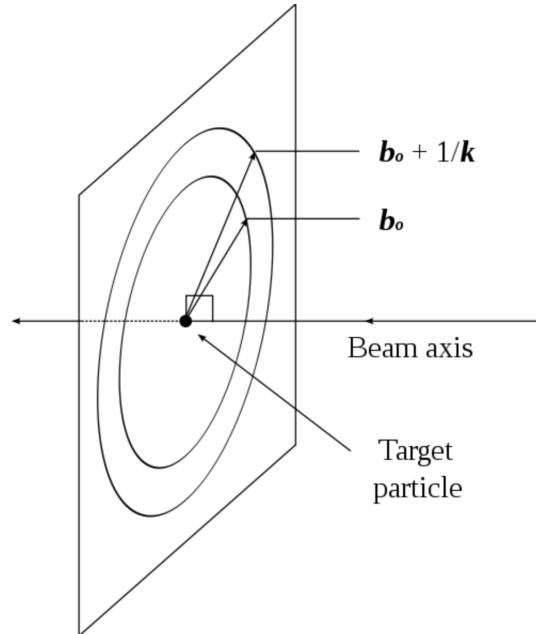


the second one is geometrical, where  $\sigma_{tot}$  represents the effective area of interaction, usually measured in  $mb$  for hadronic scattering.

The growth of the  $pp$   $\sigma_{tot}$  with the center of mass energy is an experimental fact (see Fig.3.1), confirmed in every energy regime at different colliders, but the *Froissart - Martin* bound states that  $\sigma_{tot}$  cannot grow asymptotically faster than  $\ln^2 s$ , where  $\sqrt{s}$  is the centre-of-mass energy [18].

$$\sigma_{tot}(s) < \frac{\pi}{m_\pi} \cdot \ln^2 \frac{s}{s_0} \quad (3.2)$$

where  $m_\pi$  is the mass of the pion. The nuclear force is in fact typically mediated by mesons, the lightest of which is the pion. While in classical mechanics, this exchange isn't possible because of the violation of the energy conservation, in quantum mechanics this is possible thanks to the so-called *tunnel effect*. The probability of the tunnel effect decreases exponentially with the distance. The maximum is reached when the incident particle is closest to the target particle, at a distance  $b$  (called *impact parameter*), perpendicular to the incident line-of-flight, see Fig.(3.2). There are two cases to



**Figure 3.2:** Pictorial view of the incident particle beam and the related target particle. Within a circle of radius  $b_0$  in the plane of the target particle, the scattering probability cannot be larger than 1. Outside, it's not negligible essentially in a ring of width  $1/k$ . The total cross section is bounded by  $\pi(b_0 + 1/k)^2$ .

be considered:

- for  $b < b_0$ , the force of the interaction is not affected by the tunnel effect. The interaction probability is less than, or equal to, 1.
- for  $b > b_0$ , the tunnel effect wins and the interaction probability is bounded by the exponential  $exp(kb_0 - kb)$ , since it's constrained to be one at  $b = b_0$ .

After some calculus, the total probability is obtained:

$$\sigma = \pi(b_0 + 1/k)^2 \quad (3.3)$$

The quantity  $k$  is given by the theory of tunnel effect and it's related to the mass of the lightest meson that can be exchanged, i.e. the pion,  $k = \frac{mhc}{2\pi}$ . Intrinsic couplings of particles are generally accepted not to increase faster than some power of the center-of-mass energy  $s$  as it becomes very large. The crucial point is the determination of the impact parameter  $b_0$  that is given by

$$Cs^n exp(-kb_0) = 1 \quad (3.4)$$

and thus

$$b_0 = \frac{nlns + lnC}{k} \quad (3.5)$$

where  $s$  in the centre-of-mass energy,  $n$  and  $C$  are constants. The essential outcome of this reasoning is that the total cross section, which is bounded by  $\pi(b_0 + 1/k)^2$  does not increase faster than  $ln^2s$ , multiplied by some constant. This is expressed by the Froissart bound (Eq.3.2).

Although there are several theoretical boundaries on the total cross section that can predict the general trend of the energy dependence of  $\sigma_{tot}$ , no precise predictions on energy dependence can be done.

For this reason the experimental measurement of the cross section in  $pp$  and  $p\bar{p}$  at increasing centre-of-mass energy at LHC is crucial.

## **3.2 Measurement of $\sigma_{tot}$ with Elastic Scattering through Optical Theorem**

The total cross section at hadron colliders can be measured via elastic scattering using the *Optical Theorem* [19] which links the rate of elastic interaction to the total cross section. The total cross section is related to the imaginary part of the forward elastic scattering amplitude via:

$$\sigma_{tot} \propto Im[f_{el}(t \rightarrow 0)] \quad (3.6)$$

where  $f_{el}(t \rightarrow 0)$  is the elastic scattering amplitude extrapolated to the forward direction at  $|t| \rightarrow 0$  ( $t$  is the four-momentum transfer). A measurement of elastic scattering in the very forward direction gives thus information about the total cross section. The differential elastic cross section is related to the strong interaction amplitude by

$$\frac{d\sigma_{el}}{dt} = \pi |f_{el}(\theta)|^2 \quad (3.7)$$

where  $f_{el}(\theta)$  is

$$f_{el}(\theta) = Re[f_{el}(\theta)] + iIm[f_{el}(\theta)] \quad (3.8)$$

Applying the optical theorem yields

$$\sigma_{tot}^2 = \frac{16\pi}{1 + \rho^2} \left( \frac{d\sigma_{el}}{dt} \right)_{t \rightarrow 0} \quad (3.9)$$

where  $\rho$  is the ratio of the real to the imaginary part of the elastic scattering amplitude:

$$\rho = \frac{Re[f_{el}(t=0)]}{Im[f_{el}(t=0)]} \quad (3.10)$$

Eq.(3.9) can be rewritten as:

$$\sigma_{tot}^2 = \frac{16\pi(\hbar c)^2}{1 + \rho^2} \frac{1}{\mathcal{L}} \left( \frac{dN_{el}}{dt} \right)_{t \rightarrow 0} \quad (3.11)$$

where the luminosity value has been isolated. Eq.(3.11) shows that  $\sigma_{tot}$  can be determined by measuring the elastic rate extrapolated at  $t=0$  and, independently, the luminosity.

A second technique permits the measurement of  $\sigma_{tot}$  in a luminosity-independent approach. Reminding that  $\sigma_{tot} = \frac{N_{tot}}{\mathcal{L}}$  and  $\frac{d\sigma_{el}}{dt} = \frac{1}{\mathcal{L}} \frac{dN_{el}}{dt}$ , the total cross section and the luminosity can be expressed in terms of the total interaction rate  $N_{tot}$  and of the elastic event rate  $\frac{dN_{el}}{dt}$  extrapolated to zero momentum transfer:

$$\sigma_{tot} = \frac{16\pi}{1 + \rho^2} \frac{(dN_{el}/dt)_{t=0}}{N_{tot}} \quad (3.12)$$

$$\mathcal{L} = \frac{1 + \rho^2}{16\pi} \frac{N_{tot}^2}{(dN_{el}/dt)_{t \rightarrow 0}} \quad (3.13)$$

In this case both  $\frac{dN_{el}}{dt}$  at  $t=0$  and  $N_{tot}$  have to be determined simultaneously, the sum of elastic and inelastic rate. While the elastic rate can be extracted from the measurement of the elastic cross section, the inelastic one has to be determined separately but *simultaneously*. On the other hand, in this second

approach, the  $\mathcal{L}$  determination is not necessary.

In the present thesis, as well described later, the first approach is used and thus the luminosity determination is necessary. The second approach is instead used by TOTEM.

### 3.3 Measurement of $\sigma_{tot}$ with Elastic Scattering in the Coulomb-Nuclear Interference Region

The general expression of the  $pp$  differential elastic cross section is

$$\frac{d\sigma_{el}}{dt} = \frac{1}{16\pi} |f_N(t) + f_C(t)e^{i\alpha\phi(t)}|^2 \quad (3.14)$$

obtained from the contributing diagrams. In Eq.(3.14),  $f_N$  is the strongly interacting amplitude,  $f_C$  is the Coulomb amplitude and a phase  $\phi$  is induced by long-range Coulomb interactions. The problem is the accurate estimation of the inelastic rate in the very forward direction that can be circumvented by measuring the elastic cross section down to angles small enough for the  $t$ -dependence to become sensitive to the Coulomb amplitude. The individual amplitudes are given by:

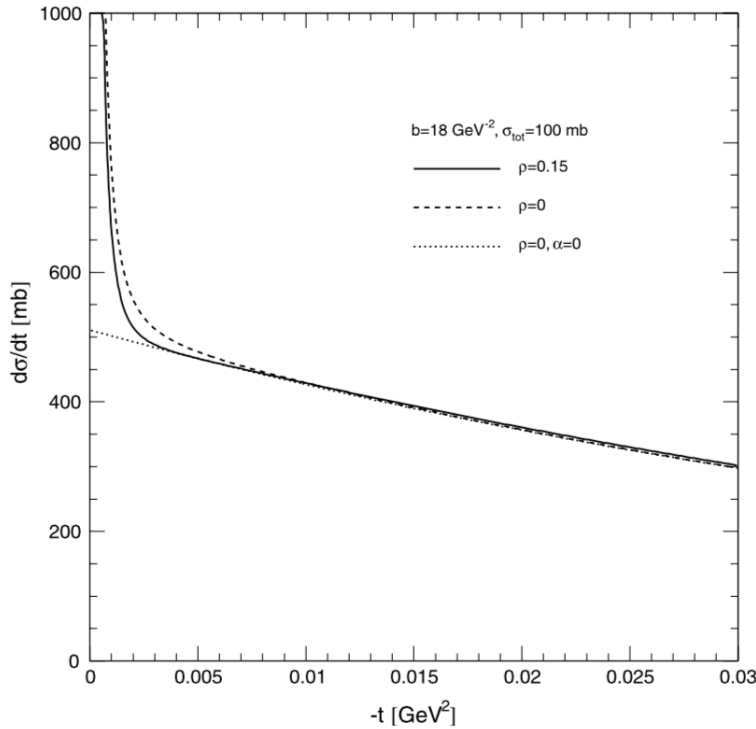
$$f_C(t) = -8\pi\alpha\hbar c \frac{G^2(t)}{t} \quad (3.15)$$

$$f_N(t) = (\rho + i) \frac{\sigma_{tot}}{\hbar c} e^{-B|t|/2} \quad (3.16)$$

where  $G$  is the electric form factor of the proton,  $B$  is the nuclear slope and  $\rho = \frac{Re(f_{el})}{Im(f_{el})}$ . It's important to note that the expression of  $f_N$  is valid in the approximation of small  $|t|$  only. The theoretical form of the  $t$ -dependence of the cross section is obtained from the evaluation of the square of the complex amplitudes:

$$\frac{dN_{el}}{dt} \propto L\pi \left| \frac{-2\alpha}{|t|} + \frac{\sigma_{tot}}{4\pi} (i + \rho) e^{-B|t|/2} \right|^2 \quad (3.17)$$

The Eq.(3.17) contains three terms which correspond to different kinds of interactions. The first term represents the Coulomb interaction, the second one the Coulomb-Nuclear interference and the last one the hadronic interaction. In Eq.(3.17) the only free parameters are  $B$ ,  $\rho$  and  $\sigma_{tot}$ . By fitting the experimental distribution (see Fig.3.3), the previous three parameters can be determined them extracting simultaneously. In order to perform this fit, one needs to reach  $|t| \sim 0.001 \text{ GeV}^2$ . This order of magnitude has been approached in LHC by TOTEM, while ATLAS has reached a minimum  $|t| \sim 0.1 \text{ GeV}^2$ .



**Figure 3.3:** Differential elastic cross section estimation at LHC as a function of transferred momentum. The differential cross section is plotted for  $\rho=0$  (dashed line) and  $\rho=0.15$  (solid line) in order to highlight the interference region, as well as for  $\alpha=0$  (dotted line) to isolate the nuclear contribution.

### 3.4 Beam Optics for $\sigma_{tot}$ Measurement

In order to measure the rate of  $pp$  elastic interactions, it is necessary to reach small enough angles with a dedicated beam optics and with detectors positioned far from the Interaction Point [21]. Only in this way the practically undeflected protons emerging from the elastic interaction and travelling in the beam-pipe can be detected. This implies that the relevant detectors must be integrated in the LHC lattice and that a certain number of quadrupoles separate the IP from the detectors. The assembly of the field gradient of the quadrupoles, which determine the beam optics, has to be optimized for a good measurement of small angle elastic scattering.

There are several criteria that such beam optics has to fulfill:

- The focusing at the IP has to be done in a way that the beam divergence is significantly smaller than the scattering angles to be measured.

The divergence is given by  $\sqrt{\epsilon}/\beta^*$ , where  $\epsilon$  is the beam emittance and  $\beta^*$  is the betatron function at the IP. Knowing that the typical LHC emittance is 2-3  $\mu\text{m}$ ,  $\beta^*$  has to assume values of the order of 100 m in order to achieve divergence of few  $\mu\text{rad}$ .

- The "parallel-to-point" focusing implies that the position trajectory in the detector is independent of the unmeasured vertex position at the IP.
- An effective lever arm,  $L_{eff}^{x,y}$ , between the Interaction Point and the detector can be defined as:

$$\theta_{x,y} = \frac{x,y}{L_{eff}^{x,y}} \quad (3.18)$$

where  $\theta_{x,y}$  is the scattering angle at the IP and  $x, y$  are detectors space coordinate. The lever arm should be large in at least one of the two transverse projection, giving a good separation at the level of the detector and, consequently, a good resolution for different scattering angles at the IP.

A beam optics fulfilling these three requirements in the vertical plane and the first criteria on the horizontal plane was developed both by TOTEM and ATLAS, with small differences implying different approaches in the  $t$  reconstruction method.

### 3.5 $t$ -reconstruction

In order to get an estimation of the  $\sigma_{tot}$ , the measurement of the differential elastic cross section at small values of  $t$ . The key to getting small  $t$  or, equivalently, small scattering angles, is to place the detectors close to the beam and far away from the Interaction Point. In addition, a dedicated optics to get small  $t$ -values is needed.

For small value of the scattering angle and at high energy,

$$-t = (p\theta)^2 \quad (3.19)$$

where  $p$  is the beam momentum and  $\theta$  is the scattering angle at the Interaction Point, which can be written as  $\sqrt{\theta_x^2 + \theta_y^2}$ ,  $\theta_x$  and  $\theta_y$  being, respectively, the scattering angles in the horizontal and vertical planes. In general, the reconstruction of the scattering angle is performed by using the fact that elastic scattering is back-to-back, so the vertex position is identical for the two scattered protons. In this case, the scattering angle at the IP can be

calculated either from a measurement of the position at the Roman Pots or from the measurement of the angle of the tracks at the Roman Pots. The parallel-to-point focusing and the large lever-arm in the vertical plane make the reconstruction method of  $\theta_y$  straight forward. The best resolution and the smallest sensitivity to the optics is achieved by just transforming the position measurement at the Roman Pots to an angle at the IP. This method has a good  $t$ -resolution which is determined in the vertical plane by the beam divergence at the IP and not by the spatial resolution of the detector. The  $t$ -resolution for ATLAS is significantly better using the position measurement but this method is sensitive to the optics. In order to overcome this problem and better understand the sensitivity to the optics, the kinematics of the elastic-scattering data were used.

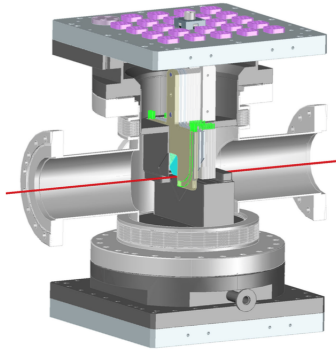
## 3.6 Measurement of $\sigma_{tot}$ at $\sqrt{s} = 7$ TeV in ATLAS in 2011

### 3.6.1 Data Taking

The total cross section has been measured at a centre-of-mass energy of 7 TeV and most of the data reported by ATLAS and TOTEM were taken during a single fill in October 2011, during which 14 bunches circulated in each beam: one high-intensity bunch ( $6 - 7 \times 10^{10}$  protons), 12 low-intensity bunches ( $1-2 \times 10^{10}$  protons) and one non-colliding bunch. Only events from the high-intensity colliding bunches were used and this corresponded to an instantaneous luminosity of  $5 \times 10^{27} \text{ cm}^{-2}\text{s}^{-1}$ . The pile-up conditions were favorable with an average of about 4% inelastic interactions per bunch crossing.

### 3.6.2 The Roman Pots

The *Roman Pots* (RP) [22] are the detectors that are traditionally designated for the measurements of elastic cross section, since the early 70<sup>th</sup>. A Roman Pot is a vessel that contains a detector connected to the accelerator vacuum via bellows (Fig. 3.4). This particular design allows a nearest as possible approach to the beam, without entering the machine. The system was mainly developed by the TOTEM experiment and the ATLAS collaboration followed their guidelines with some changes due to the adaptation to their specific needs. Both TOTEM and ALFA have two stations, located symmetrically on each side of the Interaction Point. Each station consists of two units separated by about 5 meters, each of which consists of two Roman Pots



**Figure 3.4:** Picture of two Roman Pot vessels.

approaching the beam from above and below. Although, the basic methodology is similar for both experiments, the detector technologies used inside the Roman Pots are completely different.

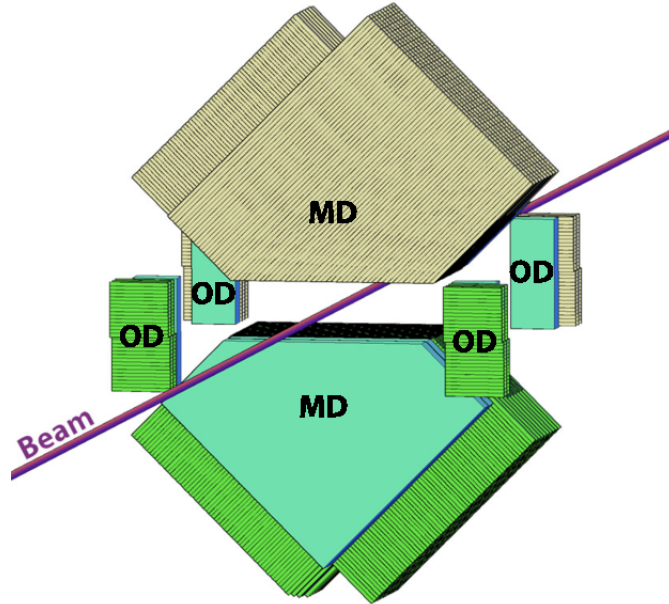
### 3.6.3 The ALFA Detector

The ALFA detector [14] is composed two stations, placed at each side of the central ATLAS detector, one at 238 m and one at 241 m from the interaction point. Each of them carries an upper and a lower RP made of stainless steel with thin windows of 0.2 mm and 0.5 mm thickness at the bottom and front sides to reduce the interactions of traversing protons. In Fig. 3.5, the ALFA tracking system is shown with the *main detectors* (MDs) and the *overlap detectors* (ODs). The formers detect the elastic scattered protons, the latter are dedicated devices for the measurements of the distance between upper and lower MDs.

Each MD consists of two times 10 layers of 64 square scintillating fibres with 0.5 mm side length glued on titanium plates. The fibres are orthogonally disposed at  $\pm 45^\circ$  with respect to the  $y$ -axis and the projection perpendicularly to them define the  $u$  and  $v$  coordinates for the track reconstruction. The theoretical resolution is  $14.4 \mu\text{m}$  but experimental effects such as optical cross-talk, noise, inefficient fibre channels and imperfect staggering (in fact, the fibres are staggered by 1/10 of the their size) lower the actual value. The efficiency of detecting a proton in a single layers is about 93%, with variations of 1% layer to layer.

The ODs consist of three layers of 30 scintillating fibres per layer measuring the vertical coordinate of traversing beam-halo particles or shower fragments. Two independent ODs are attached at each side of both MDs. The signals



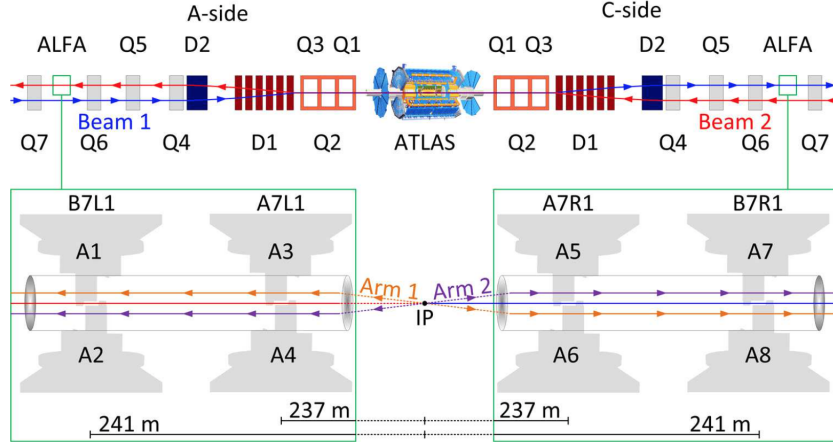


**Figure 3.5:** Schematic view of the ALFA tracking system where the two kinds of detector, main (MD) and overlap (OD) are visible.

from both types of tracking detectors are amplified by 64-channel multi-anode photomultipliers (MAPMTs). Overall, 23 MAPMTs are used to read out each MD and its two respective ODs.

Three mm thick scintillator plates constitute the trigger counters, which complete the tracking detectors. MDs are equipped with two trigger counters and their signals are used in coincidence to reduce noise contributions, while the ODs are covered with just one trigger counters and *all* signals are recorded. Before the data taking, precision motors move the RPs vertically in  $5 \mu\text{m}$  steps towards the beam. The position is measured by inductive displacement sensors (LVDT) whose calibration is performed by a laser survey in the LHC tunnel.

In Fig. (3.6), a sketch of the experimental set-up shows the position of the ALFA Roman Pot stations. The stations A7R1 and B7R1 are positioned in the outgoing beam 1 (C side) at  $z=-273.4$  m and  $z=241.5$  m, respectively, while A7L1 and B7L1 are situated in the outgoing beam 2 (A side). The detectors are numbered from 1 to 8 (A1, A2,...) and they are inserted in increasing order (the even-numbered are in the lower part of the RPs). Two spectrometer arms for elastic scattering event topologies are defined. The arm 1 includes the detectors A1, A3, A6, A8, the arm 2 the detectors A2, A4, A5, A7.



**Figure 3.6:** Schematic sketch of the experimental set-up showing the ALFA Roman Pot station positions.

### 3.6.4 Principles of Measurement

The idea at the basis of the measurement is the detection of the two back-to-back protons emerging at very small angles from the elastic interactions on the two sides of the IP. The data taking was performed with special beam optics characterized by  $\beta^* = 90$  m at the interaction point resulting in a small divergence and providing parallel-to-point focusing on the vertical plane. In parallel-to-point beam optics the betatron oscillation has a phase advance  $\Phi$  of  $90^\circ$  between the interaction point and the RPs, such that all particles scattered at the same angle are focused at the same position at the detector, independent of their production vertex position. This focusing is only achieved in the vertical plane. The beam optics parameters are needed for the reconstruction of the scattering angle  $\theta^*$  at the interaction point starting from the measured angles and position on the detectors. The momentum transfer  $t$ , at high energies, is given by

$$-t = (\theta^* p)^2 \quad (3.20)$$

where  $p$  is the nominal beam momentum of LHC of 3.5 TeV and  $\theta^*$  is measured from the proton trajectories in ALFA. The formalism of transport matrix allows to relate positions and angles of particles of two different points of the magnetic field lattice (Sec.1.1.2). Let's call  $(w(s), \theta_w(s))$ , where  $w=x,y$  are the transverse positions,  $s$  is the longitudinal direction and  $\theta_w$  the angle between  $w$  and  $s$ . We can obtain the trajectory  $(w(s), \theta_w(s))$  via the transport matrix  $\mathbf{M}$  applied to  $(w^*, \theta^*)$ , the coordinates at the interaction

point:

$$\begin{pmatrix} w(s) \\ \theta_w(s) \end{pmatrix} = \mathbf{M} \begin{pmatrix} w^* \\ \theta_w^* \end{pmatrix} = \begin{pmatrix} M_{11} & M_{12} \\ M_{21} & M_{22} \end{pmatrix} \begin{pmatrix} w^* \\ \theta_w^* \end{pmatrix} \quad (3.21)$$

where the elements of the transport matrix, as seen in Sec.(1.1.2), can be calculated from  $\beta$  and its derivative with respect to  $s$  and  $\Phi$ .

In the elastic scattering protons emerge back-to-back and the scattering angles at the A- and C-side of ATLAS are the same in magnitude and opposite in sign. The beam optics is optimized to maximize  $M_{12}$ , in the vertical plane, in order to access the smallest possible scattering angle. The positions measured in the two sides are approximately of the same size but with opposite sign. Various methods can be used to determine  $\theta_w^*$ . All of them are exploited and the variations in the results are used to quote the systematic uncertainties in  $t$  reconstruction.

- Using the so-called "subtraction method", the scattering angle is calculated according to:

$$\theta_w^* = \frac{w_A - w_C}{M_{12,A} + M_{12,C}} \quad (3.22)$$

This is the baseline method for  $\theta_y^*$  determination due to the parallel-to-point focusing in the  $y$ -direction.

- An alternative method for the reconstruction of the horizontal scattering angle is to use the "local angle"  $\theta_w$  measured by two detectors on the same side

$$\theta_w^* = \frac{\theta_{w,A} - \theta_{w,C}}{M_{22,A} - M_{22,C}} \quad (3.23)$$

- Another method performs a "local subtraction" of measurements at the inner station at 237 m and the outer station at 241 m, separately at the A- and C-side, before combining the two sides, (S=A,C):

$$\theta_{w,S}^* = \frac{M_{11,S}^{241} \times w_{237,S} - M_{11,S}^{237} \times w_{241,S}}{M_{11,S}^{241} \times M_{12,S}^{241}} \quad (3.24)$$

- Finally, the measured positions and the local angle are used to reconstruct the scattering angle by the inversion of the transport matrix:

$$\begin{pmatrix} w^* \\ \theta_w^* \end{pmatrix} = \mathbf{M}^{-1} \begin{pmatrix} w \\ \theta_w \end{pmatrix} \quad (3.25)$$

From the second row of the inverted matrix, the scattering angle is determined

$$\theta_w^* = M_{12}^{-1} \times w + M_{22}^{-1} \times \theta_w \quad (3.26)$$

All methods, which use the local angle, suffer from a poor resolution due to the moderate angular resolution of about  $10 \mu\text{rad}$ .

For all methods  $t$  is calculated from the scattering angles as:

$$-t = ((\theta_x^*)^2 + (\theta_y^*)^2)p^2 \quad (3.27)$$

where  $\theta_y^*$  is always reconstructed with the subtraction method because of the parallel-to-point focusing in the vertical plane, while the various methods, explained above, are used to reconstruct  $\theta_x^*$ .

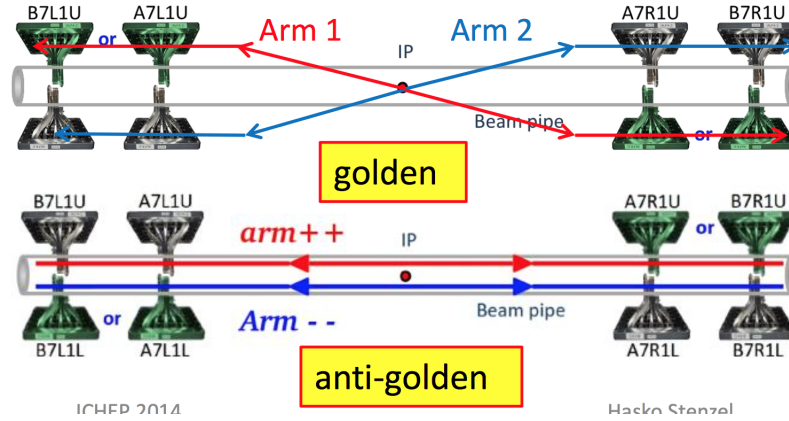
### 3.6.5 Data Acquisition and Analysis

Two main triggers were used to detect the elastic-scattering events. They required a coincidence of the main detector trigger scintillators between either of the two upper (lower) detectors on side A and either of the two lower (upper) detectors on side C in order to maximize the back-to-back configuration expected from elastically scattered protons.

The alignment of the Roman Pots is a fundamental issue in order to achieve the desired precision in the measurement in both vertical and horizontal dimensions. A beam-based alignment procedure is necessary in order to determine the position of the RPs with respect to the proton beams. The beam-based alignment procedure was performed in a dedicated fill with identical beam settings, before the data-taking run. From the positions of the upper and the lower RP windows with respect to the beam edges, the centre of the beam as well as the distance between the upper and the lower pots are computed. The distance between the upper and the lower pots was measured to be 8.7 mm for the station nearest to the interaction point and 7.8 mm for the station far away.

The reconstruction of elastic-scattering events is based on local tracks of the proton trajectory in the RP stations. A track is considered a well-reconstructed elastic-scattering event if it consists of local tracks in all four RP stations. In each MD, 20 layers of scintillating fibres are arranged perpendicular to the beam direction. The hit pattern, which allows the reconstruction of the local tracks, is usually a straight trajectory, almost parallel to the beam direction. Typically, in elastic scattering events, the average multiplicity per detector is about 23 hits, where 18-19 are attributed to the proton trajectory and the remaining 4-5 hits are due to beam-related background, cross-talk and electronic noise.

In order to reject events with hadronic showers and layers with high noise level, fibre layers with more than ten hits are not used in track reconstruction. At least three layers out of the possible ten are required to have a



**Figure 3.7:** Comparison of *golden* (top) and *anti-golden* (bottom) topology for reconstruction of elastic scattered candidates.

hit-multiplicity between one and three. In elastic scattering events, multiple tracks, originated from shower events associated, may happen mostly in a single side of the spectrometer arms and can be removed by a track-matching with the other side. In case of elastic scattering pile-up (multiple tracks are reconstructed in both sides of the detector), only the candidate with the best track-matching is accepted.

The track reconstruction in the ODs is based on the same method as described here for the MDs, but with a lower precision, because only three fibre layers are available.

The triggered events having a reconstructed track in all the four detectors of the arm which fired the trigger are the candidates of elastic-scattering events. Moreover these events are required to fulfill the so-called *golden* topology with two track in opposite vertical detector positions on the left and right side, see Fig.(3.7). The rate of elastic-scattering events is corrected for losses due to partly reconstructed events. This correction is defined as the event reconstruction efficiency and it is evaluated on the data with a tag-and-probe methodology.

### 3.6.6 Luminosity Determination with ALFA

The ALFA measurement is based on the optical-theorem approach which requires the simultaneous measurement of the luminosity and of the elastic event rate. In normal running condition at high luminosity ( $\mathcal{L} > 10^{33} \text{ cm}^{-2}\text{s}^{-1}$ ), ATLAS exploits several detectors and algorithms to determine the luminosity and evaluate the relate systematic uncertainties, see Sec.2.2.

Algorithm	$\mathcal{L}$ ( $\mu\text{b}^{-1}$ )
BCMV_EventOR	$79.68 \pm 0.13$
BCMH_EventOR	$79.11 \pm 0.13$
LUCID_EventOR	$78.63 \pm 0.04$
LUCID_EventAND	78.48
LUCID_HitOR	$79.72 \pm 0.03$
VTZ5	$79.72 \pm 0.03$

**Table 3.1:** Luminosity results for the different algorithms in the 2011 measurement. The uncertainties listed are statistical only.

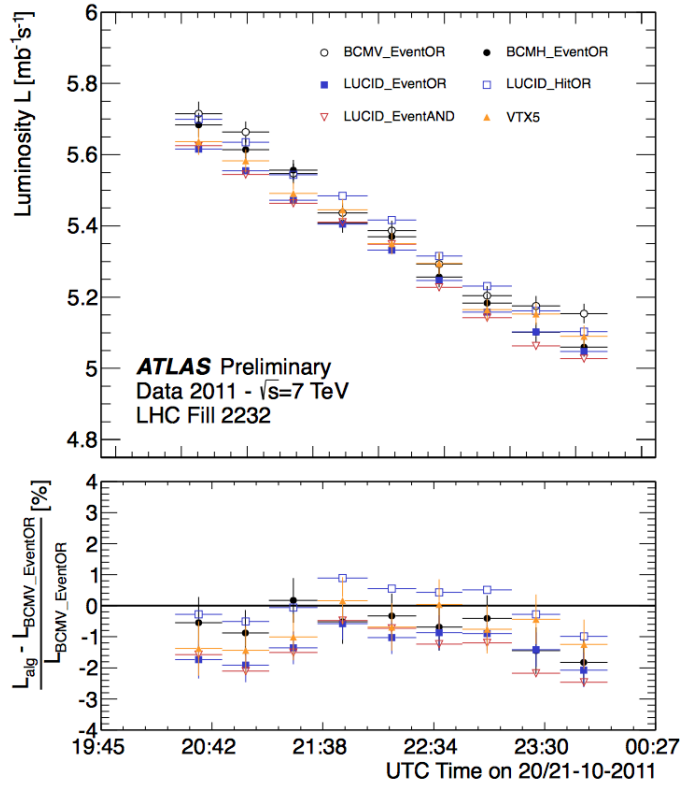
The conditions in the low-luminosity run analysed here are very different from those in high-luminosity runs. The instantaneous luminosity is about of six orders of magnitude lower ( $\mathcal{L} \sim 5 \times 10^{27} \text{ cm}^{-2} \text{ s}^{-1}$ ) which makes the calorimeter methods unusable due to the lack of sensitivity. Another difference with respect to the normal high-luminosity conditions is the background composition. The beam-gas contribution, normally negligible, can, in fact, become competitive with the collision rate in the low-luminosity regime. On the other hand, the "afterglow" background is less important due to the presence of only a few colliding bunches.

In 2011 data taking, BCM was used as the baseline detector for the luminosity determination. For high- $\beta^*$  runs, an inclusive-OR algorithm was used to measure the luminosity, LUCID\_EventOR, but also a coincidence (AND) and hit-counting algorithms (HitOR) were used. A third method for measuring the per-bunch luminosity was provided by the Inner Detector, which counts the number of primary vertices per event, a quantity proportional to the luminosity. The vertex selection criteria required a minimum number of tracks with  $p_T > 400$  MeV forming a common vertex, with additional quality requirements.

The absolute integrated luminosity during ALFA runs should be regarded as a combined measurement of all the detectors because with this redundancy, it's possible to solve inconsistency and to assess correctly the systematic uncertainties. In Tab.(3.1), the luminosity results for the various algorithms are reported. In Fig.(3.8), the values of luminosity are shown as a function of time during the run (top) and percentual deviations with respect to the reference algorithm (bottom). The total integrated luminosity measured in 2011 is:

$$\mathcal{L}_{int} = 78.72 \pm 0.13(stat) \pm 1.93(sys)\mu\text{b}^{-1} \quad (3.28)$$

The systematic uncertainties are listed in Tab.(3.2) with a total uncertainty of 2.45%.



**Figure 3.8:** Values of luminosity determined using various algorithms as a function of time during the run (top) and as percentual deviations with respect to the reference algorithm (bottom).

Source	value(%)
Calibration	1.53
BCM drift	0.25
Consistency	1.6
Background	0.2
Time Stability	1.0
Total	2.45

**Table 3.2:** List of the main sources of systematic uncertainties affecting the luminosity determination in the 2011 high  $\beta^*$  runs. The total uncertainty is 2.45%.

### 3.6.7 ALFA Total Cross Section Results

The results of the ATLAS measurement of  $\sigma_{tot}$  and  $\sigma_{el}$  between  $0.01 \text{ GeV} < |t|_{min} < 0.1 \text{ GeV}$  are

$$\sigma_{el} = 24.00 \pm 0.19(stat) \pm 0.26(sys)mb \quad (3.29)$$

and

$$\sigma_{tot} = 95.35 \pm 0.36(stat) \pm 1.25(sys) \pm 0.37(extrapolation)mb \quad (3.30)$$

## 3.7 Measurement of $\sigma_{tot}$ at $\sqrt{s} = 7$ TeV with TOTEM

The TOTEM experiment was designed to measure the total proton-proton cross section with a separate measurement of the elastic and inelastic cross section [23].

TOTEM has three different Roman Pot stations, two approaching the beam vertically and the third horizontally inside the LHC ring. With respect to ALFA, TOTEM uses silicon sensors. Two sets of RP stations, placed at  $\pm 147$  m and  $\pm 220$  m from the Interaction Point, and their detectors allow a study of the elastic scattering cross section down to a four-momentum transfer square of  $|t| \simeq 10^{-3} \text{ GeV}^{-2}$ .

To measure the inelastic cross section by identifying the inelastic beam-beam events, two telescopes (T1 and T2) detect charged particles produced in a certain range of pseudorapidity. Each telescope is made of two arms, symmetrically placed at about 9 and 13.5 m from the IP respectively [24].

The three TOTEM subsystems have each their own particular electronic system, but nevertheless follow a common architecture.

### 3.7.1 TOTEM Results

TOTEM has reported four different measurements of  $\sigma_{tot}$  at 7 TeV. The first measurement is based upon data taken in the first LHC run with a  $\beta^* = 90$  m optics in June 2011 with an integrated luminosity of  $1.7 \mu\text{b}^{-1}$ . The other two measurements are based upon two different methods to extract the total cross sections using the same data set of  $84 \mu\text{b}^{-1}$ .

The first measurement used the Optical Theorem and an independent measurement of the luminosity as for ALFA. The detectors were not as close to the beam as they were in the later measurements and 30% of hadronic elastic



events were not detected. A  $|t|_{min}$  of 0.02 GeV<sup>2</sup> was achieved. The value of  $\sigma_{tot}$  reported is

$$\sigma_{tot} = 98.3 \pm 0.2_{stat} \pm 2.8_{syst} mb \quad (3.31)$$

The systematic uncertainty is dominated by the extrapolation to  $t=0$  and the luminosity uncertainty. The luminosity was taken from a measurement of the CMS experiment with an uncertainty of 4%, twice the value provided by ALFA.

The settings and the positioning of the RPs allowed to reach  $|t|_{min}$  values in the range  $4.6 \times 10^{-3} \div 7.3 \times 10^{-3}$  GeV<sup>2</sup>. The three different data sets were analyzed separately to better understand the systematic uncertainties. Considering the excellent agreement found between the three samples, they were merged to extract final result. The differential elastic cross section was thus fitted in the  $t$ -range  $5 \times 10^{-3}$  GeV  $< |t|_{min} < 0.2$  GeV, obtaining for the total elastic cross section

$$\sigma_{el} = 25.40 \pm 0.03(stat) \pm 1.1(sys) mb \quad (3.32)$$

and for the total cross section

$$\sigma_{tot} = 98.6 \pm 2.2 mb \quad (3.33)$$

In case of  $\sigma_{tot}$ , the uncertainty is only systematic because, merging all the data samples, (nearly one million elastic events), the statistical uncertainty is negligible. The luminosity uncertainty is the main source of systematic and it is about 4%.

Thanks to the very low  $|t|$  value reached, the sample was also analysed using the luminosity-independent method (see Sec.3.2).

The result for the total cross section is

$$\sigma_{tot} = 98.0 \pm 2.5 mb \quad (3.34)$$

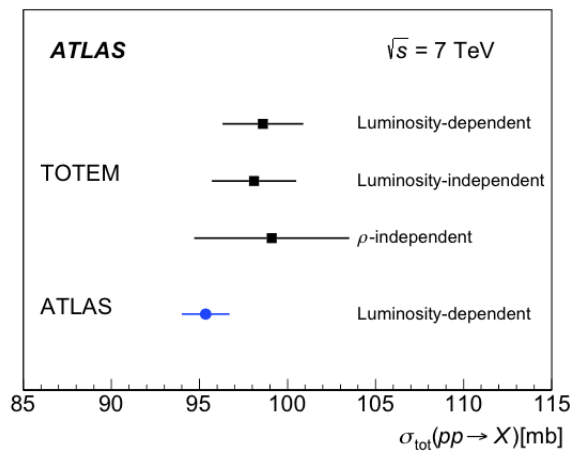
The value is consistent with the one measured with the luminosity-dependent method and the uncertainty on the luminosity determination is substituted by the one of the inelastic rate.

TOTEM used a third method for the calculation of  $\sigma_{tot}$ . The first two approaches used the Optical Theorem and so they depend on the value of  $\rho$ . Alternatively,  $\sigma_{tot}$  can be simply calculated as the sum of  $\sigma_{inel}$  and  $\sigma_{el}$ , where  $\sigma_{el}$  is estimated from the measured differential elastic cross section. Using the same data sample, TOTEM obtains:

$$\sigma_{tot} = 99.1 \pm 4.3 mb \quad (3.35)$$

## 3.8 Comparison of ATLAS and TOTEM Measurements

### 3.8.1 Systematic Uncertainties



**Figure 3.9:** Comparison of the three TOTEM results and ALFA (ATLAS detector performing this measurement) result in the determination of  $\sigma_{tot}$  at  $\sqrt{s}=7$  TeV (2011 data).

- luminosity determination at ATLAS is based upon  $vdM$  scans (See Sec.2.4) and the measurement by BCM, LUCID and Inner Detector. There are three factors which contribute to the overall uncertainty:
  - the uncertainty of the absolute scale as determined by the van der Meer scans.
  - the transfer of the absolute scale from the conditions of the calibration to the very low luminosity conditions of data taking.
  - the contribution of the uncertainties from the subtraction of beam-associated background in the luminosity monitor that has been used.

On the other hand TOTEM determined  $\sigma_{tot}$  both with luminosity-dependent and independent methods. When using the former approach, it is thus necessary to include the uncertainty on the luminosity determination from the CMS experiment (note that the ATLAS systematic uncertainty due to the luminosity determination is about half the corresponding value from CMS calculation).

- $t$  extrapolation. Both experiments extrapolate to  $t=0$  assuming an exponential form of the hadronic amplitude. Differently from ATLAS, TOTEM quotes a negligible systematic uncertainty due to this extrapolation. Moreover ATLAS included the Coulomb and Coulomb-Nuclear Interference term in the fit to the elastic cross section, while TOTEM didn't include it. However, this should not imply substantial differences in the lower limit of the measured  $t$ -range thanks to the relatively large values of  $t$  reached by the 2 experiments compared to the Nuclear-Coulomb interference region.
- Beam Energy. The uncertainty of the value of the beam energy influences the extracted value of the total cross section indirectly through the calculation of  $t$  in the assumed limit:  $-t=(p\theta)^2$ . While ATLAS includes this contribution in the systematic uncertainty, TOTEM does not mention it.
- Results comparison. ATLAS and TOTEM measurements show a satisfactory consistency of  $1.3 \sigma$ , assuming that the uncertainties are uncorrelated, see Fig.(3.9).



## Chapter 4

# Luminosity Determination for the Total Cross Section Measurement at $\sqrt{s} = 8$ TeV

In 2012 the LHC center of mass energy was raised for 7 to 8 TeV. A new measurement of the total cross section was therefore performed in order to add further experimental information to the energy dependence of  $\sigma_{tot}$ . Two different data samples have been acquired, with different experimental conditions. The first run (number 206881) has been performed in July 2012 with  $\beta^*=90$  m (similar to 2011 case), the second (number 213268) in October 2012 with  $\beta^* = 1000$  m. The main characteristics of LHC configuration have been reported in Tab.(1.1). In this chapter, the procedure for the determination of the integrated luminosity is described. This evaluation is necessary for the measurement of the total cross section  $\sigma_{tot}$ , performed by the ALFA detector, as explained in Chapter 3.

The two acquired runs are both characterized by a very low value of  $\mu$ , the average number of interactions per bunch crossing, with respect to the normal runs (up to 3 ÷ 4 orders of magnitude difference), with substantial implications on the problematics of the luminosity measurement.

### 4.1 The Data Sample

The two data samples have been taken during the so called ALFA runs (or high- $\beta^*$  runs), with a dedicated machine optics set up, necessary for the measurement of the  $pp$  elastic scattering in the forward direction.

### 4.1.1 Run 206881 at $\beta^* = 90$ m

Run 206881 was acquired between July 12 and July 13 2012 at center-of-mass energy of  $\sqrt{s}=8$  TeV with  $\beta^*=90$  m. Both beams had an average number of protons of about  $2.5 \times 10^{11}$ . Overall, 647 Luminosity Blocks were acquired with an average duration of 60 seconds each, but only the first part of the run (before LB=335) was dedicated to the elastic scattering measurement. The LBs from 335 on are therefore discarded in this analysis.

The number of colliding bunches was 108 but only 3 of them can be used in this analysis since the ALFA detector was triggered on these three bunches only. The average number of interactions per bunch-crossing was in the range  $0.08 \lesssim \mu \lesssim 0.1$ .

### 4.1.2 Run 213268 at $\beta^* = 1000$ m

Run 213268 was taken between October 24 and October 25 2012 at a center-of-mass energy of  $\sqrt{s}=8$  TeV with  $\beta^*=1000$  m. Both beam 1 and 2 had a typical intensity of  $\sim 2 \times 10^{11}$  protons. Three bunches were colliding during this run, but the first (called *pilot*) is not used in this analysis, due to particularly low number of protons, and consequently low luminosity, with respect to the other two. The average number of interactions per bunch-crossing was in the range  $0.001 \lesssim \mu \lesssim 0.005$ .

## 4.2 Analysis Procedure

As for the standard high luminosity runs, ALFA strategy consists in using as many detectors and algorithms as possible in order to better cross-check the results and assess the systematic uncertainties. In the special case of high- $\beta^*$  runs, where the instantaneous luminosity is very low, only LUCID and BCM are sensitive enough to measure the luminosity. Tile Calorimeter can be used as cross-check for run 20688 only (with 108 bunches) but, as it only provides BCID-averaged luminosity, it is not possible to restrict the measurement to the 3 triggered BCIDs. Finally the data to be used for the vertex and track-counting analysis are still not fully reprocessed so that this measurement is also not possible.

### 4.2.1 Luminosity Algorithms

The used algorithms are Event-counting type (see Sec.2.3.1), namely: BCMHOR, BCMVOR (double-side inclusive OR for the horizontal and vertical parts of BCM), BCMHORC and BCMVORC (single-side inclusive OR), LCDOR

(LUCID double-side inclusive OR), and LCDORA and LCDORC (single-side OR for LUCID). All other algorithms, such as the coincidence ones (AND) were not calibrated in the  $vdM$  scans, so they are not used. BCMHOR has been used as reference algorithm for consistency checks with the standard physics runs at high luminosity.

As mentioned above, in principle TileCal can be used for consistency checks for run 206881, but without the possibility to select the 3 triggered BCIDs. For run 213268, due to the even lower  $\mu$ -values and number of colliding bunches, TileCal is not usable at all, due to the lack of sensitivity. The same considerations are applied also for the forward calorimeter FCAL.

### 4.2.2 Statistical Errors

As described in Sec.(1.5.1), the average number of interactions per bunch crossing ( $\mu$ ) in a Luminosity Block can be calculated as

$$\mu = -\frac{1}{\epsilon} \ln \left( 1 - \frac{N_{ev}}{N_{BC}} \right) \quad (4.1)$$

where  $N_{BC}$  crossings have happened and  $N_{ev}$  have been detected by the luminosity detector, under the assumption that the number of interactions per BC is distributed following the Poisson statistics. Defining

$$P(N_{ev}) = \frac{N_{ev}}{N_{BC}} \quad (4.2)$$

and assuming that  $N_{ev}$  follows a Binomial distribution, then the variance can be expressed as

$$Var[N_{ev}] = N_{BC} P(N_{ev})(1 - P(N_{ev})) = N_{BC} \frac{N_{ev}}{N_{BC}} \left( 1 - \frac{N_{ev}}{N_{BC}} \right) \quad (4.3)$$

and the error on  $N_{ev}$  is:

$$\delta N_{ev} = \sqrt{N_{ev} \cdot \left( 1 - \frac{N_{ev}}{N_{orb}} \right)} \quad (4.4)$$

The statistical error associated to  $\mu$  can be therefore evaluated using the following formula:

$$\delta \mu = \frac{\partial \mu}{\partial N_{ev}} \delta N_{ev} = \frac{1}{\epsilon} \frac{1}{\sqrt{N_{orb}}} \sqrt{\frac{\frac{N_{ev}}{N_{orb}}}{1 - \frac{N_{ev}}{N_{orb}}}} \quad (4.5)$$

	$\sigma_{vis}(mb)$	$\sigma_{vis}(mb)$
Algorithm	July 2012	November 2012
BCMHOR	5.1334	5.0799
BCMHORC	2.6589	2.6371
BMCVOR	5.1549	5.0458
BMCVORC	2.6631	2.5848
LCDOR	36.4170	35.4962
LCDORA	23.8922	23.1923
LCDORC	21.1661	20.5268

**Table 4.1:** Values of  $\sigma_{vis}$  measured in July and November 2012 calibration for LUCID and BCM algorithms.

### 4.2.3 Calibration

The van der Meer calibration for 2012 has been described in Sec.(2.4). Having various  $vdM$  calibrations available, each of the two ALFA runs was analysed using the closest calibration in time, namely: for run 206881 the July  $vdM$  calibration, while for run 213268 the one performed in November. For run 206881, the calibration has been performed few days apart from the data taking: this reduces systematic effects of long term stability of the luminometers. A month separates run 213268 from the corresponding  $vdM$  scan calibration, so that effects due to long term stability cannot be ignored. In Tab.(4.1) the values of calibration constants  $\sigma_{vis}$  for the used algorithms are reported for both the July and November  $vdM$  scans.

## 4.3 Background Definition and Evaluation

The background subtraction is one of the most delicate issues of the luminosity measurement in ALFA runs. In fact, due to the very low value of the luminosity, the contribution of the background (or at least of some of background components) can become competitive and therefore a detailed understanding and modelling of the various background contributions is needed. In normal physics runs at high-luminosity, the background evaluation, although necessary, is less crucial.

Two main background components are usually considered:

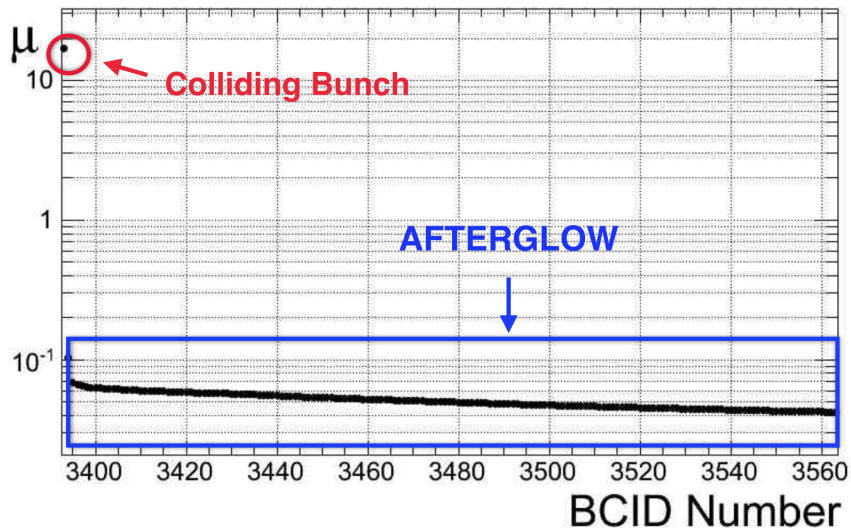
- *afterglow* background;
- *beam-gas* (also called single-beam) background.



In the following sub-sections, these two contributions are discussed and the approach for their evaluation and subtraction are explained.

### 4.3.1 Afterglow Background

The afterglow background is caused by the emission of photons from nuclear de-excitation, induced by the hadronic cascades originated by  $pp$  collision products. The typical shape of the afterglow background induced by a single colliding bunch can be seen in Fig.(4.1) and consists of an exponential tail following the colliding bunch with a decay time of the order of  $\mu\text{s}$ . In normal



**Figure 4.1:** Typical shape of afterglow background induced by a single colliding bunch, an exponential tail with decay time of few  $\mu\text{s}$ .

running conditions, with a large number of colliding bunches at high  $\mu$ , the afterglow contribution is expected to be high because each colliding bunch produces afterglow and therefore influences the following ones.

In ALFA runs,  $\mu$  is low and few bunches with a large time separation are colliding, so this background source is expected to be reduced.

As the afterglow background results in an overestimation of the signal in the BCID following a colliding one, however its level must be carefully evaluated. In the following actions, modelling and subtraction procedure are described.

### 4.3.2 Afterglow Modelling

In this sub-section, the modelling of signal and afterglow background are described both separately and in superimposed conditions. The aim is to come up with formulas which allow the estimation, from the measured probabilities of the various algorithms (which are by definition composed by both signal and background), the corresponding background-subtracted probabilities (and therefore the background subtracted  $\mu$ ). In Fig.(4.2), the modelling of the SIGNAL contribution and the corresponding probabilities of the following event-counting algorithms are shown:

- $P_0$ : zero-counting probability (SIGNAL ONLY)
- $P_A, P_C$ : exclusive single-side probabilities (SIGNAL ONLY)
- $P_{AND}$ : coincidence probability (SIGNAL ONLY)

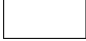
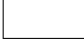

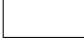




from these formulas the inclusive (SIGNAL ONLY) probabilities can be calculated:

- $P_{OR} = 1 - P_0$  (SIGNAL ONLY)
- $P_{ORA} = P_A + P_{AND}$  (SIGNAL ONLY)
- $P_{ORC} = P_C + P_{AND}$  (SIGNAL ONLY)

SIGNAL MODEL		(A)
A-Side	C-Side	
<input type="checkbox"/>	<input type="checkbox"/>	$P_0 = e^{-\epsilon_{OR}\mu}$
<input checked="" type="checkbox"/>	<input type="checkbox"/>	$P_A = e^{-\epsilon_C\mu} - e^{-\epsilon_{OR}\mu}$
<input type="checkbox"/>	<input checked="" type="checkbox"/>	$P_C = e^{-\epsilon_A\mu} - e^{-\epsilon_{OR}\mu}$
<input checked="" type="checkbox"/>	<input checked="" type="checkbox"/>	$P_{AND} = 1 - e^{-\epsilon_A\mu} - e^{-\epsilon_C\mu} + e^{-\epsilon_{OR}\mu}$

**Figure 4.2:** (A): Signal modelling for zero-counting, exclusive single-side ( $P_A, P_C$ ) and coincidence ( $P_{AND}$ ) algorithms.

A table (4.3) similar to the one obtained for signal can be built for the BACKGROUND contribution and for the corresponding probabilities using the exclusive single-side probabilities (BACKGROUND ONLY),  $P_{bA}$  and  $P_{bC}$ , the suffix "b" reflects the BACKGROUND ONLY contribution. Having the separate contributions of signal ( $P_{OR}, P_{ORA}, P_{ORC}, P_A, P_C, P_{AND}$ ) and background ( $P_{bA}, P_{bC}$ ) probabilities, the different cases, corresponding to the

BACKGROUND MODEL		(B)
A-Side	C-Side	
		$(1 - P_{bA})(1 - P_{bC})$
		$P_{bA}(1 - P_{bC})$
		$P_{bC}(1 - P_{bA})$
		$P_{bA}P_{bC}$

**Figure 4.3:** (B): Background-only modelling based on the exclusive single-side background probabilities  $P_{bA}$  and  $P_{bC}$ .

different algorithms, can be modelled by combining tables in Fig.(4.2) and in Fig.(4.3) into a third table containing all possible combinations of signal and background. Table in Fig.(4.4) show for different algorithms all the probabilities obtained combining signal and background separated ones. Calling  $P_X^{meas}$  the measured probabilities for algorithm "X", i.e. the "signal+background" probability (measured by the detector),  $P_{bX}$  the "background-only" contribution to the measured probability (as for table in Fig.4.3) and  $P_X$  the corresponding "signal-only" probability (i.e. the background subtracted one, goal of all this modelling description, as from Fig.4.2) using table in Fig.4.4 derive from table C the useful equations providing the background-subtracted probabilities from the measured and the pure-background ones can be derived:

- OR Algorithm.

$$P_{OR} = \frac{P_{OR}^{meas} - (P_{bA} + P_{bC} - P_{bA}P_{bC})}{(1 - P_{bA} - P_{bC} + P_{bA}P_{bC})} \quad (4.6)$$

- A(C)\_Exclusive Algorithm.

$$P_{A(C)} = \frac{P_{A(C)}^{meas} - (1 - P_{OR})(P_{bA(C)} - P_{bA}P_{bC})}{1 - P_{bC(A)}} \quad (4.7)$$

- And Algorithm.

$$P_{AND} = \frac{P_{AND}^{meas} - (P_A P_{bC} + P_C P_{bA} + P_{bA} P_{bC} - P_A P_{bA} P_{bC} - P_C P_{bA} P_{bC})}{1 - P_{bA} P_{bC}} \quad (4.8)$$

The only open point is how to define the "background-only" probabilities ( $P_{bX}$ ). The best approximation is to use as the "background-only" probability estimation, the probability measured in the "previous-to-colliding" bunch.

**Combining Signal and Background**

Zero-Counts			C-Counts		
A-Side	C-Side		A-Side	C-Side	(C)
<input type="checkbox"/>	<input type="checkbox"/>	$P_0(1 - P_{bA})(1 - P_{bC})$	<input type="checkbox"/>	<input checked="" type="checkbox"/>	$P_C(1 - P_{bA})(1 - P_{bC})$
<input checked="" type="checkbox"/>	<input type="checkbox"/>	$P_0P_{bA}(1 - P_{bC})$	<input checked="" type="checkbox"/>	<input checked="" type="checkbox"/>	$P_CP_{bA}(1 - P_{bC})$
<input type="checkbox"/>	<input checked="" type="checkbox"/>	$P_0(1 - P_{bA})P_{bC}$	<input type="checkbox"/>	<input checked="" type="checkbox"/>	$P_C(1 - P_{bA})P_{bC}$
<input checked="" type="checkbox"/>	<input checked="" type="checkbox"/>	$P_0P_{bA}P_{bC}$	<input checked="" type="checkbox"/>	<input checked="" type="checkbox"/>	$P_CP_{bA}P_{bC}$
A-Counts			AND-Counts		
A-Side	C-Side		A-Side	C-Side	
<input checked="" type="checkbox"/>	<input type="checkbox"/>	$P_A(1 - P_{bA})(1 - P_{bC})$	<input checked="" type="checkbox"/>	<input checked="" type="checkbox"/>	$P_{AND}(1 - P_{bA})(1 - P_{bC})$
<input checked="" type="checkbox"/>	<input checked="" type="checkbox"/>	$P_AP_{bA}(1 - P_{bC})$	<input checked="" type="checkbox"/>	<input checked="" type="checkbox"/>	$P_{AND}P_{bA}(1 - P_{bC})$
<input checked="" type="checkbox"/>	<input type="checkbox"/>	$P_A(1 - P_{bA})P_{bC}$	<input checked="" type="checkbox"/>	<input checked="" type="checkbox"/>	$P_{AND}(1 - P_{bA})P_{bC}$
<input checked="" type="checkbox"/>	<input checked="" type="checkbox"/>	$P_AP_{bA}P_{bC}$	<input checked="" type="checkbox"/>	<input checked="" type="checkbox"/>	$P_{AND}P_{bA}P_{bC}$

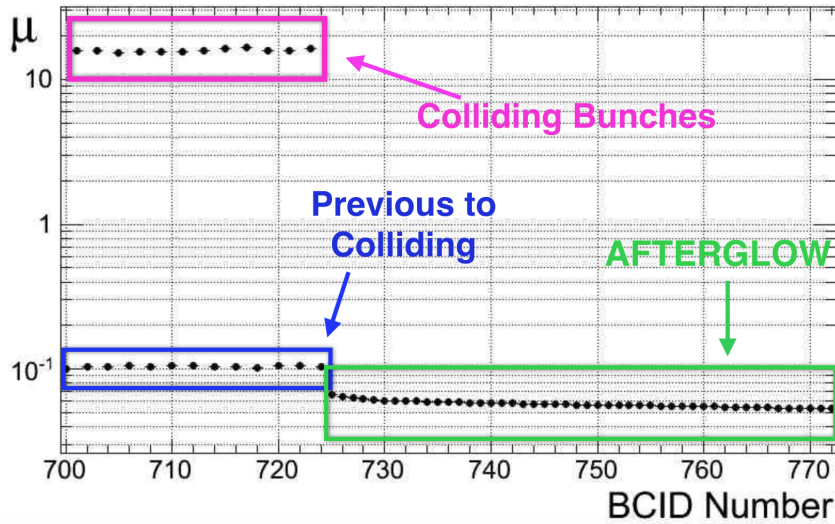
**Figure 4.4:** (C): Table reporting the modelling of signal+background contributions to the different algorithms.

In the 2012 LHC bunch configuration, spacing between colliding bunches was not 25 ns as in the original design, but 50 ns, so that the bunch preceding any colliding one was empty. Therefore whatever activity a detector measures in such empty bunch must be due to afterglow background produced by all preceding colliding bunches. In Fig.4.5 a typical BCID-distribution of the measured activity in LUCID is shown, for a high-luminosity run with many colliding bunches, where the colliding bunches are drawn together with the "previous-to-colliding" ones, used to estimate the background-only probabilities.

### 4.3.3 Afterglow Subtraction Results

In this section the verification of the quality of the afterglow subtraction evaluation using Eqs. 4.6, 4.7, 4.8 and the assumption that the "previous-to-colliding" bunch is a good estimate of the afterglow are presented. If the above assumptions and afterglow modelling are correct, after the afterglow background correction, a probability compatible with zero will remain.

In Figs. 4.6 and 4.7, in the so-called "forbidden-gap", that is the range of BCIDs never filled, for run 206881, the measured (blu) and afterglow subtracted (green) probabilities are shown for both BCM and LUCID algorithms. The afterglow-subtracted probabilities, as a function of the BCID number, are flat and compatible with zero as a function of the BCID number, showing that the method is reliable.



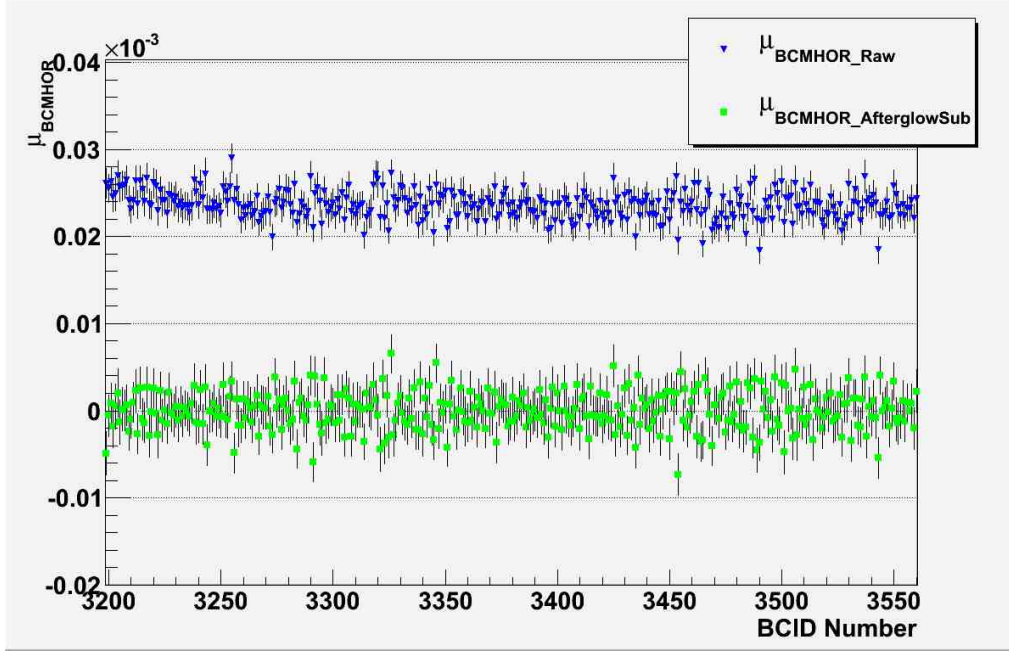
**Figure 4.5:** A typical BCID-distribution of the measured activity in LUCID, for a high-luminosity run, where the colliding bunches are visible together with the "previous-to-colliding" ones.

In Figs.4.8 and 4.9, the ratio between the afterglow-subtracted and the measured  $\mu$  is shown for BCMHOR and LCDOR as a function of  $\mu$  for run 206881, showing an afterglow level of about 0.05% for BCM 0.1% for LUCID, with no relevant dependence on  $\mu$ . As it regards run 213268, the same is shown in Fig.(4.12) (blu) for BCMHOR (Left) and LCDOR (Right). The average values of afterglow background for this run is 1% for BCMHOR and 2% for LCDOR.

#### 4.3.4 Beam Gas (Single-Beam) Background

The second source of background is the so-called beam-gas background, produced by the interactions of the beam protons with residual gas molecules in the beam-pipe and by halo-particles in time with the beam. As this is related to the presence of protons in one beam (no matter whether the other beam is also filled, i.e. no matter if there are collisions), it is often called single-beam background.

The beam-gas is the most important source of the background in the high- $\beta^*$  runs at very low  $\mu$ , which is not the case of the standard high- $\mu$  runs. In order to evaluate this background, the unpaired bunches are used, where, by definition, only one beam is filled. In general there are several unpaired bunches in each beam. By measuring the average probability, measured by a cer-



**Figure 4.6:** Measured (blue triangles) and afterglow-subtracted (green squares)  $\mu$  for BCMHOR in the forbidden gap.

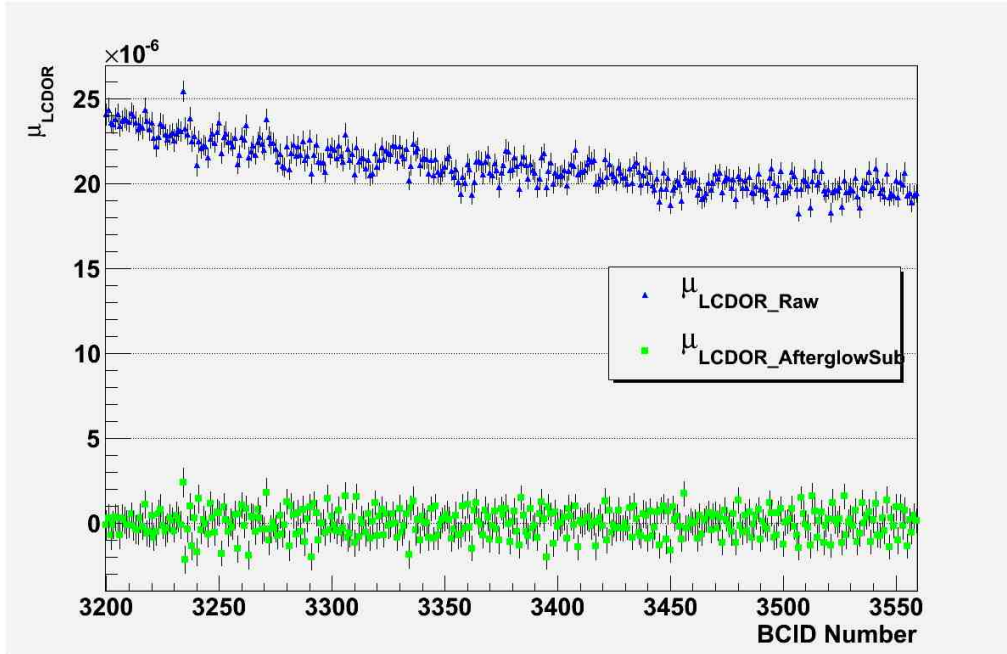
tain algorithm, in such unpaired bunches and rescaling it by the ratio of the proton currents in the colliding bunch under investigation and the unpaired bunches used for beam-gas monitoring, the expected beam-gas background contribution is obtained:

$$P_{coll}^{beam\ gas} = \left( \sum_{i=1}^n \frac{P_i}{I_i} \right) \cdot I_{coll} \quad (4.9)$$

where the sum runs over the unpaired bunches and  $P_i$  and  $I_i$  are, respectively, the measured probabilities and the proton currents in the considered bunches.  $P_{coll}^{beam\ gas}$  is the probability in the colliding bunch. From  $P_{coll}^{beam\ gas}$ , the  $\mu_{coll}^{beam\ gas}$  can be determined using the standard logarithmic formula and finally the  $\mu_{coll}$  with all backgrounds subtracted can be written as:

$$\mu_{coll}^{all\ bkg\ subtracted} = \mu_{coll}^{afterglow\ subtracted} - \mu_{coll}^{beam\ gas} \quad (4.10)$$

In order to verify the quality of the subtraction of single-beam background, the procedure has been tested for the unpaired bunches themselves. In Fig.4.10, the measured, afterglow subtracted and beam gas subtracted  $\mu$ -values for the unpaired bunch number 3196 in run 206881 is presented (on the left BCMHOR and on the right LCDOR), showing a very satisfactory



**Figure 4.7:** Measured (blu triangles) and afterglow-subtracted (green squares)  $\mu$  for LCDOR in the forbidden gap for run 206881.

subtraction result, with the  $\mu_{\text{value}}$  with all background subtracted at zero. The overall levels of background subtracted in the two ALFA runs can be summarized as follows.

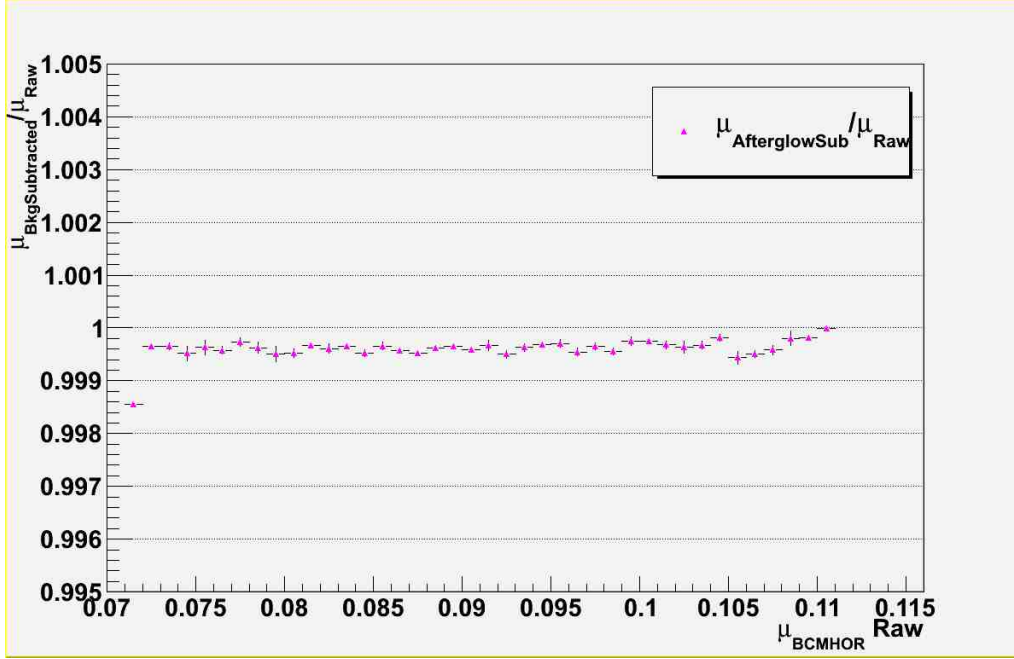
- Run 206881: In Fig.4.11: the percentages of afterglow plus beam-gas background are shown in blue for BCMHOR and in red for LCDOR algorithms, showing a level of 0.4% for BCMHOR and 0.2% for LCDOR.
- Run 213268: In Fig.4.12, the percentages of the afterglow plus beam-gas background are shown, in blue for BCMHOR and in red for LCDOR. The overall background level for BCMHOR is 10%, while for LUCID is 4%.

The systematic uncertainty related to the background subtraction is described in Sec.(4.5).

## 4.4 Luminosity Results

Once the background subtracted  $\mu$  has been measured, the instantaneous ( $\mathcal{L}_j$ ) and the integrated luminosities ( $L_j$ ) for each Luminosity Block ( $j$ ) and





**Figure 4.8:** Ratio between afterglow background subtracted and measured  $\mu$  for run 206881 for BCMHOR as a function of  $\mu$  measured.

for the whole run ( $L_{RUN}$ ) can be evaluated as:

$$\mathcal{L}_j = \frac{f}{\sigma_{pp}} \sum_{i=1}^n \mu_i \quad (4.11)$$

$$L_j = \mathcal{L}_j \cdot \Delta t_j \quad (4.12)$$

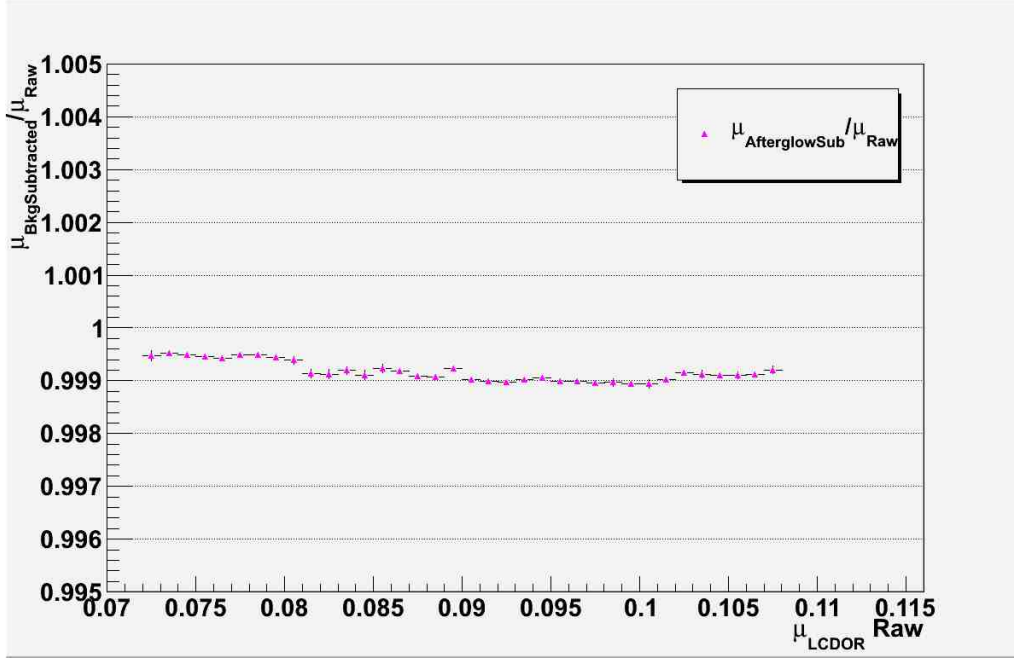
$$L_{RUN} = \sum_{j=1}^N L_j \quad (4.13)$$

where index  $j$  indicates the LB number ( $j=1, \dots, N$ ), index  $i$  refers to the colliding bunches ( $i=1, \dots, n$ ),  $f$  is the LHC revolution frequency,  $\Delta t_j$  is the duration of each LB and  $\sigma_{pp}$  is the inelastic  $pp$  cross section. Although  $\sigma_{pp}$  appears in Eq.4.11, it cancels with the  $\sigma_{pp}$  contained in the calibration of  $\mu$  ( $\epsilon = \frac{\sigma_{vis}}{\sigma_{pp}}$ ) so that the luminosity result is independent of the choice of the to-be-measured  $\sigma_{pp}$ .

#### 4.4.1 Results for run 206881 at $\beta^* = 90$ m

In Tab.4.2, the integrated luminosity values are reported for run 206881 using the various algorithms, together with their statistical uncertainties and





**Figure 4.9:** Ratio between afterglow background subtracted and measured  $\mu$  for run 206881 for LCDOR as a function of  $\mu$  measured. The ratio is about 2% with no dependency on  $\mu$ .

the deviations with respect to the reference BCMHOR measurement. The integrated luminosity is therefore (using the reference BCMHOR algorithm):

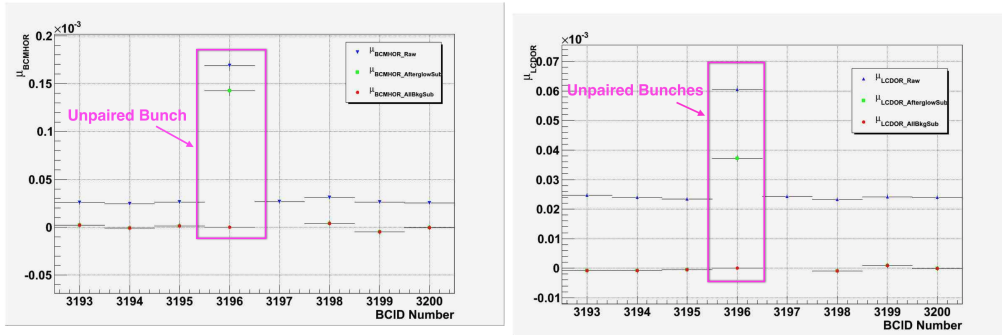
$$L_{206881} = 498.55 \pm 0.31 \mu b^{-1} \quad (4.14)$$

In Fig.4.13, the average number of interactions per bunch crossing ( $\mu$ ) as a function of the LB number is shown for the different luminosity algorithms, while in Fig.4.14 the percentage deviations with respect to the reference algorithm BCMHOR are shown. A very good consistency ( $<2\sigma$ ) with the only exception of LCDORA ( $5\sigma$ ) can be observed.

#### 4.4.2 Results for run 213268 at $\beta^* = 1000$ m

In Tab.4.3, the integrated luminosity values are reported for run 213268, together with their statistical uncertainties and the deviations with respect to the reference BCMHOR measurement. The integrated luminosity is therefore (using the reference BCMHOR algorithm):

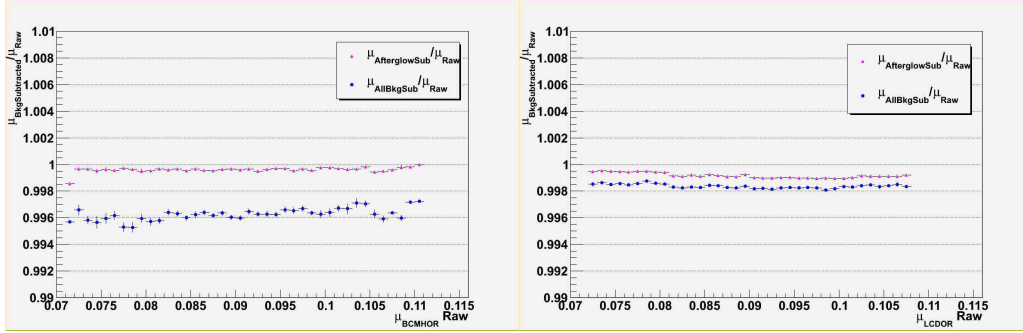
$$L_{213268} = 21.93 \pm 0.07 \mu b^{-1} \quad (4.15)$$



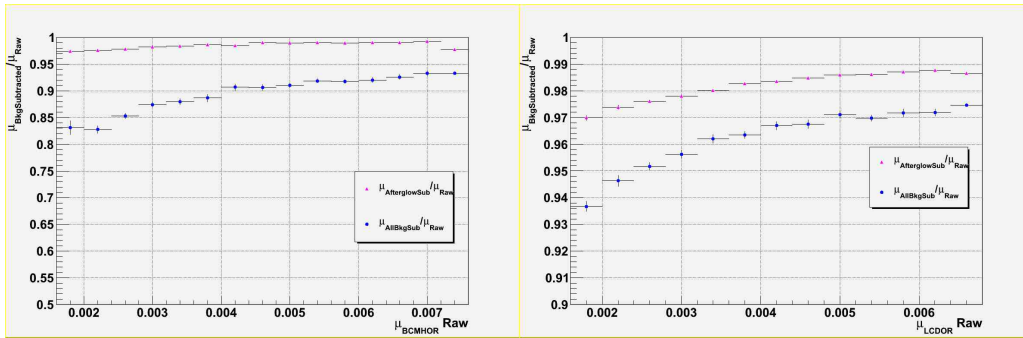
**Figure 4.10:** (Left) BCMHOR measured (blue triangles), afterglow subtracted (green squares), afterglow and beam gas subtracted (red circles)  $\mu$  for the unpaired bunch 3196 of run 206881. (Right) LCDOR measured (triangles), afterglow subtracted (squares), afterglow and beam gas subtracted (circles)  $\mu$  for the unpaired bunch 3196 of run 206881.

Algorithm	$L_{206881}(\mu\text{b}^{-1})$	$\delta L_{206881}(\text{stat})(\mu\text{b}^{-1})$	$\Delta L_{206881}/\delta L_{206881}$
BCMHOR	498.55	0.31	-
BCMHORC	497.51	0.43	-2
BCMFOR	498.97	0.31	1
BMCVORC	498.15	0.43	-1
LCDOR	499.28	0.12	2
LCDORA	500.29	0.15	5
LCDORC	498.73	0.15	1

**Table 4.2:** Integrated luminosity values (first column) and statistical errors (second column) determined with different algorithms for run 206881. In the third column, the deviations among the various algorithms to the reference BCMHOR are reported in units of the statistical errors.



**Figure 4.11:** Percentages of afterglow only (red triangles) and afterglow plus beam-gas (blue circles) for BCMHOR (left) and for LCDOR (right) for run 206881.



**Figure 4.12:** Percentages of afterglow only (red triangles) and afterglow plus beam-gas (blue circles) for BCMHOR (left) and for LCDOR (right) for the run 213268.

In Fig.(4.15), the average number of interactions per bunch crossing ( $\mu$ ) as a function of the LB number is shown for the various luminosity algorithms, while in Fig.(4.16) the percentage-deviations with respect to the reference algorithm BCMHOR are shown. For this run the all algorithms, with no exceptions, are compatible with the reference BCMHOR within less than  $2\sigma$ .

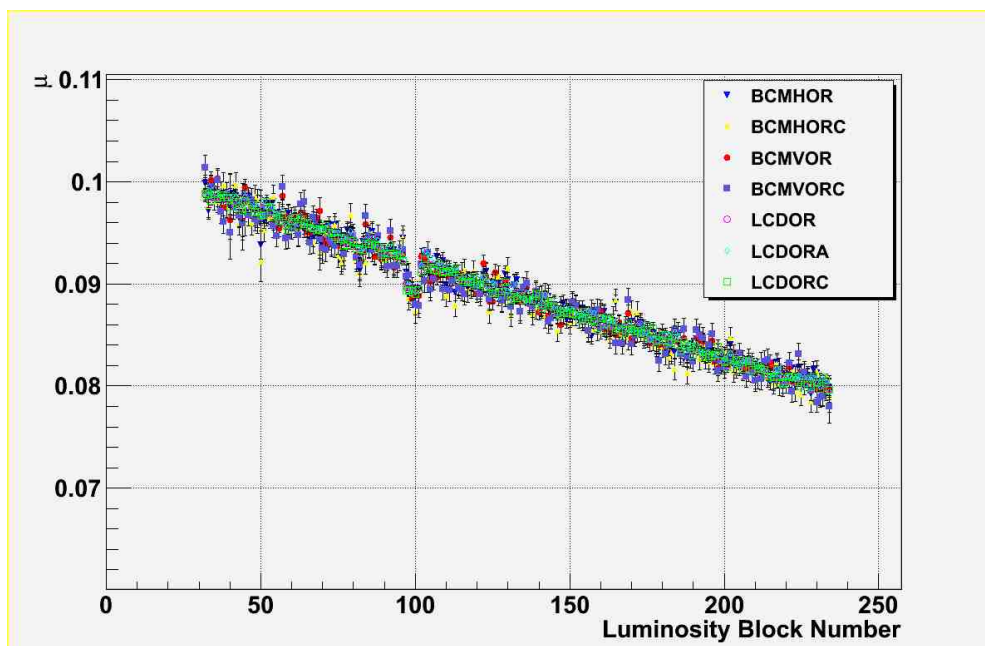


Figure 4.13: Average number of interactions per bunch crossing  $\mu$  as a function of the LB number for the different luminosity algorithms for run 206881.

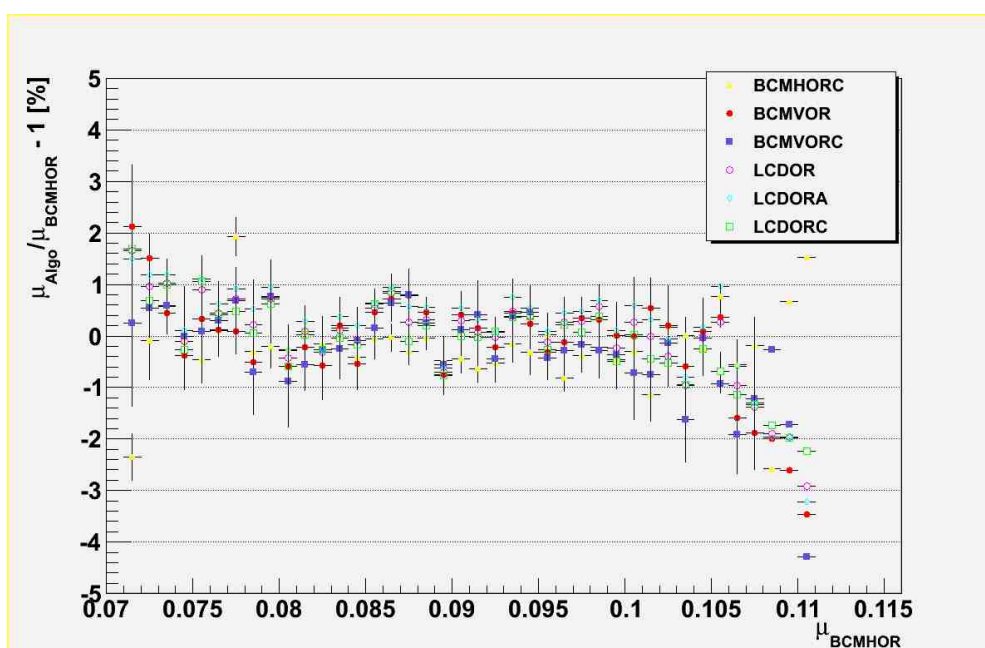
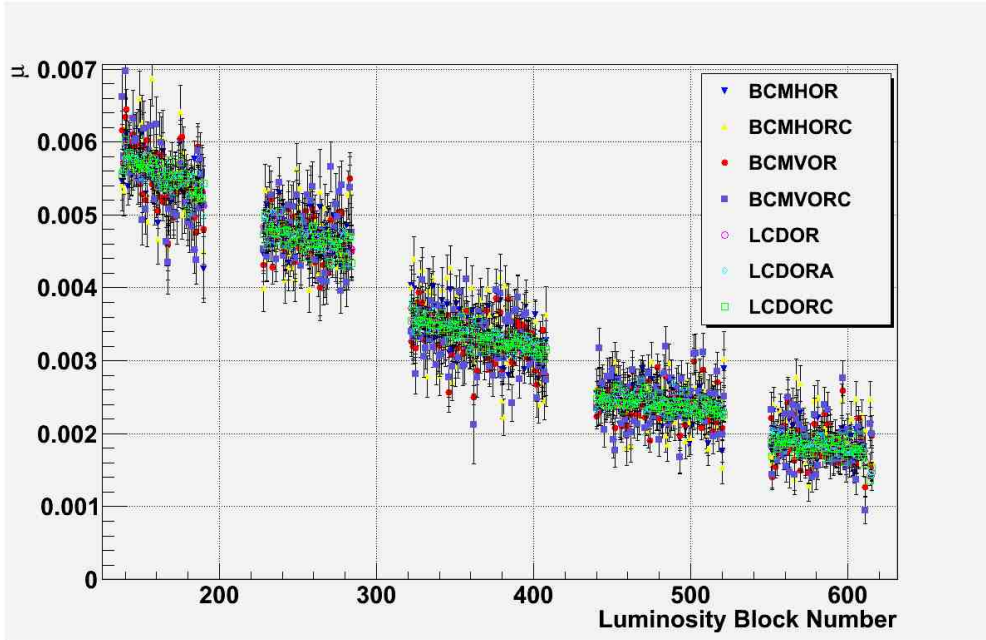


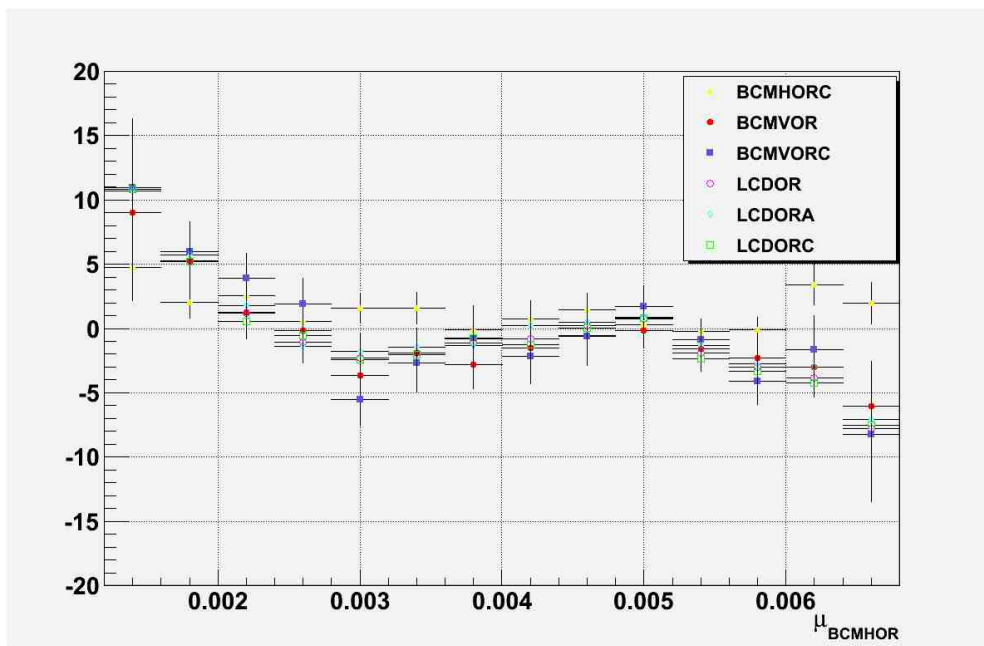
Figure 4.14: Percentage deviation of the various algorithms with respect to the reference one, BCMHOR.

Algorithm	$L_{213268}$ ( $\mu\text{b}^{-1}$ )	$\delta L_{213268}(\text{stat})$ ( $\mu\text{b}^{-1}$ )	$\Delta L_{213268}/\delta L_{213268}$
BCMHOR	21.93	0.07	-
BCMHORC	22.17	0.10	2
BCMVOR	21.76	0.07	-2
BMCVORC	21.89	0.10	0
LCDOR	21.81	0.02	-2
LCDORA	21.88	0.03	-1
LCDORC	21.78	0.03	-2

**Table 4.3:** Integrated luminosity values (first column) and statistical errors (second column) determined with different algorithms for run 213268. In the third column, the deviations among the various algorithms to the reference BCMHOR are reported in units of the statistical errors.



**Figure 4.15:** Average number of interactions per bunch crossing  $\mu$  as a function of the LB number for the various luminosity algorithms for run 213268.

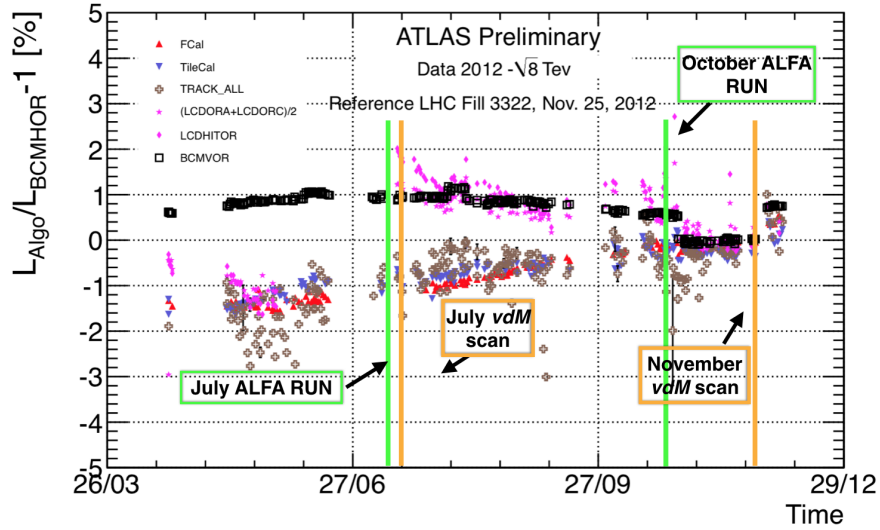


**Figure 4.16:** Percentage deviation of the various algorithms with respect to the reference one, BCMHOR.

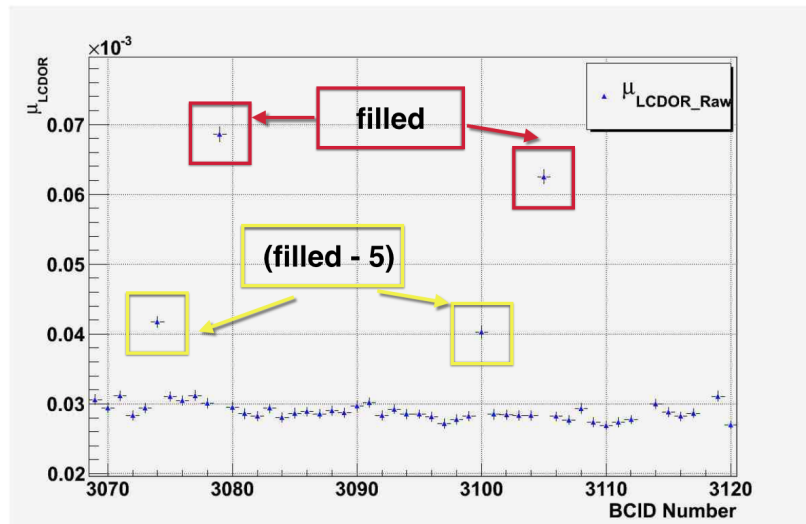
## 4.5 Systematic Uncertainties Evaluation

To estimate the systematic uncertainties related to the luminosity measurement, the analysis of the standard high-luminosity runs (see Sec.2.5) was used as a guideline, although not all the uncertainties quoted there should be considered in the special case of the high- $\beta^*$  runs, while additional ones should be added. The following list of systematic uncertainties is considered:

- ***van der Meer* calibration.** The systematic uncertainty evaluated from the *vdM* scan in 2012 is 3.27% (see Sec.2.5).
- **$\mu$ -dependence.** This contribution, relevant for the high- $\mu$  runs due to the very different  $\mu$ -ranges from *vdM* calibration to data taking, is not relevant for the present analysis.
- **Long-term stability.** This uncertainty is related to the observed time-related drifts of the various luminosity detectors. For run 206881 a *vdM* calibration close in time to the ALFA run was used, so no drift is expected and no systematic uncertainty is quoted. Run 213268 was taken one month before the corresponding *vdM* session. From Fig.4.17 a relative drift among detectors of 0.5% is visible between run 213268 and the corresponding *vdM* session. Such conservative value is therefore associated to the long-term drift systematic for this run only.
- **Background evaluation.** The main contribution to the background systematic uncertainty comes from the assumption that the single-beam background is well describes by using the unpaired bunches. In order to test this assumption and the related systematic uncertainty a particular effect, visible in LUCID only, has been exploited. As visible in Fig.4.18 in 5 BCIDs before any colliding or unpaired bunch, LUCID shows some activity which is related to the passage of Beam 1 (Beam 2) hitting LUCID C (A) from the back (i.e. from the opposite direction with respect to particles coming from the IP). This effect is observed in LUCID with a small but visible activity 5 BCIDs before the BCID in time measured at the IP ( $t=0$ ). This difference in time is due to the position of LUCID with respect to the IP. The activity is entirely due to beam-gas interactions. The beam-gas induced activity (normalized to the bunch current) observed 5 BCIDs before both colliding or unpaired bunches can be used to assess systematic uncertainty in the background estimation.

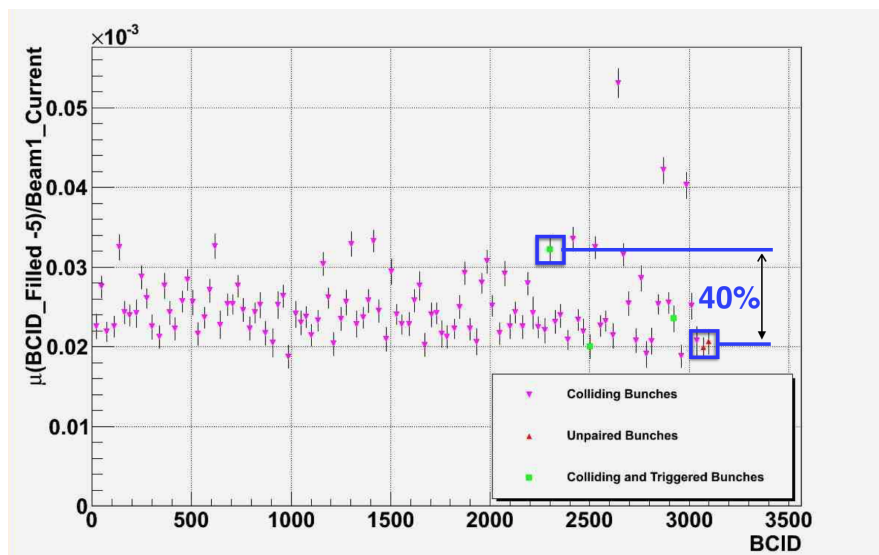


**Figure 4.17:** Long-term stability of the different luminosity algorithms along 2012. The dates of two ALFA runs (light green) and the corresponding *vdM* sessions (orange) are marked with vertical lines.

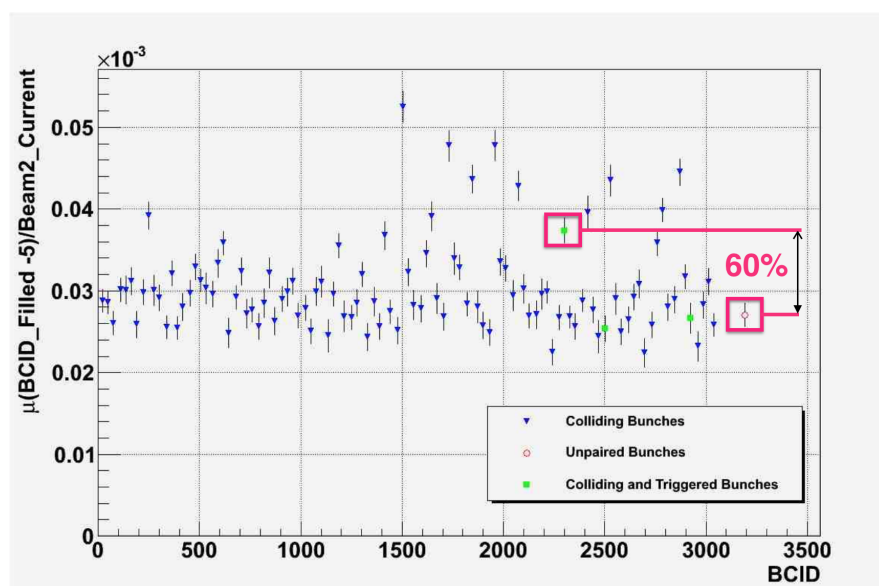


**Figure 4.18:**  $\mu$  as measured by LUCID (LCDOR algorithm) as a function of BCIDs. The activity 5 BCIDs before colliding and unpaired bunches is marked with coloured squares.





**Figure 4.19:** Run 206881: Beam-gas induced activity in LCDORA normalized to the bunch proton current for all colliding (blue), unpaired (red) and for the 3 ALFA-triggered colliding-bunches.



**Figure 4.20:** Run 206881: Beam-gas induced activity in LCDORC normalized to the bunch proton current for all colliding (blue), unpaired (red) and for the 3 ALFA-triggered colliding-bunches.

- run 206881. In Figs.(4.19) and (4.20) a maximum difference between the beam-gas induced activity 5 BCIDs before unpaired and colliding bunches of about 40% for LCDORA and 60% for LCDORC can be observed. We therefore assume a systematic uncertainty due to the background evaluation of 50% of the background itself (0.4% for BCMHOR, see 4.3.4), i.e. 0.2%.
- run 213268. From Figs.(4.21) and (4.22), we can evaluate a maximum difference between the unpaired and the colliding bunches of about 18% for LCDORA and 12% for LCDORC. Therefore, we assume a systematic uncertainty of 15% of the background level itself (10% for BCMHOR, see Sec.4.3.4), i.e. 1.5%.

In Tab.(4.4) the systematic uncertainties arising from the different sources are listed separately for the two runs. Overall a systematic uncertainty of 3.3% is estimated for run 206881 and 3.6% for run 213268.

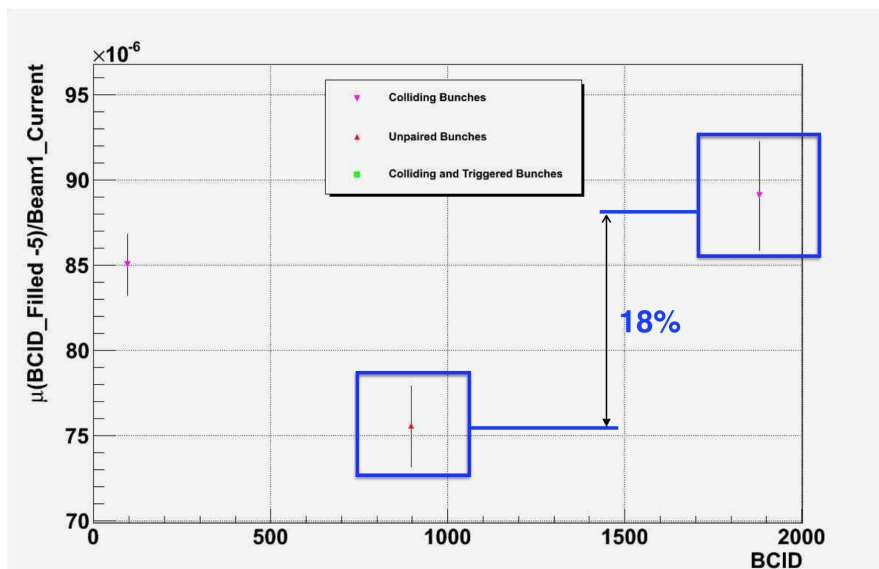
The final luminosity value for the two runs, including the systematic uncertainties are therefore

$$L^{206881} = 498.55 \pm 0.31(stat) \pm 16.33(sys)\mu b^{-1} \quad (4.16)$$

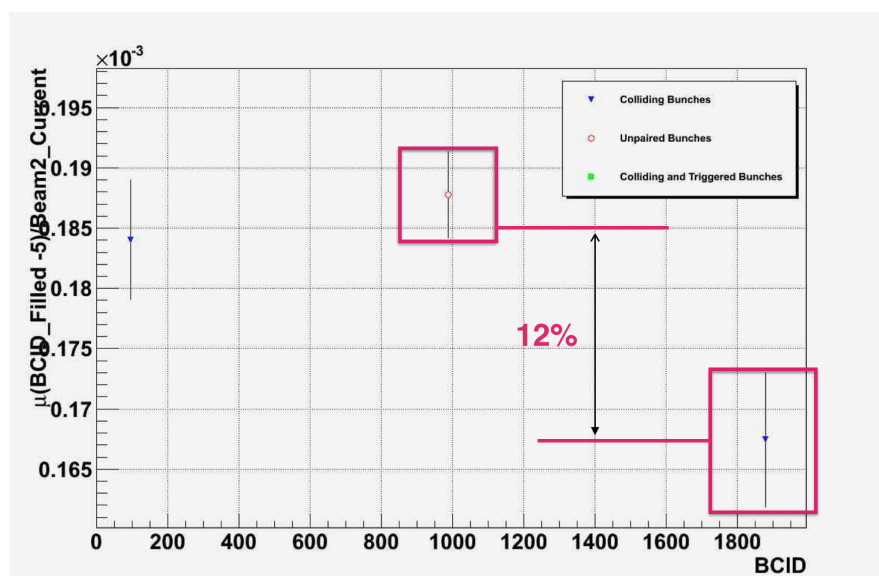
$$L^{213268} = 21.93 \pm 0.07(stat) \pm 0.80(sys)\mu b^{-1} \quad (4.17)$$

Uncertainty Sources	206881	213268
$vdM$ calibration	3.27%	3.27%
Long-term stability	0	0.5%
Background Subtraction	0.2%	1.5%
Total	3.3%	3.7%

**Table 4.4:** Systematic uncertainties on the luminosity measurement for runs 206881 and 213268.



**Figure 4.21:** Run 213268: Beam-gas induced activity in LCDORA normalized to the bunch proton current for all colliding (pink), unpaired (red) and for the 3 ALFA-triggered colliding-bunches.



**Figure 4.22:** Run 213268: Beam-gas induced activity in LCDORC normalized to the bunch proton current for all colliding (pink), unpaired (red) and for the 3 ALFA-triggered colliding-bunches.

## 4.6 General Comments

A few general remarks should be made about the obtained results:

- Compatibility of the results: despite the challenging conditions of the analysed high- $\beta^*$  runs in term of instantaneous luminosity, a remarkable consistency among LUCID and BCM measurements was achieved. The typical luminosity values of run 213268 is about 7 orders of magnitude lower than the values of the standard physics runs due to lower values of both  $\mu$  ( $\sim 10^{-3}$  compared to  $\mu \sim 20$ ) and number of colliding bunches (2 compared to 1400) and much lower than the value for which both LUCID and BCM were designed for. This is very encouraging for the future of ALFA runs to be acquired in LHC Run II with even higher  $\beta^*$ , aimed to reach the Coulomb-nuclear interference region for the total cross section measurement.
- In the present analysis we assumed as reference BCMHOR algorithm for consistency with the standard analysis, despite the fact that LUCID shows a clearly smaller background level and, consequently, a smaller systematic uncertainty. Studies are ongoing in order to verify the absence of additional effects in LUCID which would prevent using it as a reference detector in the ALFA runs. In such case a drastic reduction in the systematic uncertainty on the background would be possible (about a factor 2), although at the moment this is not the largest systematic contribution (represented by the  $vdM$  calibration).
- From Eq.(3.11), the percentage systematic uncertainty ( $\frac{\delta L}{L}$ ) in the luminosity measurements enters in the overall  $\sigma_{tot}$  uncertainty as half ( $\frac{1}{2} \frac{\delta L}{L}$ ). This means that the real contribution to the total systematic uncertainty for luminosity to the one on  $\sigma_{tot}$  is 1.6% (run 206881) and 1.8% (for run 213268).
- The analysis of the elastic distribution is far from being finished by the ALFA community. The luminosity values for the absolute normalization cannot be nevertheless provided.

# Conclusions

The work described in this thesis has been performed within the ATLAS experiment operating at the LHC collider at CERN. The analyzed data consist in two ATLAS runs acquired in special beam conditions, optimized for the measurement of the total proton-proton cross section at a center of mass energy of  $\sqrt{s} = 8$  TeV. This measurement is crucial as the total cross section is not calculable in the context of perturbation theory but can only be estimated and bounded, under special hypotheses, as a function of the center of mass energy. The particular beam-optics used for the data taking mainly consist in very high betatron-function values at the ATLAS interaction point ( $\beta^*$ ) and parallel-to-focusing configuration, necessary to allow for the measurement of the elastic interaction rate at very low scattering angles. The measurement of the proton-proton elastic scattering at low angles is used, within the Optical Theorem formalism, to determine the total proton-proton cross section. Using such formalism, an independent evaluation of the luminosity delivered by LHC is necessary for the total cross section measurement. The luminosity determination is the main argument of this thesis. The two runs acquired for this purpose are characterized by  $\beta^* = 90$  m and  $\beta^* = 1000$  m. Such large values of  $\beta^*$  and low number of colliding bunches imply that the instantaneous luminosities are up to seven orders of magnitude lower than the standard LHC running conditions. This represents a real challenge for the luminosity measurement for various reasons. First, the luminosity detectors are close, if not below, the sensitivity range which they were designed for. Second, the different sources of physical background become competitive with the interaction rate, and must be therefore carefully evaluated and subtracted, and the related systematic uncertainties assessed. Finally, instrumental effects such as ageing and calibration stability with time must be carefully understood in order to correct the measurement. All the steps of the analysis were entirely and personally developed by the candidate and can be summarized as follows:

- development of a code aimed to measure the luminosity for various luminosity detectors and algorithms in particular the Beam Condition

Monitor (BCM) and the LUCID detectors were used as they measure the luminosity bunch-by-bunch with various algorithms;

- modelling of the background from different sources and implementation of a background subtraction procedure;
- assessment of the systematic uncertainties due to the various sources, in particular related to the background subtraction and the time-stability of the luminometers.

The results obtained show a remarkable consistency among the detectors and algorithms (at the  $2\sigma$  level), which was not straightforward given the challenging conditions of the data taking. The main systematic uncertainties are related to the absolute calibration of the detectors through the Van der Meer scans (3.27% , not evaluated in the context of this thesis) and to the background subtraction. An original method for the determination of this uncertainties was developed in this thesis exploiting a side-effect of the beam-background in the LUCID detector. The final background percentage level has been evaluated to be 0.2% and 1.5% for the  $\beta^* = 90$  m and of  $\beta^* = 1000$  m runs, respectively.

The luminosity values determined in this thesis will be provided to the physics community performing the measurement of the proton-proton elastic scattering rate in order to allow the necessary normalization for the determination of the elastic (and then total) cross section. Such analysis is still not in a final state, while the luminosity determination is ready to be used.

$$L^{206881} = 498.55 \pm 0.31(stat) \pm 16.33(sys)\mu b^{-1}$$

$$L^{213268} = 21.93 \pm 0.07(stat) \pm 0.80(sys)\mu b^{-1}$$

In LHC Run II, starting in 2015, a proton-proton total cross section measurement at a center of mass energy of 13 TeV is planned to be performed, in order to extend the energy-range of the measurement and study, with a larger arm, the behavior of the total cross section with increasing energy. If the Coulomb-Nuclear interference region of the elastic scattering cross section would not be reached (for which an even more challenging increase of the  $\beta^*$  would be needed), a luminosity-dependent measurement based on the Optical Theorem will again be necessary.

The tools and the experience developed in this thesis will therefore be fundamental for such a goal.

## Appendix A

# Derivation of Hill's Equations

In this Appendix, the derivation of the Hill's Equations will be reported, starting from the equation of motion in a dipolar magnet and in a quadrupolar magnet.

$$\frac{d\vec{p}}{dt} = q(\vec{E} + \vec{v} \wedge \vec{B}) \quad (\text{A.1})$$

$$\frac{d}{dt}(p_x \hat{x} + p_s \hat{s} + p_y \hat{y}) = q(v_x, v_s, v_y) \wedge (B_x, 0, B_y) \quad (\text{A.2})$$

$$\dot{p}_x \hat{x} + p_x \dot{\hat{x}} + \dot{p}_s \hat{s} + p_s \dot{\hat{s}} + \dot{p}_y \hat{y} + p_y \dot{\hat{y}} = q(v_y B_x - v_x B_y) \hat{s} - qv_s B_x \hat{z} \quad (\text{A.3})$$

Remembering the Poisson relations:

$$\dot{\hat{x}} = \vec{\omega} \wedge \hat{x} = \dot{\phi} \hat{y} \wedge \hat{x} = \frac{1}{\rho} \rho \dot{\phi} \hat{s} = \frac{v_s}{\rho} \hat{s} \quad (\text{A.4})$$

$$\dot{\hat{s}} = \dot{\phi} \hat{y} \wedge \hat{s} \quad (\text{A.5})$$

$$\dot{p}_x \hat{x} + \dot{p}_s \hat{s} + \dot{p}_y \hat{y} + p_x \frac{v_s}{\rho} \hat{s} - p_s \frac{v_s}{\rho} \hat{x} = qv_s B_y \hat{x} + q(v_y B_x - v_x B_y) \hat{s} - qv_s B_x \hat{y} \quad (\text{A.6})$$

$$\left( \dot{p}_x - p_s \frac{v_s}{\rho} \right) \hat{s} + \dot{p}_y \hat{y} = qv_s B_y \hat{x} + q(v_y B_x - v_x B_y) \hat{s} - qv_s B_x \hat{y} \quad (\text{A.7})$$

$$\dot{p}_x - p_s \frac{v_s}{\rho} = qv_s B_y \quad (\text{A.8})$$

$$\dot{p}_s + p_x \frac{v_s}{\rho} = q(v_y B_x - v_x B_y) \quad (\text{A.9})$$

$$\dot{p}_y = -qv_s B_x \quad (\text{A.10})$$

The field in a dipolar magnet is:

$$B_x = 0 \quad (\text{A.11})$$

$$B_y = -B \quad (\text{A.12})$$

$$B_s = 0 \quad (\text{A.13})$$

while the reference orbit is

$$v_x = 0 \quad (\text{A.14})$$

$$v_s = v \quad (\text{A.15})$$

$$v_z = 0 \quad (\text{A.16})$$

$$p_s \frac{v_s}{\rho} = qv_s B \quad (\text{A.17})$$

$$p_s = q\rho B \quad (\text{A.18})$$

The motion in a dipolar magnet is, then:

$$\dot{p}_x - p_s \frac{v_s}{\rho} = -qv_s B \quad (\text{A.19})$$

$$\dot{p}_s + p_x \frac{v_s}{\rho} = qv_x B \quad (\text{A.20})$$

$$\dot{p}_y = 0 \quad (\text{A.21})$$

The field in a quadrupolar magnet is:

$$B_x = a_{xx}x + a_{xy}y \quad (\text{A.22})$$

$$B_y = a_{yx}x + a_{yy}y \quad (\text{A.23})$$

$$B_s = 0 \quad (\text{A.24})$$

This contribution added to the dipole magnet gives:

$$B_x = a_{xx}x + a_{xy}y \quad (\text{A.25})$$

$$B_y = B_{0y} + a_{yx}x + a_{yy}y \quad (\text{A.26})$$

$$B_s = 0 \quad (\text{A.27})$$

$$B_x = \alpha x + \beta y \quad (\text{A.28})$$

$$B_y = B_{0y} + \beta x - \alpha y \quad (\text{A.29})$$

$$B_s = 0 \quad (\text{A.30})$$

With the following conditions:

$$\text{div} \vec{B} = a_{xx} + a_{yy} = 0 \quad (\text{A.31})$$

$$\text{rot} \vec{B} = (0, a_{xy} - a_{yx}, 0) = 0 \quad (\text{A.32})$$



in the chosen coordinate system

$$B_y = B_{0y} + \beta x - \alpha y \quad (\text{A.33})$$

$$B_y(x=0) = B_{0y} - \alpha y = B_{0y} \quad \alpha = 0 \quad (\text{A.34})$$

The magnetic field becomes:

$$B_x = -\beta y \quad (\text{A.35})$$

$$B_y = -B_{0y} - \beta x \quad (\text{A.36})$$

$$B_s = 0 \quad (\text{A.37})$$

The equations of motion become:

$$\dot{p}_x = -p_s \frac{v_s}{\rho} = qv_s B_y \quad (\text{A.38})$$

$$\dot{p}_s + p_x \frac{v_s}{\rho} = q(v_y B_x - v_x B_y) \quad (\text{A.39})$$

$$\dot{p}_y = -qv_s B_x \quad (\text{A.40})$$

We have a solution that focuses in  $x$

$$\dot{p}_x - p_s \frac{v_s}{\rho} = -qv_s(B_{0y} + \beta x) \quad (\text{A.41})$$

$$\dot{p}_y = qv_s \beta y \quad (\text{A.42})$$

and an other one that focuses in  $y$

$$\dot{p}_y = qv_s B_y \quad (\text{A.43})$$

The motion in the quadrupole is:

$$\dot{p}_x - p_s \frac{v_s}{\rho} = -qv_s(B_{0y} - \beta x) \quad (\text{A.44})$$

$$m \ddot{x} - p_s \frac{v_s}{\rho} = -qv_s(B_{0y} - \beta x) \quad (\text{A.45})$$

$$\frac{d}{dt} = v_s \frac{d}{ds} \quad (\text{A.46})$$

Finally we get the Hills equation:

$$mv_s^2 x'' - mv_s^2 \frac{1}{\rho} = -qv_s(B_{0y} + \beta x) \quad (\text{A.47})$$

$$x'' - \frac{1}{\rho} = -\frac{q}{p_s}(B_{0y} + \beta x) \quad (\text{A.48})$$

$$x'' - \frac{1}{\rho_0} \left(1 + \frac{x}{\rho_0}\right) = -\frac{q}{p_0} \left(1 - \frac{\delta p}{p_0}\right) (B_{0y} - \beta x) \quad (\text{A.49})$$

$$x'' - \frac{1}{\rho_0} + \frac{x}{\rho_0^2} \simeq -\frac{q}{p_0} B_{0y} - \frac{q}{p_0} \beta x \quad p_0 = q\rho_0 B_{0y} \quad (\text{A.50})$$

$$x'' - \frac{1}{\rho_0} + \frac{x}{\rho_0^2} \simeq -\frac{1}{\rho_0} - \frac{\beta}{\rho_0 B_{0y}} x \quad (\text{A.51})$$

$$x'' \simeq -\left(\frac{1}{\rho_0^2} + \frac{1}{\rho_0 \frac{\beta}{B_{0y}}}\right) x \quad (\text{A.52})$$

$$x'' \simeq -K(s)x \quad (\text{A.53})$$



# Bibliography

- [1] S.White, *Determination of the absolute luminosity at the LHC*. PhD thesis, Orsay, Universite Paris-Sud 11, Orsay, 2010.
- [2] W.Herr *Beam-Beam Interaction*, (CERN 2006-002) 2006.
- [3] W.Herr *Concept of Luminosity*, (CERN 2006-002) 2006.
- [4] P.Grafstrom and W.Kozanecki, *Luminosity Determination at Proton Colliders*, Progress in Particle and Nuclear Physics (2015), <http://dx.doi.org/10.1016/j.pnpnp.2014.11.002>.
- [5] K.Schindl, *The Injector Chain for LHC*, PS Division, CERN, 1211.
- [6] S. Mattig, *Luminosity Measurements with the ATLAS Detector*, Universitat Hamburg Department Physik.
- [7] S.van der Meer, CERN-ISR-PO-68-31, 1968.
- [8] S.M. White, R. Alemany-Fernandez, H.Burkhardt, M.Lamont, *First Luminosity Scans in the LHC*
- [9] ATLAS Collaboration, *The ATLAS Experiments at the CERN Large Hadron Collider*, JINST 3:S08003 (2008).
- [10] ATLAS Collaboration, *ATLAS Pixel Detector Technical Report*, CERN/LHCC, 1998.
- [11] J.N.Jackson, *The ATLAS Semiconductor Tracker (SCT)*, Nucl. Instrum. Meth. A541, 2005.
- [12] V.A. Mitsou, *The ATLAS Transition Radiation Tracker*, ATL-CONF-2003-012.,2003.
- [13] *The Beam Conditions Monitor*, JINST 3:P02004, 2008.

- 
- [14] *Forward Detectors*, JINST 3:S08003, 2008.
- [15] ATLAS Collaboration, *ATLAS Calorimeter Performance Technical Design Report*, CERN/LHCC, 1997.
- [16] ATLAS Collaboration, *Improved luminosity determination in pp collisions at  $\sqrt{s} = 7$  TeV using the ATLAS detector at the LHC*, Eur Phys J. C (2013) 73:2518.
- [17] ATLAS Collaboration, *Preliminary Determination in pp collisions at  $\sqrt{s} = 8$  TeV using the ATLAS Detector in 2012*, ATL-COM-LUM-2012-013.
- [18] M.Froissart, *Asymptotic Behaviour and Subtractions in the Mandelstam Representation*, Phys.Rev.123(1961), 1053.
- [19] R.G. Newton, *Optical Theorem and beyond*, 1976 American Association of Physics Teachers.
- [20] P. Grafstrom, *Measurement of the Total Cross Section and Soft Diffraction by the ATLAS and TOTEM experiments at the LHC*.
- [21] ATLAS NOTE, *Measurement of the total cross section in pp collisions at  $\sqrt{s} = 7$  TeV from elastic scattering with the ATLAS detector*, ATLAS-CONF-2014-040.
- [22] Oriunno, M. et al. *The Roman Pot for the LHC*, in 10th European Particle Accelerator Conference. 2006. Edimburg, Scotland.
- [23] The TOTEM Collaboration, *The TOTEM experiment at the CERN Large Hadron Collider*, 2008 JINST 3 S08007.
- [24] *Performance of the TOTEM Detectors at the LHC*. arXiv:1310.2908v1 [physics.ins-det] 10 Oct 2013.